

AD A 043387



12

## SYSTEMS, SCIENCE AND SOFTWARE

SSS-R-77-3119

### THEORETICAL BODY AND SURFACE WAVE MAGNITUDES FOR TWELVE NUMERICALLY SIMULATED CRATERING EXPLOSIONS

T. C. Bache  
J. F. Masso  
B. F. Mason

Topical Report

Sponsored by  
Advanced Research Projects Agency  
ARPA Order No. 2551



This research was supported by the Advanced Research Projects Agency of the Department of Defense and was monitored by AFTAC/VSC, Patrick Air Force Base, Florida, 32925, under Contract No. F08606-76-C-0041.

The views and conclusions contained in this document are those of the authors and should not be interpreted as necessarily representing the official policies, either expressed or implied, of the Advanced Research Projects Agency, the Air Force Technical Applications Center, or the U. S. Government.

Approved for Public Release, Distribution Unlimited.

January 1977

P. O. BOX 1620, LA JOLLA, CALIFORNIA 92038, TELEPHONE (714) 453-0060

AD No. \_\_\_\_\_  
DDC FILE COPY

AFTAC Project Authorization No. VELA/T/7712/B/ETR

Program Code No. 6H189

Effective Date of Contract: October 1, 1976

Contract Expiration Date: September 30, 1977

Amount of Contract: \$374,397

Contract No. F08606-76-C-0041

Principal Investigator and Phone No.

Dr. Thomas C. Bache, (714) 453-0060, Ext. 337

Project Scientist and Phone No.

Dr. Ralph W. Alewine, III, (202) 325-8484



UNCLASSIFIED

SECURITY CLASSIFICATION OF THIS PAGE (When Data Entered)

REPORT DOCUMENTATION PAGE		READ INSTRUCTIONS BEFORE COMPLETING FORM
1. REPORT NUMBER	2. GOVT ACCESSION NO.	3. RECIPIENT'S CATALOG NUMBER
4. TITLE (and Subtitle) THEORETICAL BODY AND SURFACE WAVE MAGNITUDES FOR TWELVE NUMERICALLY SIMULATED CRATERING EXPLOSIONS.		5. TYPE OF REPORT & PERIOD COVERED Topical Report.
7. AUTHOR(s) C. Bache, J. F. Masso and B. F. Mason		6. PERFORMING ORG. REPORT NUMBER SSS-R-77-3119
9. PERFORMING ORGANIZATION NAME AND ADDRESS Systems, Science and Software P. O. Box 1620 La Jolla, CA 92038		8. CONTRACT OR GRANT NUMBER(s) Contract No. F08606-76-C-0041
11. CONTROLLING OFFICE NAME AND ADDRESS VELA Seismological Center 312 Montgomery Street Alexandria, VA 22314		10. PROGRAM ELEMENT, PROJECT, TASK AREA & WORK UNIT NUMBERS Program Code No. 6H189 ARPA Order No. 2551
14. MONITORING AGENCY NAME & ADDRESS (if different from Controlling Office) 12 148p.		12. REPORT DATE January 1977
		13. NUMBER OF PAGES 142
		15. SECURITY CLASS. (of this report) UNCLASSIFIED
		15a. DECLASSIFICATION/DOWNGRADING SCHEDULE
16. DISTRIBUTION STATEMENT (of this Report) Approved for Public Release, Distribution Unlimited.		
17. DISTRIBUTION STATEMENT (of the abstract entered in Block 20, if different from Report) D D C AUG 24 1977 RECEIVED C		
18. SUPPLEMENTARY NOTES		
19. KEY WORDS (Continue on reverse side if necessary and identify by block number) Nuclear Explosion Seismology      Source Theory Seismology      Theoretical Seismograms Body Waves Surface Waves		
20. ABSTRACT (Continue on reverse side if necessary and identify by block number) The results of the Systems, Science and Software (S <sup>3</sup> ) contribution to a study of cratering explosions are presented. A series of twelve numerical simulations of 150 kt cratering explosions in three materials at several depths were carried out by Applied Theory, Incorporated. The data from these calculations were processed to compute theoretical far-field body and surface wave seismograms and from these to determine $m_b$ and $M_s$ . The $m_b$ and $M_s$ data is to be analyzed by Pacific Sierra Research. MS486 MS485		

DD FORM 1 JAN 73 1473

EDITION OF 1 NOV 65 IS OBSOLETE

UNCLASSIFIED

SECURITY CLASSIFICATION OF THIS PAGE (When Data Entered)

388507i

LB

UNCLASSIFIED

SECURITY CLASSIFICATION OF THIS PAGE(When Data Entered)

The theoretical seismogram calculations are done in a two-step process. First, an equivalent elastic source representation of the cratering event is obtained. The wave field is then propagated through realistic layered earth models to teleseismic distances. For this application the procedure is found to be more accurate for the shorter period body waves than for the surface waves. The  $m_b$  and  $M_s$  values are presented for the twelve 150 kt sources and for these sources scaled to 37.5 and 600 kt. Also given are the values for contained explosions of the same yield in the same emplacement material. The contribution of the ejecta fallback is studied and is found to be insignificant for teleseismic magnitude values.

→ MS4BB → MS4BS

ACCESSION for	
NTIS	White Section <input checked="" type="checkbox"/>
DDC	Buff Section <input type="checkbox"/>
UNANNOUNCED	<input type="checkbox"/>
JUSTIFICATION	
BY	
DISTRIBUTION/AVAILABILITY CODES	
Dist.	SP. CIAL
A	

UNCLASSIFIED

SECURITY CLASSIFICATION OF THIS PAGE(When Data Entered)

## TABLE OF CONTENTS

	Page
I. INTRODUCTION . . . . .	1
II. COMPUTATIONAL PROCEDURE . . . . .	3
III. DESCRIPTION OF THE CRATERING CALCULATIONS . .	7
IV. EQUIVALENT ELASTIC SOURCE REPRESENTATION . . .	9
4.1 MULTIPOLE COEFFICIENTS IN THE TIME DOMAIN . . . . .	9
4.2 THEORETICAL CONSTRAINTS ON THE MULTI- POLE COEFFICIENTS . . . . .	15
4.3 MULTIPOLE COEFFICIENTS IN THE FREQUENCY DOMAIN . . . . .	17
V. FAR-FIELD DISPLACEMENT SPECTRA . . . . .	18
VI. BODY WAVE MAGNITUDE, $m_b$ . . . . .	29
VII. SURFACE WAVE MAGNITUDE, $M_s$ . . . . .	37
VIII. CONTRIBUTION OF EJECTA FALLBACK TO TELESEISMIC MAGNITUDES . . . . .	46
8.1 BOUNDARY CONDITIONS . . . . .	46
8.2 SURFACE WAVES FROM EJECTA . . . . .	48
8.3 BODY WAVES FROM EJECTA . . . . .	52
IX. TELESEISMIC MAGNITUDES FOR 37.5 AND 600 kt . .	53
9.1 SOURCE SCALING . . . . .	53
9.2 BODY WAVES FOR SCALED SOURCES . . . . .	53
REFERENCES . . . . .	64
APPENDIX A - EQUIVALENT ELASTIC SOURCE . . . . .	66
APPENDIX B - APPLICATION OF THE MULTIPOLAR EXPANSION TECHNIQUE TO CRATERING EXPLOSIONS . . . .	72
APPENDIX C - PROPERTIES OF AN AXIALLY SYMMETRIC SEISMIC SOURCE . . . . .	82

	Page
APPENDIX D - DESCRIPTION OF A TYPICAL CALCULATION. . .	102
APPENDIX E - THE SEISMIC WAVES DUE TO A STRESS DISTRIBUTION APPLIED AT THE SURFACE OF A MULTILAYERED HALFSpace . . . . .	125



## I. INTRODUCTION

This report is the Systems, Science and Software ( $S^3$ ) contribution to a joint research project carried out in collaboration with Applied Theory, Incorporated (ATI) and Pacific Sierra Research (PSR). A series of cratering calculations were done by ATI and the results were transmitted to  $S^3$  for processing. The  $S^3$  contribution has been to compute theoretical body and surface wave records from the ATI data and from these to obtain  $m_b$  and  $M_s$ . The results are to be analyzed by PSR.

The computational procedure employed at  $S^3$  is to first obtain an equivalent elastic source representation of the cratering explosions. Having an elastic source representation, elastic wave propagation methods can be employed to compute theoretical seismograms. The key step in this procedure is clearly the interpretation of the raw data in terms of an equivalent elastic source.

The computation of an equivalent elastic source from the output of finite difference calculations has been accomplished at  $S^3$  for a number of complex explosion and earthquake sources. However, all of our experience has been with sources that were entirely surrounded by an elastic material. The cratering sources then provided a special problem. In fact, our technique is not rigorously valid for half-space sources of this kind. Therefore, it is quite important to understand the approximations that must be employed and their potential effect on the results.

In analyzing the approximations made we conclude that in every case the effects are much more severe for the S waves than for the P waves. In fact, the short period P waves seem to be handled very well by our technique. Since the S waves have almost no effect on the body wave seismograms, we have considerable confidence in the  $m_b$  values generated.



In order to compute  $M_s$  we have to accurately compute the source at periods of about 20 seconds. The finite difference calculations were terminated at 2.5 seconds. Therefore, our  $M_s$  calculations depend on the source having reached a static state. This is much closer to being true for the P waves than for the S waves. Fortunately, we find that for this case the S waves have to be quite a lot larger than the P waves to substantially perturb  $M_s$ , so our errors in the long period S waves may not be too important. Still, we have less confidence in the  $M_s$  values than in the  $m_b$  values. Nevertheless, we are treating all calculations the same and we can reasonably suppose that trends are properly reflected in the  $M_s$  data.

We also computed the seismic waves for the ejecta fallback for several of the sources. We find that this contribution to the body and surface waves is too small to be of any significance for  $m_b$  and  $M_s$  measurements.

The report is organized in nine sections and five appendices. In Section II we outline the computational procedures. We also summarize the content of the appendices where detailed exposition of some aspects of the theory and to application is given. In Section III we briefly describe the fourteen finite difference calculations to be studied. Twelve of these are cratering calculations and two are for spherically symmetric contained explosions. In Section IV we discuss the equivalent elastic source representation of the cratering calculations. The approximations made and their effect on the solution is indicated in some detail in this section. The far-field displacement spectra are extracted from the source calculations and displayed in Section V. Sections VI and VII give the  $m_b$  and  $M_s$  results. In Section VII the seismic waves generated by the ejecta fallback are discussed. Finally, in Section IX the sources are scaled to 37.5 and 600 kt and the  $m_b$  and  $M_s$  are computed for each of the fourteen sources.

## II. COMPUTATIONAL PROCEDURE

In this section we outline the computational procedure used to compute  $M_s$  and  $m_b$  for the ATI cratering calculations. The main steps in our procedure may be listed as follows:

1. The ATI performed cratering calculations were carried into the regime where the material response is approximately linearly elastic. A tape was then prepared containing the time histories of the divergence and curl ( $\nabla \cdot \underline{u}(t)$ ,  $\nabla \times \underline{u}(t)$ ) of the displacement field on a radius, denoted the elastic radius, centered at ground zero. The geometry and coordinate system are shown in Figure 2.1.
2. The divergence and curl are expanded in a series of spherical harmonics to obtain an equivalent elastic source. The procedure is formally that described by Bache and Harkrider [1976] for sources in a whole space. However, the presence of a free surface requires a number of assumptions that, to some extent, control the solution. The extent of this effect is discussed in some detail in this report. However, the most important point is that all the cratering calculations are treated the same way and the relative values of  $m_b$  and  $M_s$  should be preserved.
3. Using the equivalent elastic source, synthetic seismograms are computed for body waves and surface waves. For body waves the pertinent references are Bache and Harkrider [1976] and Bache, et al. [1976]. For surface waves we use the method of Harkrider which has been described in numerous publications; e.g., Harkrider [1964], with certain modifications indicated in Section VII.

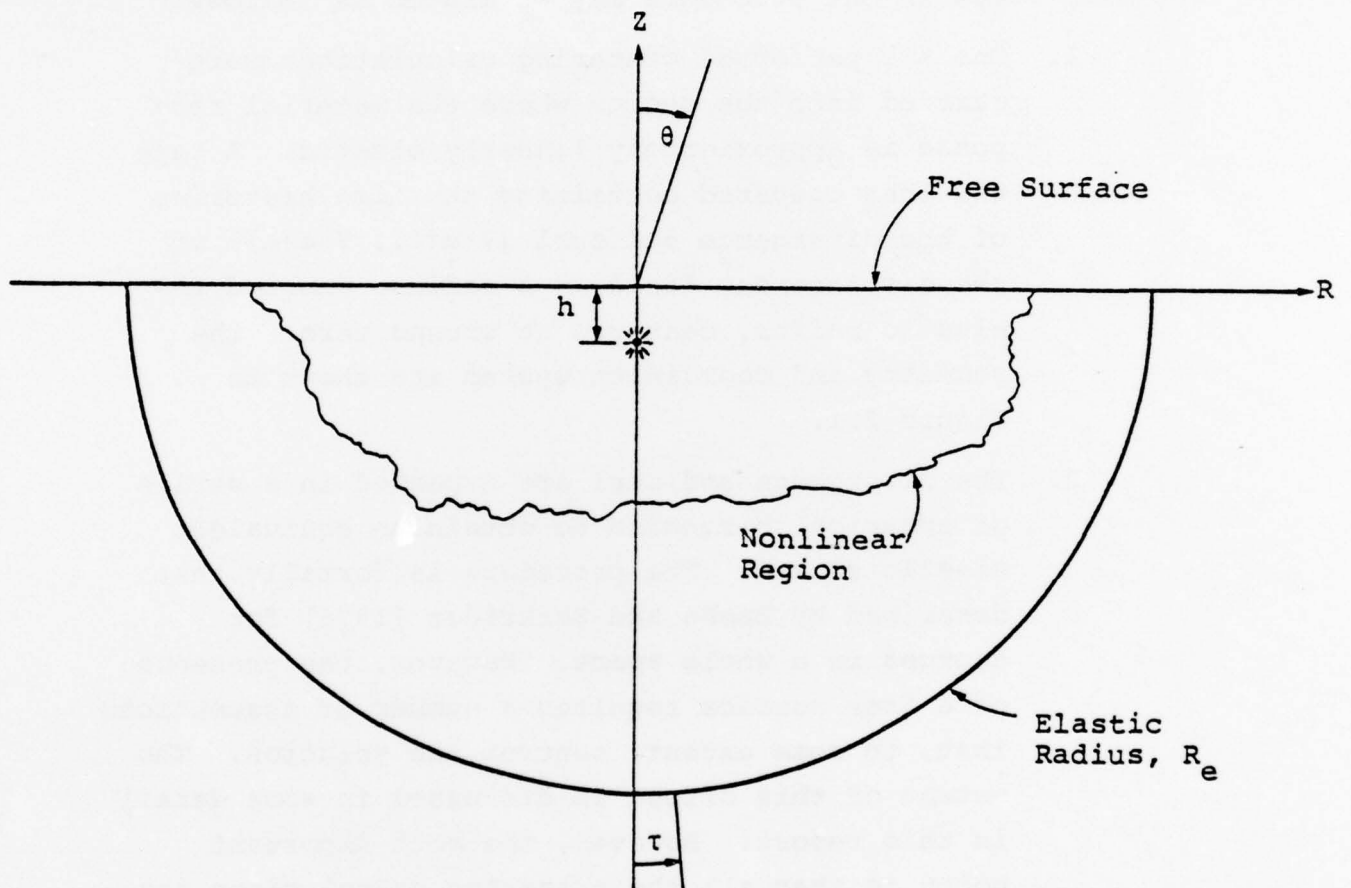


Figure 2.1. The geometry and coordinate system for the cratering calculations. The solution is independent of the azimuthal coordinate.

4. The values of  $m_b$  and  $M_s$  are strongly dependent on the crust and upper mantle models used in the synthetic seismogram calculations. However, the same models are used in all calculations and the relative values should be insensitive to these models.
5. The free surface stresses due to the ejecta fallback were also provided to us by ATI. These data were analyzed to determine the effect on the far-field body and surface waves.

Further descriptions of the computational procedure are contained in subsequent sections of the main body of the report where the equivalent elastic source representation, the far-field displacement spectra and the teleseismic waveforms are discussed. Also included in the report are a number of Appendices which treat various aspects of our work in considerable detail. The content of these appendices is briefly summarized below.

#### Appendix A: Theory of the Equivalent Elastic Source Representation

This appendix is a reproduction of a section of a paper by Bache and Harkrider [1976]. It outlines the mathematical formulation for representing an arbitrary volume source in an elastic, homogeneous and isotropic space in terms of an expansion in spherical harmonics. The expansion coefficients, the multipole coefficients, provide an equivalent elastic source representation.

#### Appendix B: Application of the Multipolar Expansion Technique to Cratering Explosions

The procedures of Appendix A, appropriately modified, can give a satisfactory representation of the output of the cratering calculations. The approximations required are discussed in Appendix B.



Appendix C: Effect of Source Symmetry on the Multipolar Source

The most important approximation is in the choice of the symmetry to be imposed on the computed radiation field. The possibilities are discussed in Appendix C.

Appendix D: Detailed Description of a Typical Calculation of the Multipolar Source Representation

We go through a typical calculation step-by-step and indicate the operations carried out.

Appendix E: The Seismic Waves Due to a Stress Distribution Applied at the Surface of a Multilayered Half-space

In order to compute  $m_b$  and  $M_s$  for the ejecta impact portion of the cratering calculations, it was necessary to extend our theoretical results to include the case of a distribution load on the surface. The theory is developed in Appendix E.



## III. DESCRIPTION OF THE CRATERING CALCULATIONS

In order to carry out our analyses of the cratering calculations, it was necessary to have some information about the source depth and the local material properties. This information, together with an identifier for each calculation for use in subsequent sections, is summarized here.

We will be describing fourteen source calculations in three emplacement materials. Two of these are one-dimensional calculations for contained explosions in a homogeneous whole space and provide benchmark cases for measuring the effect of the cratering. The other twelve are cratering calculations. The important parameters characterizing the calculations are summarized in Table 3.1.

We see from the table that the calculations have the potential to help us understand:

1. The effect of burial depth on the teleseismic signature of cratering explosions.
2. The effect of emplacement material on the signal from cratering explosions.
3. The difference between cratering and contained shots in the same material.

Considering the approximations made in our calculations (exclusive of any difficulties with the finite difference calculations), the above are listed in order of the amount of confidence we place in the results. That is, we are most optimistic about our conclusions regarding differences in the source coupling between events that differ only by the burial depth. On the other hand, we are least confident in conclusions about the differences between cratering and contained explosions.

TABLE 3.1  
PARAMETERS DESCRIBING THE ATI CALCULATIONS

<u>Identifier</u>	<u>Material</u>	<u>Depth (km)</u>	<u><math>\alpha</math> (km/sec)</u>	<u><math>\beta</math> (km/sec)</u>	<u><math>\rho</math> (km/sec)</u>
1	Granite	0.159	4.402	2.54	2.661
2	"	0.207	4.402	2.54	2.661
3	"	0.253	4.406	2.542	2.661
4	Dry Sandstone	0.159	2.822	1.740	2.30
5	"	0.207	2.825	1.743	2.30
6	"	0.253	2.828	1.744	2.30
7	Low Strength	0.207	2.836	1.755	2.30
8	Wet Sandstone	0.053	2.620	1.509	2.40
9	"	0.159	2.624	1.592	2.40
10	"	0.207	2.614	1.513	2.40
11	"	0.253	2.618	1.517	2.40
12	"	0.531	2.619	1.519	2.40
13	Granite	Spherically Symmetric	4.239	2.448	2.661
14	Wet Sandstone	Spherically Symmetric	2.619	1.530	2.40

## IV. EQUIVALENT ELASTIC SOURCE REPRESENTATION

4.1 MULTIPOLE COEFFICIENTS IN THE TIME DOMAIN

The procedure used to obtain the equivalent elastic source representation for the cratering calculations is described in detail in the Appendices. The basic equations written in the frequency domain are given by A.1-A.5 of Appendix A. In our implementation, we actually use the time domain analogues of these equations. That is, the equation of motion is written

$$\frac{\partial^2 \underline{u}}{\partial t^2} = \alpha^2 \nabla \chi^{(4)} - 2\beta^2 \nabla \times \underline{\chi} \quad (4.1)$$

where the Cartesian potentials are defined by

$$\begin{aligned} \chi_4 &= \nabla \cdot \underline{u} \\ \underline{\chi} &= \frac{1}{2} \nabla \times \underline{u}. \end{aligned} \quad (4.2)$$

The potentials are expanded in spherical eigenfunctions as follows

$$\begin{aligned} \chi^{(j)}(\underline{R}, \omega) &= \sum_{\ell=0}^{\infty} \sum_{m=0}^{\ell} \left[ A_{\ell m}^{(j)}(\underline{R}, t) \cos m\phi \right. \\ &\quad \left. + B_m^{(j)}(\underline{R}, t) \sin m\phi \right] P_{\ell}^m(\cos\theta), \quad j = 1, 2, 3, 4. \end{aligned} \quad (4.3)$$

Note that these equations are identical to A.1, A.2, A.4, if

$$A_{\ell m}^{(j)}(\omega) = \frac{1}{h_{\ell}^{(2)}(k_j R)} \int_{-\infty}^{\infty} A_{\ell m}^{(j)}(\underline{R}, t) e^{-i\omega t} dt, \quad (4.4)$$

and similarly for  $B_{\ell m}^{(j)}(\omega)$ . Note that (4.4) is simply a Fourier transformation normalized by the Hankel function.

In computing the multipolar representation of the cratering calculations we assume axisymmetry and vertical antisymmetry, the case described in Section C.2.3 of Appendix C. Then the multipole coefficients in the time domain are actually computed from C.32-C.34. For example, for the P-wave portion of the field the nonzero terms are

$$A_{\ell 0}^{(4)}(R, t) = (2\ell + 1) \int_0^{\pi/2} \chi^{(4)}(R, \theta, t) P_{\ell}^0(\cos \theta) \sin \theta \, d\theta,$$

$$\ell = 1, 3, 5, \dots, \quad (4.5)$$

and the  $\chi^{(4)}(R, \theta, t)$  is the time history of the divergence of the displacement field given on the quarter-circle of radius  $R_e$  (see Figure 2.1).

It turns out that the dominant term for the  $m_b$  and  $M_s$  determinations is the leading term in the expansion of the P-wave portion of the field; that is,  $A_{10}^{(4)}(R, t)$ . The other terms provide higher order corrections as will be explained in later sections. For now, let us examine the "dipole-P" term as it is a fair representation of the equivalent elastic source. In Figures 4.1 through 4.3 the computed  $A_{10}^{(4)}(R, t)$  is plotted for each of the twelve cratering calculations. The multipole coefficient is dimensionless and the amplitude depends on the radius,  $R$ .

For each calculation we indicate the theoretical arrival time for the P, S and Rayleigh (R) waves. For the P wave this time is simply  $(R-h)/\alpha$  since the shortest path from the source to the elastic radius is straight down. The same is done for the S wave. The theoretical arrival time for the Rayleigh wave at the free surface is  $R/V_R$ , where the Rayleigh wave velocity,  $V_R = 0.91928$ . This is the time

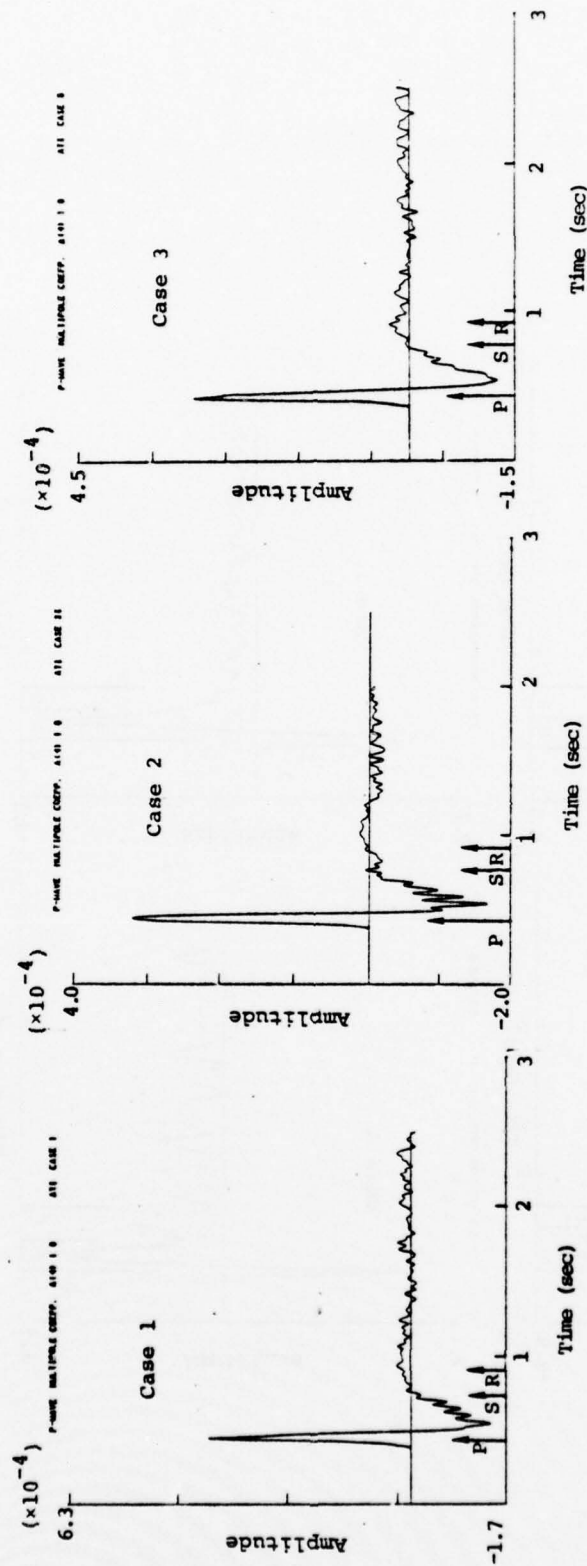


Figure 4.1. The dipole-P multipole coefficient,  $A_{10}^{(4)}(R, t)$ , for the three cratering calculations in granite. For these calculations  $R = 2.1$  km.



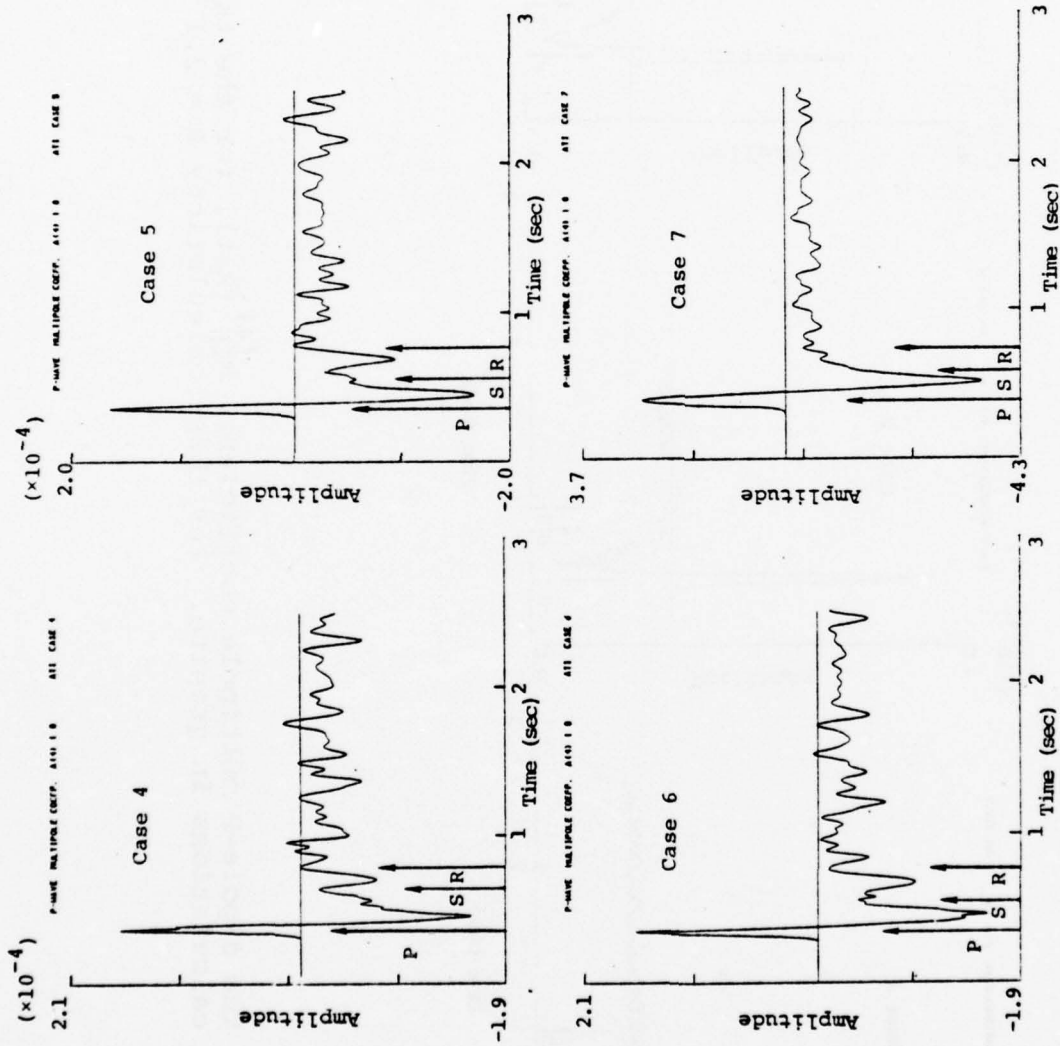


Figure 4.2. The dipole-P multipole coefficient for the four cratering calculations in dry sandstone. For these calculations  $R = 1.2$  km.

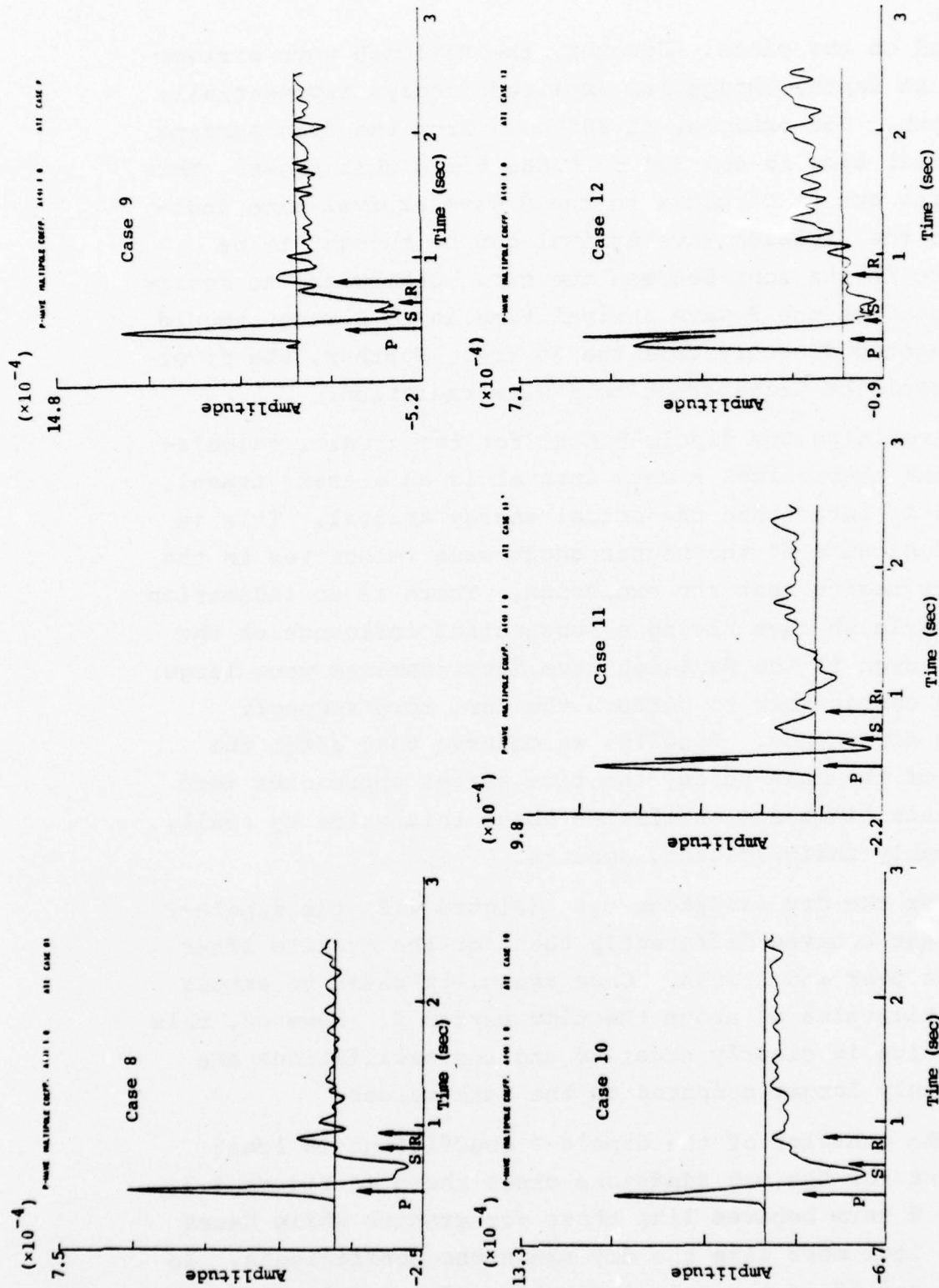


Figure 4.3. The dipole-P multipole coefficient for the five cratering calculations in wet sandstone. For Case 8,  $R = 1.3$  km and  $R = 1.2$  km for the remaining four calculations.

indicated on the plots. However, the Rayleigh wave arrives earlier at depth, though its amplitude decays exponentially with depth. For example, at  $30^\circ$  down from the free surface the arrival time is  $\cos 30^\circ$  or 0.866 times that shown. This time turns out to be close to the S wave arrival time indicated so the Rayleigh wave arrival can be thought to be somewhere in the zone between the two. Otherwise, no energy is expected at the S wave arrival time as no S waves should be propagated directly from the source. Further, the divergence should be transparent to S wave radiation.

Examining the dipole-P term for the granite calculations, the theoretical P wave arrival is an elastic travel time and is later than the actual energy arrival. This is expected because of the higher shock wave velocities in the nonlinear regime near the explosion. There is no indication of the Rayleigh wave having a substantial influence on the record. Even if the Rayleigh wave displacements were large, we would expect them to perturb the curl more strongly than the divergence. Finally, we observe that after the passage of the main pulse, the time series approaches zero as a static limit and oscillates about this value by small, and probably insignificant, amounts.

For the dry sandstone case (Figure 4.2) the dipole-P coefficient behaves differently than for the granite after the first peak and trough. Once again, it seems to settle to a static value at about the time marked R. However, this static value is clearly negative and the oscillations are considerably larger compared to the peak values.

The behavior of the dipole-P coefficient is least consistent for the wet sandstone cases shown in Figure 4.3. The Case 8 term behaves like those for granite while Cases 9 and 10 look more like the dry sandstone coefficients. In Cases 11 and 12 is the only indication of possible difficulty

associated with the presence of Rayleigh wave energy. In the other cases the static limit is essentially attained before the Rayleigh wave arrival time but this is not true for the last two cases.

Finally, we should mention that some of the sudden jumps that occur in these time series, most prominently those in the first peak of Cases 11 and 12, are associated with rezoning in the finite difference calculations. See Appendix D for details.

#### 4.2 THEORETICAL CONSTRAINTS ON THE MULTIPOLE COEFFICIENTS

Our techniques for synthesizing teleseismic body and surface wave seismograms require the multipole coefficients in the frequency domain. The appropriate transformation is given by (4.4). That is, we must Fourier transform time series like those in Figures 4.1-4.3, then normalize by the Hankel function. Before discussing results of this operation, let us discuss the constraints on the form of the multipole coefficients that are imposed by the theory.

The theoretical constraints on the solution follow from the requirement that there be no static offset in the far-field. That is, we require that

$$\lim_{t \rightarrow \infty} u_{FF}(\tilde{R}, t) = 0, \quad (4.6a)$$

which is equivalent to requiring that

$$\lim_{\omega \rightarrow 0} \bar{u}_{FF}(\tilde{R}, \omega) = \omega^n, \quad n \geq 0. \quad (4.6b)$$

The far-field portion of the field is that which decays as  $R^{-1}$ . The relationship between the far-field displacement and the multipole coefficients for the case being studied is given by (C.47)-(C.48) of Appendix C. We point out that

the conditions (4.6) can be shown to be equivalent to requiring a finite static displacement in the near-field.

Comparing (4.6b) with (C.47)-(C.48), we see that we must require that

$$\lim_{\omega \rightarrow 0} A_{\ell m}^{(j)} = \omega^{n+2}, \quad n \geq 0, \quad (4.7)$$

for all  $\ell$  and  $m$ .

What are the implications of (4.7) for the time domain behavior of the multipole coefficients? From (4.4) we observe that

$$A_{\ell m}^{(j)}(\omega) = \frac{1}{h_{\ell}^{(2)}(k_j R)} \mathcal{F}\{A_{\ell m}^{(j)}(R, t)\}, \quad (4.8)$$

where  $\mathcal{F}\{\}$  denotes the Fourier transform of  $\{\}$ . Since

$$\begin{aligned} \lim_{t \rightarrow \infty} A_{\ell m}^{(j)}(R, t) &= \lim_{\omega \rightarrow 0} \mathcal{F}\left\{\frac{\partial A_{\ell m}^{(j)}(R, t)}{\partial t}\right\}, \\ &= \lim_{\omega \rightarrow 0} i\omega \mathcal{F}\{A_{\ell m}^{(j)}(R, t)\}, \end{aligned} \quad (4.9)$$

it is apparent that if  $A_{\ell m}^{(j)}(R, t)$  has a finite static limit,

$$\lim_{\omega \rightarrow 0} \mathcal{F}\{A_{\ell m}^{(j)}(R, t)\} = \omega^{-1}. \quad (4.10)$$

Then, since

$$\lim_{\omega \rightarrow 0} \frac{1}{h_{\ell}^{(2)}(k_j R)} = \omega^{\ell+1}, \quad (4.11)$$

we have

$$\lim_{\omega \rightarrow 0} A_{\ell m}^{(j)}(\omega) = \omega^{\ell}, \quad (4.12)$$

for those coefficients which have a finite static limit.



In view of (4.7) and (4.12) we see that the time domain coefficients for  $\ell \geq 2$  can have finite static limits. However, for the dipole ( $\ell=1$ ), we must require that

$$\lim_{t \rightarrow \infty} A_{\ell m}^{(j)}(R, t) = 0, \quad (4.13)$$

for the solution to be finite.

#### 4.3 MULTIPOLE COEFFICIENTS IN THE FREQUENCY DOMAIN

The Fourier transformation of terms of higher order than the dipole is carried out by assuming that the value at the last time step is the static value. For the dipole terms, like  $A_{10}^{(4)}(R, t)$  shown in Figures 4.1-4.3, we must have a zero static value. To accomplish this the coefficient is simply set to zero for all times greater than the final computed time step. For Cases 1, 2, 3, 8, 9 and 10 this seems quite satisfactory. The other six cases do not seem to be approaching zero for long times and the approximation is more severe.

## V. FAR-FIELD DISPLACEMENT SPECTRA

For each of the fourteen sources listed in Table 3.1 we compute far-field displacement spectra. For the one-dimensional, spherically symmetric calculations the equivalent elastic source is the reduced displacement potential,  $\Psi(t-r/\alpha)$ , which is related to the displacement by

$$\bar{u}(R, \omega) = \frac{\hat{\Psi}}{R^2} + \frac{\hat{\dot{\Psi}}}{R\alpha}, \quad (5.1)$$

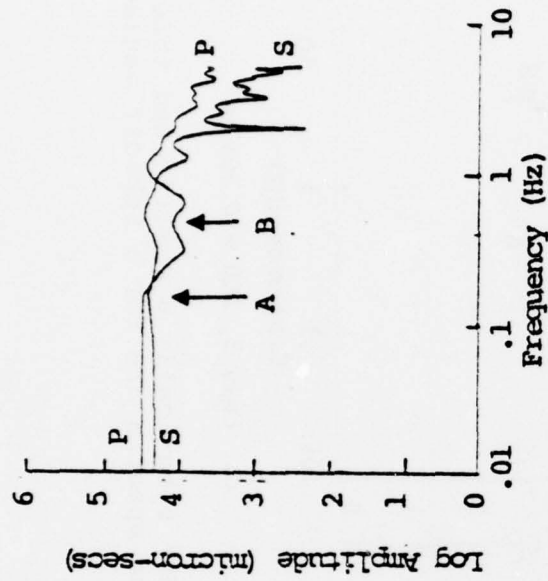
where all quantities are Fourier transformed. Then the far-field displacement spectrum is defined by

$$\bar{u}_{FF}(R, \omega) = \frac{\hat{\dot{\Psi}}}{R\alpha}. \quad (5.2)$$

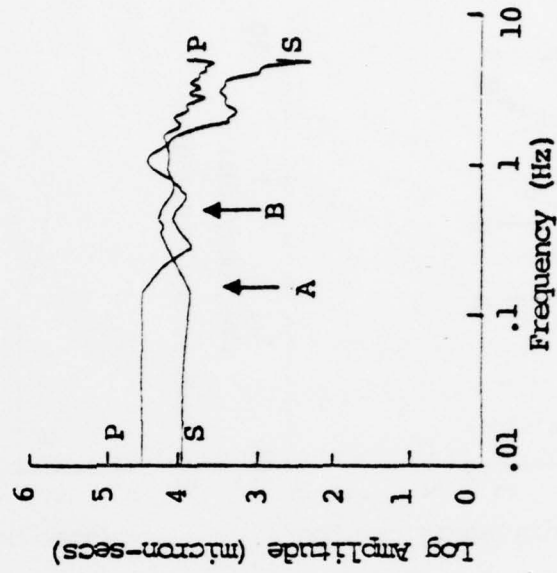
An entirely analogous procedure is followed for the equivalent elastic source representations for the cratering calculations. That is, we retain only terms of order  $R^{-1}$  in the expansion as is explained in Section C.3 of Appendix C.

The displacement spectra are presented in Figures 5.1 through 5.6. The plots are log-log in amplitude versus frequency. Note that the scale on the amplitude axis is in powers of 10 while the actual frequencies are printed on the abscissa. The spectra are shown at two takeoff angles  $\tau$  (see Figure 2.1). The teleseismic body waves are associated with takeoff angles near  $\tau = 20^\circ$ . The  $\tau = 70^\circ$  plots are shown as being representative of the waves trapped as surface wave energy.

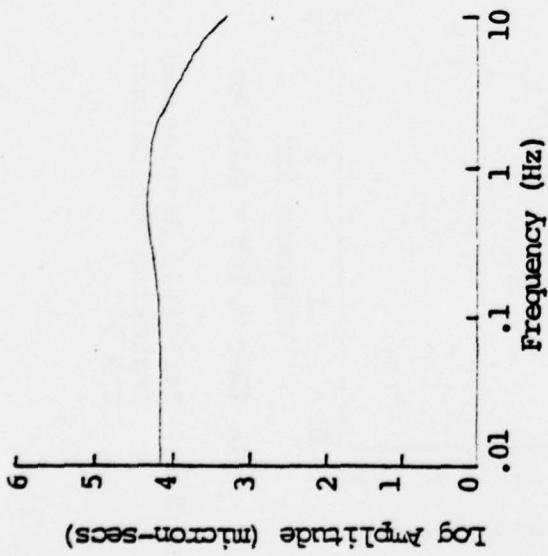
Two frequencies are singled out on the spectra for the cratering calculations and are denoted A and B. The frequency denoted B is associated with the (approximate) total time of the ground motion data provided by ATI. That is, if



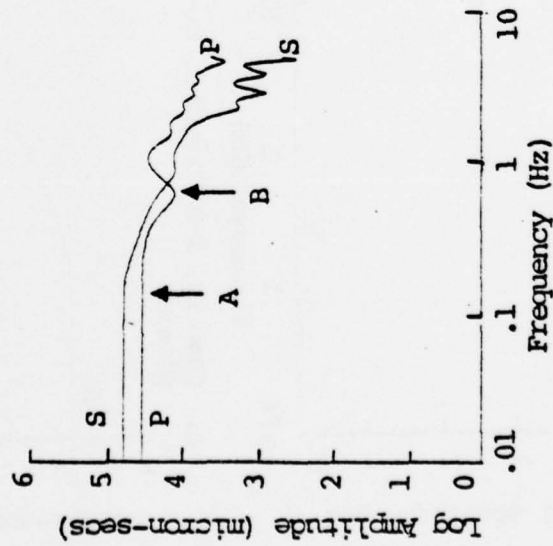
b. Case 1, DOB = 0.159 km



d. Case 3, DOB = 0.253 km



a. Case 13, 1-D Contained Explosion



c. Case 2, DOB = 0.207 km

Figure 5.1. Far-field displacement spectra for one spherically symmetric and three cratering explosions in granite. The spectra are for a takeoff angle  $\tau = 20^\circ$ .

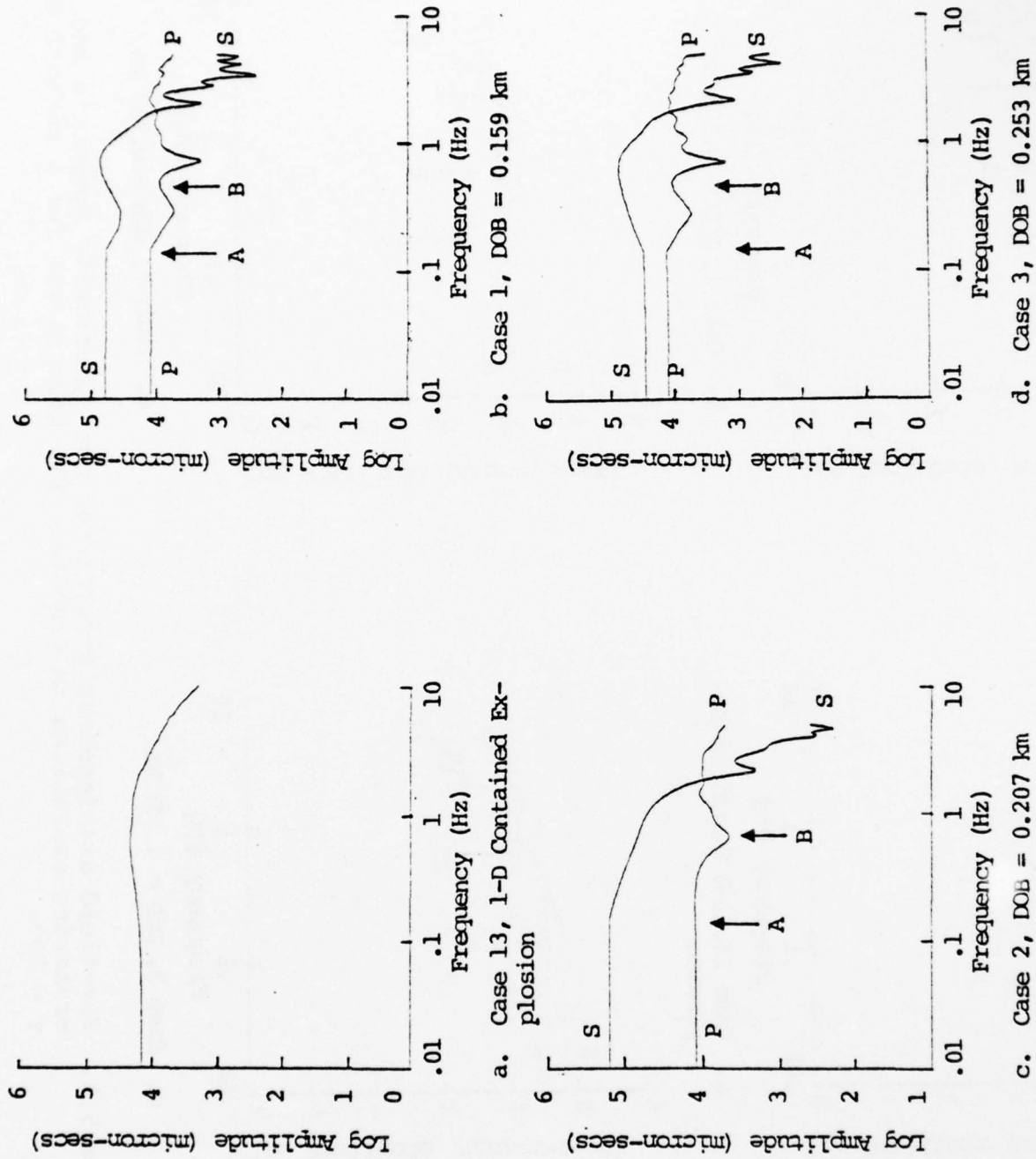
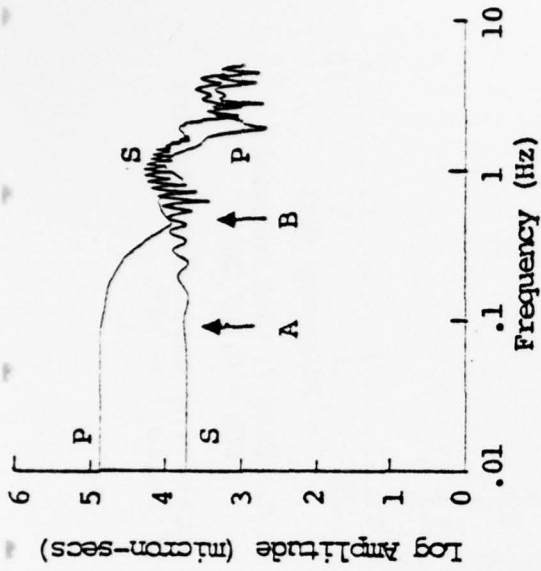
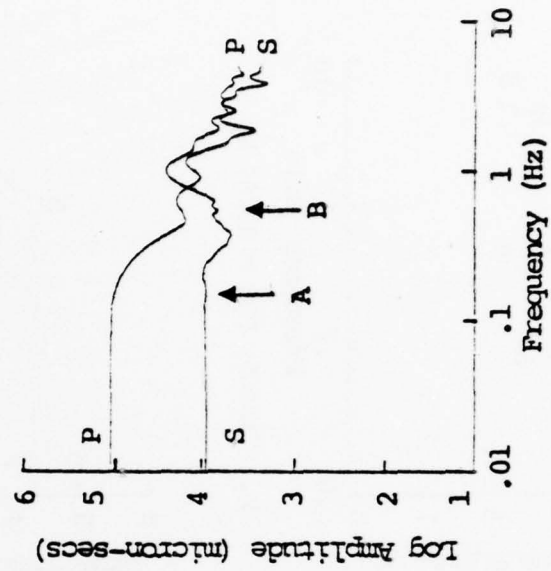
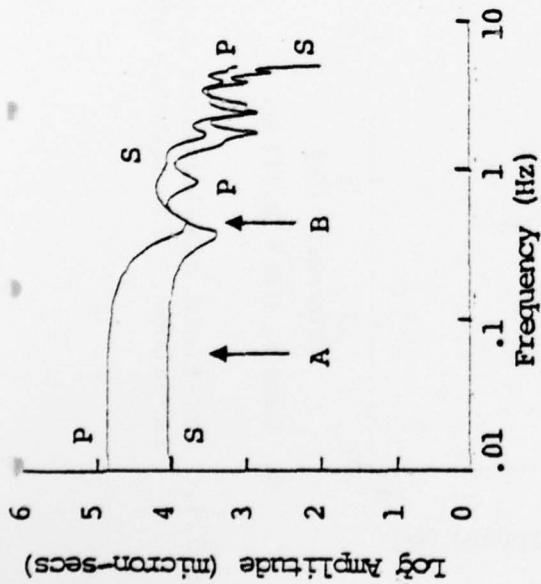


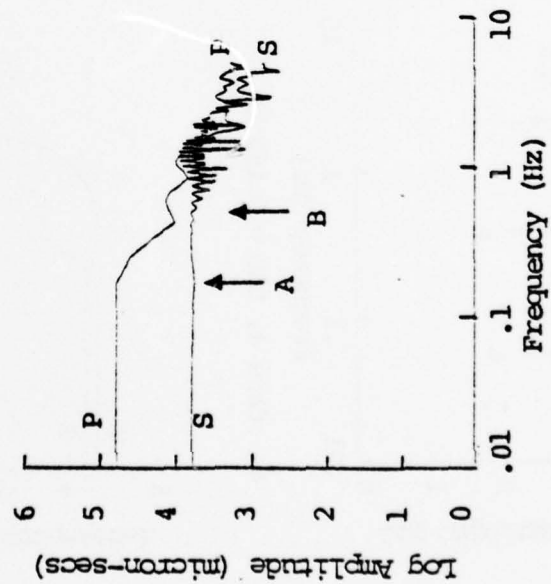
Figure 5.2. Far-field displacement spectra for one spherically symmetric and three cratering explosions in granite. The spectra are for a takeoff angle  $\tau = 70^\circ$ .



b. Case 5, DOB = 0.207 km

d. Case 7, weak material,  
DOB = 0.207 km

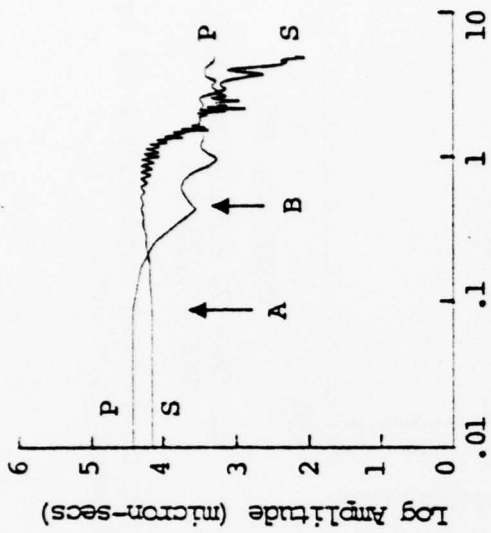
a. Case 4, DOB = 0.159 km



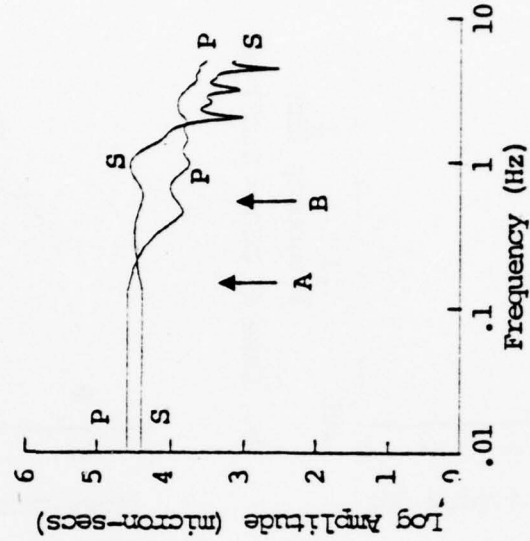
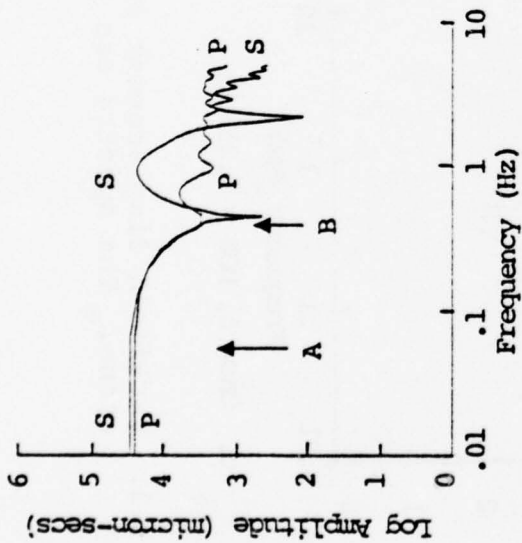
c. Case 6, DOB = 0.253 km

Figure 5.3. Far-field displacement spectra for four cratering explosions in dry sandstone. The spectra are for a takeoff angle  $\tau = 20^\circ$ .

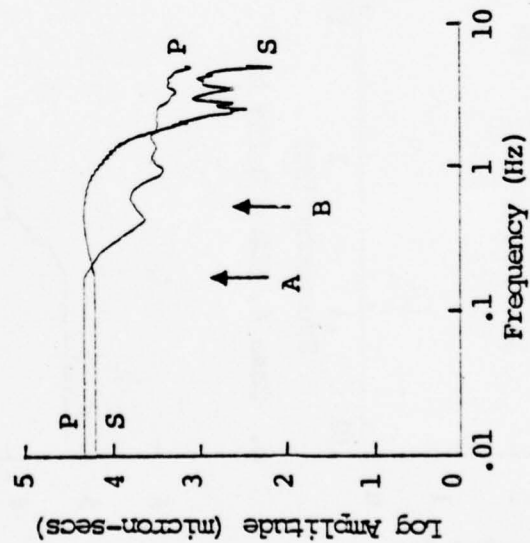




b. Case 5, DOB = 0.207 km

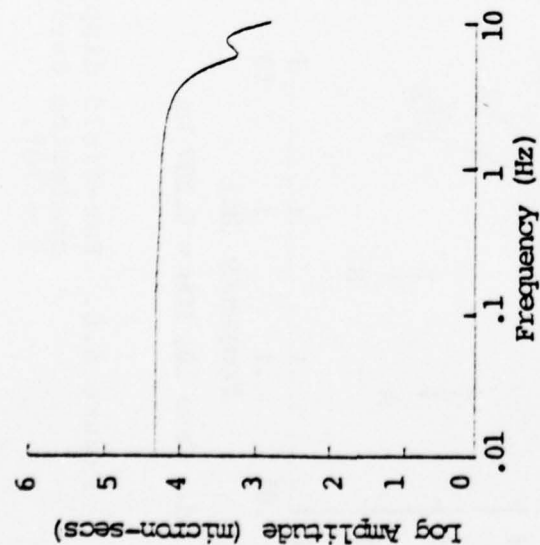
d. Case 7, weak material,  
DOB = 0.207 km

a. Case 4, DOB = 0.159 km

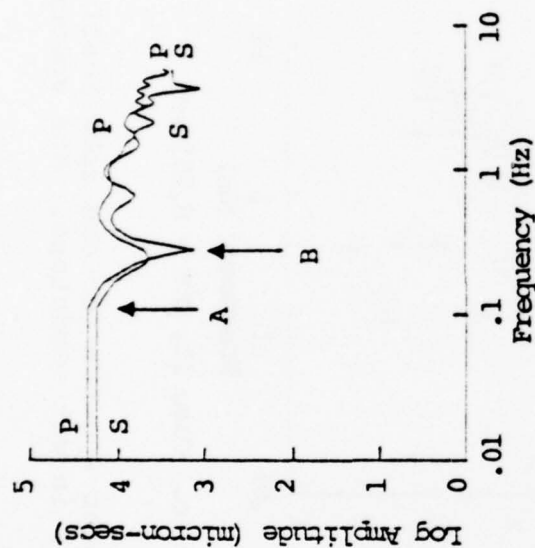


c. Case 6, DOB = 0.253 km

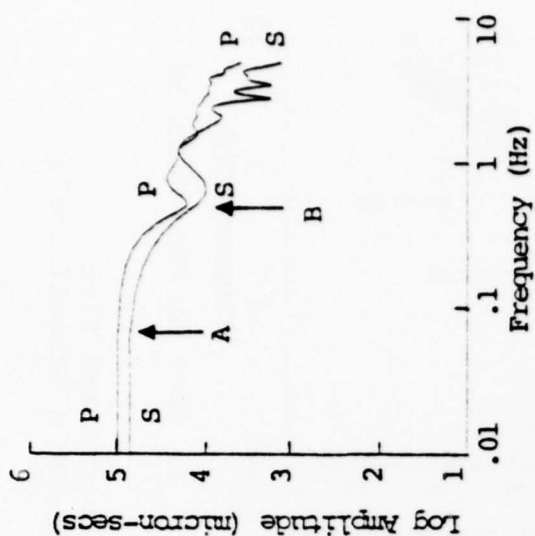
Figure 5.4. Far-field displacement spectra for four cratering explosions in dry sandstone. The spectra are for a takeoff angle  $\tau = 70^\circ$ .



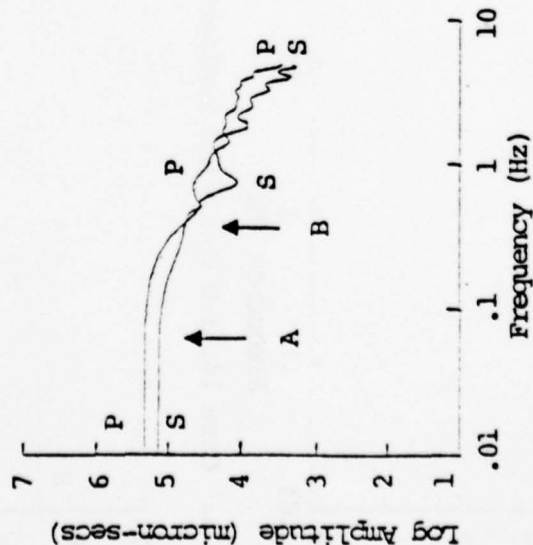
a. Case 14, 1-D Contained Explosion



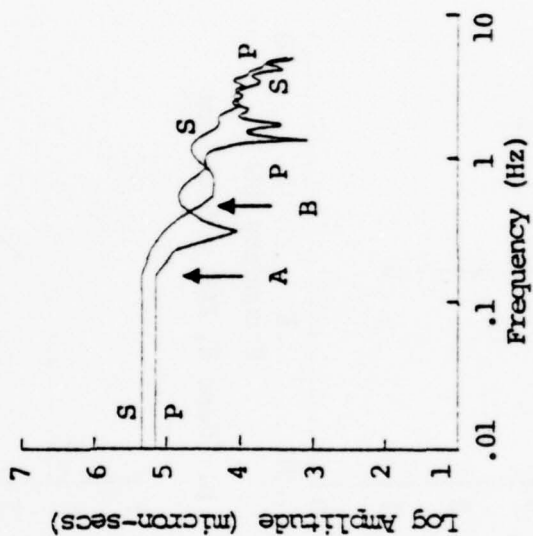
b. Case 8, DOB = 0.053 km



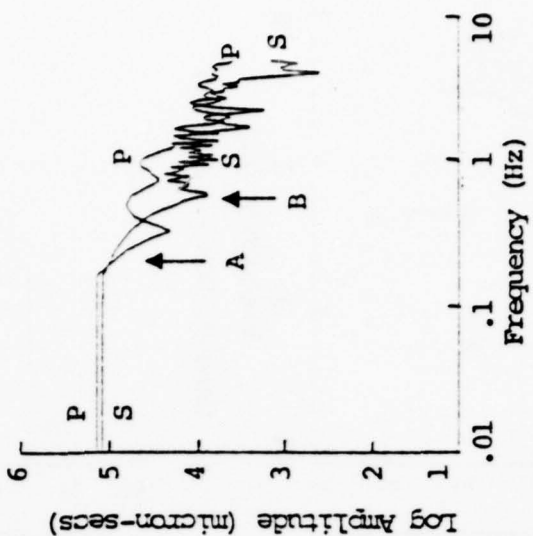
c. Case 9, DOB = 0.159 km



d. Case 10, DOB = 0.207 km

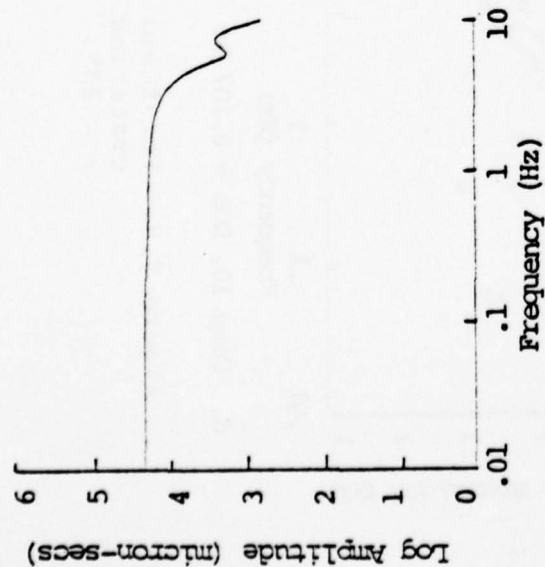


e. Case 11, DOB = 0.253 km

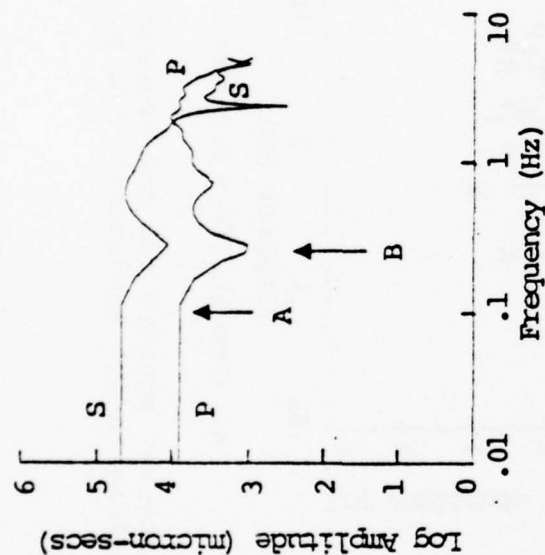


f. Case 12, DOB = 0.531 km

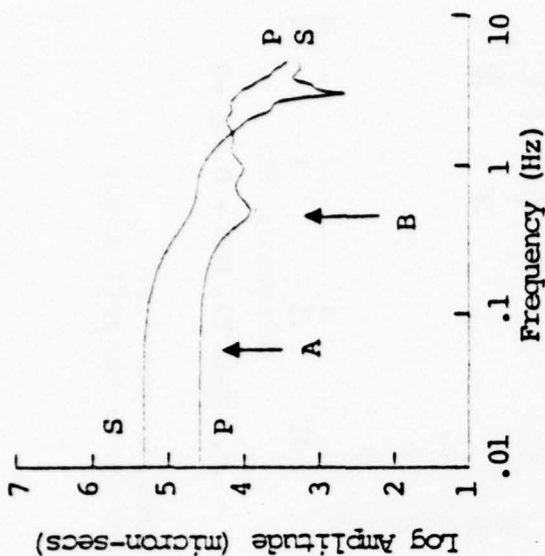
Figure 5.5. Far-field displacement spectra for one spherically symmetric and five cratering explosions in wet sandstone. The spectra are for a takeoff angle  $\tau = 20^\circ$ .



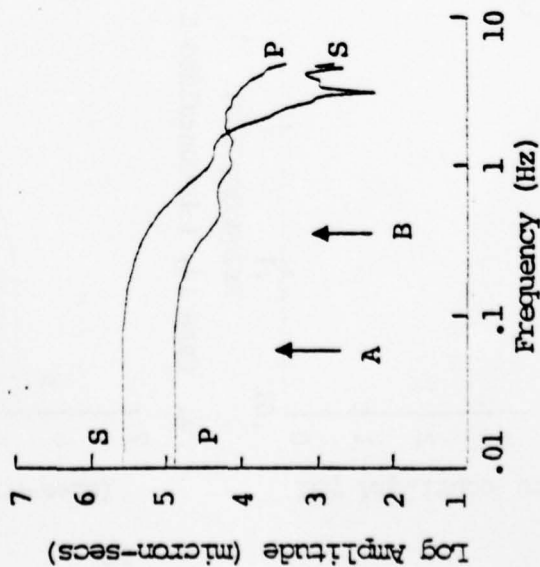
a. Case 14, 1-D Contained Explosion



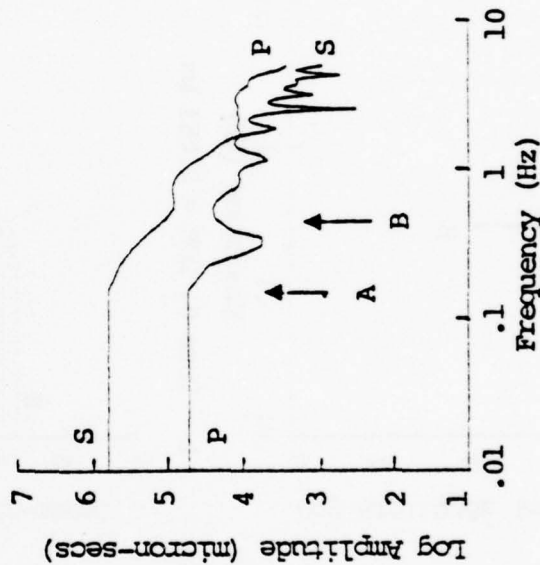
b. Case 8, DOB = 0.053 km



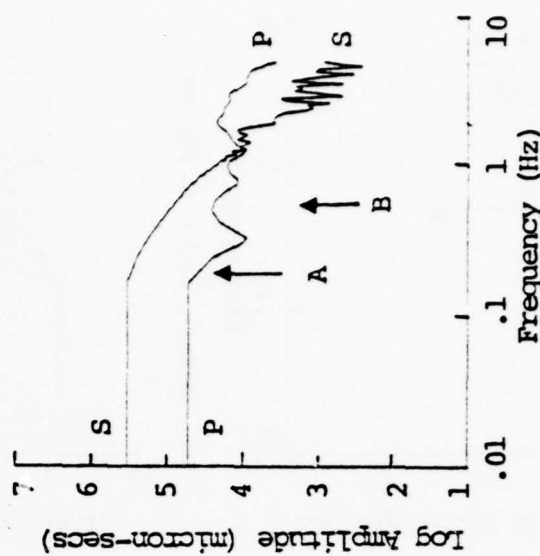
c. Case 9, DOB = 0.159 km



d. Case 10, DOB = 0.207 km



e. Case 11, DOB = 0.253 km



f. Case 12, DOB = 0.531 km

Figure 5.6. Far-field displacement spectra for one spherically symmetric and five cratering explosions in wet sandstone. The spectra are for a takeoff angle  $\tau = 70^\circ$ .

the  $\nabla \cdot \underline{u}(t)$  and  $\nabla \times \underline{u}(t)$  at a typical station on the elastic radius had their first non-zero value at  $t_i = 0.4$  seconds and the final time point was at  $t_f = 2.5$  seconds, we say that the frequency B is  $1/(t_f - t_i)$  or, for this example, 0.48 Hz. Then B is the lowest frequency that can be associated with the actual computed data.

The frequency A is associated with the procedure used to compute the Fourier transforms. As pointed out in the previous section, beyond the time  $t_f$  we assume that the lowest order terms (the dipole) in the expansion of the divergence and curl are zero. The higher order terms are assumed to remain static at the value reached at the last time point. The amplitudes at all frequencies below B are dependent on these assumptions. In order to compute the Fourier transform we extend the time histories out to some  $t_e$  using the assumptions mentioned above. Then  $A \approx 1/(t_e - t_i)$ .

How do we compute values for frequencies below A? We know that the response at low frequencies is dominated by the dipole term in the expansion. Further, in Section 4.2 we showed that the dipole term must behave like  $\omega^2$  at low frequencies for a bounded solution. This corresponds to a flat far-field displacement spectrum at low frequencies. Our procedure is then to extrapolate the amplitude of the dipole term from its value at A by assuming proportionality to  $\omega^2$ . This is nearly the same as assuming the far-field displacement spectrum to be flat to long periods from its value at A as can be seen in the figures.

All the P wave spectra shown are quite well behaved, though the high frequency portion shows considerable modulation. However, some of the S wave spectra are rapidly oscillating in a manner indicative of numerical error. Cases 5, 6 and 12 are the worst cases. The oscillations are apparently due to some incompatibility between the dipole and

higher order terms. We can ignore this trouble because only the portion of the S wave spectrum below, say, 0.1 Hz has any influence on our calculations. The S waves cannot influence the body waves (see Section VI), so we need not worry about errors in the higher frequency region.

Finally, in Tables 5.1 and 5.2 we tabulate the spectral values that have the greatest significance for computing teleseismic body and surface waves. The amplitude values in these tables are all on the same scale (all have been multiplied by  $10^{-4}$  R) and are best viewed as relative amplitudes. The reliability of these values for scaling  $m_b$  and  $M_s$  is discussed in Sections VI and VII.



TABLE 5.1

BODY WAVE AMPLITUDE SPECTRA - FAR-FIELD P WAVE  
 1 HZ SPECTRAL AMPLITUDES AT  $\tau = 20^\circ$

<u>Identifier</u>	<u>Material</u>	<u>Depth (km)</u>	<u>Spectral Amplitude</u>
13	Granite	Spherically Symmetric	1.8
1	"	0.159	1.8
2	"	0.207	2.1
3	"	0.253	1.5
4	Dry Sandstone	0.159	0.60
5	"	0.207	0.65
6	"	0.253	0.72
7	Weak Dry Sand- stone	0.207	1.4
14	Wet Sandstone	Spherically Symmetric	1.7
8	"	0.053	1.3
9	"	0.159	2.1
10	"	0.207	2.8
11	"	0.253	2.7
12	"	0.531	2.5

TABLE 5.2  
SURFACE WAVE AMPLITUDE SPECTRA (0.05 Hz)

<u>Identifier</u>	<u>P(<math>\tau=20^\circ</math>)</u>	<u>S(<math>\tau=20^\circ</math>)</u>	<u>P(<math>\tau=70^\circ</math>)</u>	<u>S(<math>\tau=70^\circ</math>)</u>	<u>S/P (70°)</u>
13	1.3	-	1.3	-	-
1	2.9	2.0	1.1	5.4	4.9
2	3.2	5.7	1.2	15.6	13.0
3	3.3	0.9	1.2	2.7	2.3
4	6.5	1.1	2.4	2.8	1.2
5	7.1	5.0	2.6	1.4	0.54
6	5.6	5.7	2.1	1.6	0.76
7	10.6	0.95	3.9	2.4	0.62
14	2.0	-	2.0	-	-
8	2.2	1.7	0.78	4.6	5.9
9	10.1	7.4	3.7	20.2	5.5
10	21.3	13.6	7.7	37.8	4.9
11	14.4	22.0	5.2	60.1	11.6
12	13.7	11.8	5.0	32.5	6.5

VI. BODY WAVE MAGNITUDE,  $m_b$ 

In this section we present our synthetic seismograms for the fourteen ATI sources and give the  $m_b$  values for each. The synthetic seismogram calculations include the following elements:

1. The equivalent elastic sources which give the (whole space) far-field displacement spectra described in the previous section are embedded in a layered model of the crust in the source region. The basic model used for the calculations is tabulated in Table 6.1. The top layer was changed to have the properties appropriate to each source as listed in Table 2.1. In carrying out the calculations only the downgoing waves emitted by the source are computed; that is, no free surface is included in the source crustal model.
2. The far-field body waves emanating from the base of the source crust and characterized by ray parameter  $p = 0.079$  sec/km are calculated.
3. The upper mantle is accounted for by a step function response computed using generalized ray theory. In this case we took the distance to be  $\Delta = 36^\circ$  which is beyond the upper mantle triplications and the upper mantle response is essentially a constant geometric spreading factor with a value of about  $0.95 \times 10^{-4}$ .
4. The response of the receiver crustal model (Table 6.2) is included. In this case the receiver crust has little effect other than scaling the seismogram proportional to the velocity of the top few kilometers.

TABLE 6.1  
SOURCE REGION CRUSTAL MODEL

<u>Depth (km)</u>	<u>Thickness (km)</u>	<u><math>\alpha</math> (km/sec)</u>	<u><math>\beta</math> (km/sec)</u>	<u><math>\rho</math> (g/cm<sup>3</sup>)</u>
1.0	1.0	Granite, Wet or Dry Sandstone		
1.7	0.7	4.7	2.7	2.6
2.7	1.0	5.4	2.8	2.7
4.0	1.3	5.8	3.45	2.8
20.0	16.0	6.0	3.50	2.8

TABLE 6.2  
RECEIVER REGION CRUSTAL STRUCTURE

<u>Depth (km)</u>	<u>Thickness (km)</u>	<u><math>\alpha</math> (km/sec)</u>	<u><math>\beta</math> (km/sec)</u>	<u><math>\rho</math> (km/sec)</u>
2.58	2.58	3.67	2.31	2.40
4.84	2.26	5.42	3.27	2.60
11.61	6.77	5.80	3.45	2.60
20.0	8.39	6.00	3.50	2.80

5. The response is convolved with an operator representing the attenuation and dispersive properties of the earth. For these calculations we took  $t^* = 0.7$  ( $t^*$  is the ratio of travel time to the effective path attenuation factor,  $Q$ ).
6. The ground motion is convolved with the response of a standard short period seismograph system.

The synthetic seismograms are shown in Figures 6.1 and 6.2. The cycle from which  $m_b$  is measured is indicated on each record by a bar. The  $m_b$  values and the period of the  $m_b$  cycle are tabulated in Table 6.3. The  $m_b$  is computed from

$$m_b = \log \frac{A}{T} + 3.32, \quad (6.1)$$

where  $T$  is the period tabulated,  $A$  is the peak-to-peak amplitude of the indicated cycle corrected for the instrument response at the period  $T$ , and the constant 3.32 is the appropriate distance correction factor. Recall that for all the seismogram calculations there is no free surface near the source.

The seismograms of Figures 6.1-6.3 are quite typical of short period teleseismic recordings of explosions. The only anomaly seems to be for the dry sandstone events for which the seismograms are in Figure 6.2. Note that the apparent first motion in these seismograms is downward; or at least the upward motion is too small to be noticed. This seems to be a consequence of the negative offset of the dominant term,  $A_{10}^{(4)}$ , that was discussed in connection with Figure 4.2.

One other point should be made about the short period seismograms and  $m_b$ . The S wave contribution to the seismograms is negligible. The only way the S wave energy leaving the source can affect the seismograms is through converted



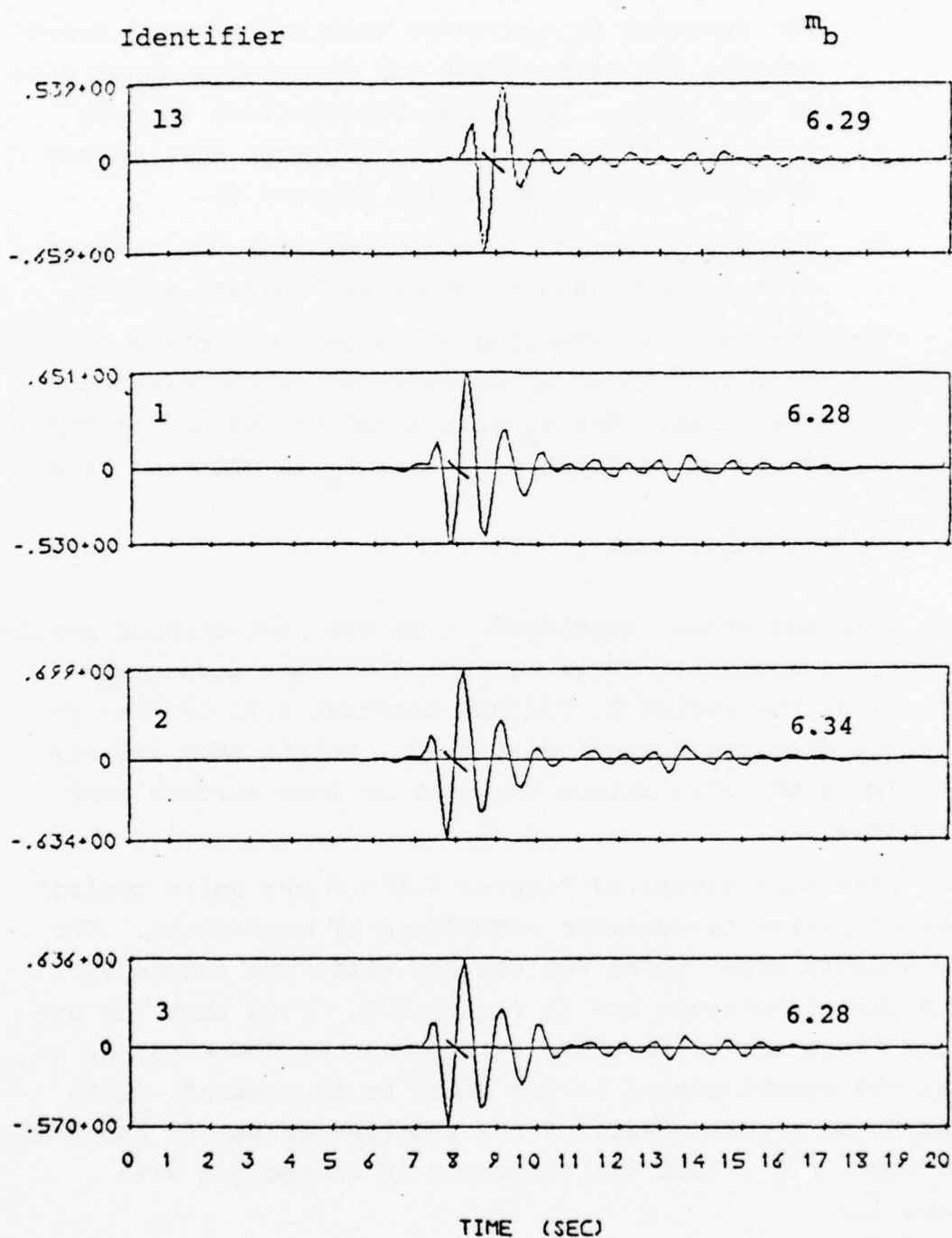


Figure 6.1. Synthetic short period seismograms for one spherically symmetric and three cratering calculations in granite. The numbers to the left are ground motion in microns at 1 Hz.

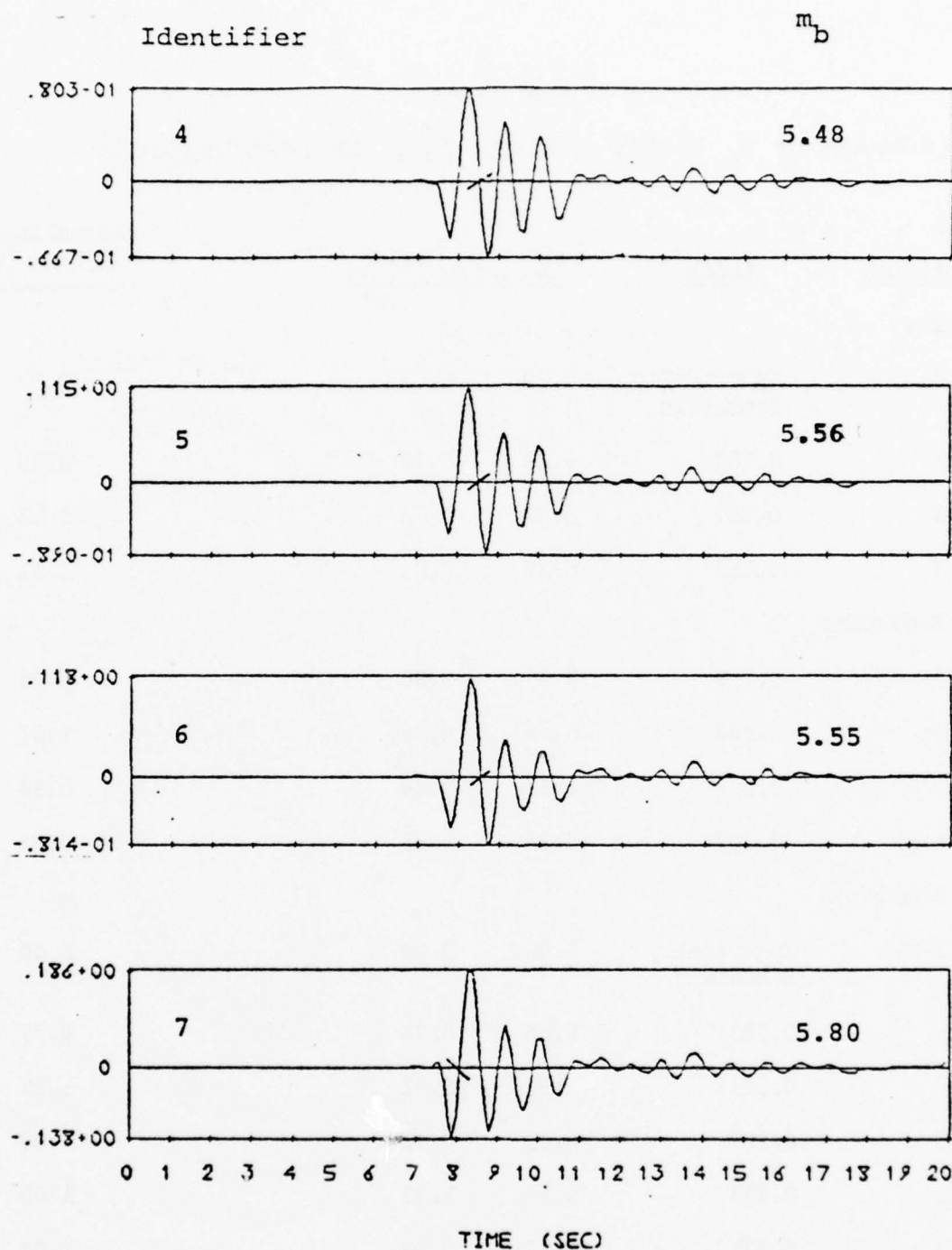


Figure 6.2. Synthetic short period seismograms for four cratering calculations in dry sandstone. The numbers to the left are ground motion in microns at 1 Hz. Note that the apparent first motion is downward. This appears to be a consequence of the constitutive properties of the dry sandstone.

TABLE 6.3  
SUMMARY OF  $m_b$  VALUES FOR ATI CRATERING CALCULATIONS

<u>Identifier</u>	<u>Depth</u>	<u><math>m_b</math></u>	<u><math>m_b</math> Period</u>	<u>Normalized (A/T)/(<math>\alpha_s^2 u</math>)</u>
Granite				
13	Spherically Symmetric	6.29	0.81	0.93
1	0.159	6.28	0.78	0.85
2	0.207	6.34	0.82	0.82
3	0.253	6.28	0.80	1.01
Dry Sandstone				
4	0.159	5.48	0.96	0.96
5	0.207	5.56	0.88	1.09
6	0.253	5.55	0.86	0.94
7 (weak)	0.207	5.80	0.93	0.86
Wet Sandstone				
14 (1-D)	Spherically Symmetric	5.88	0.79	1.00
8	0.053	5.66	0.94	0.79
9	0.159	5.98	0.92	1.02
10	0.207	6.11	0.92	1.05
11	0.253	6.10	1.03	1.05
12	0.531	6.15	0.99	1.27

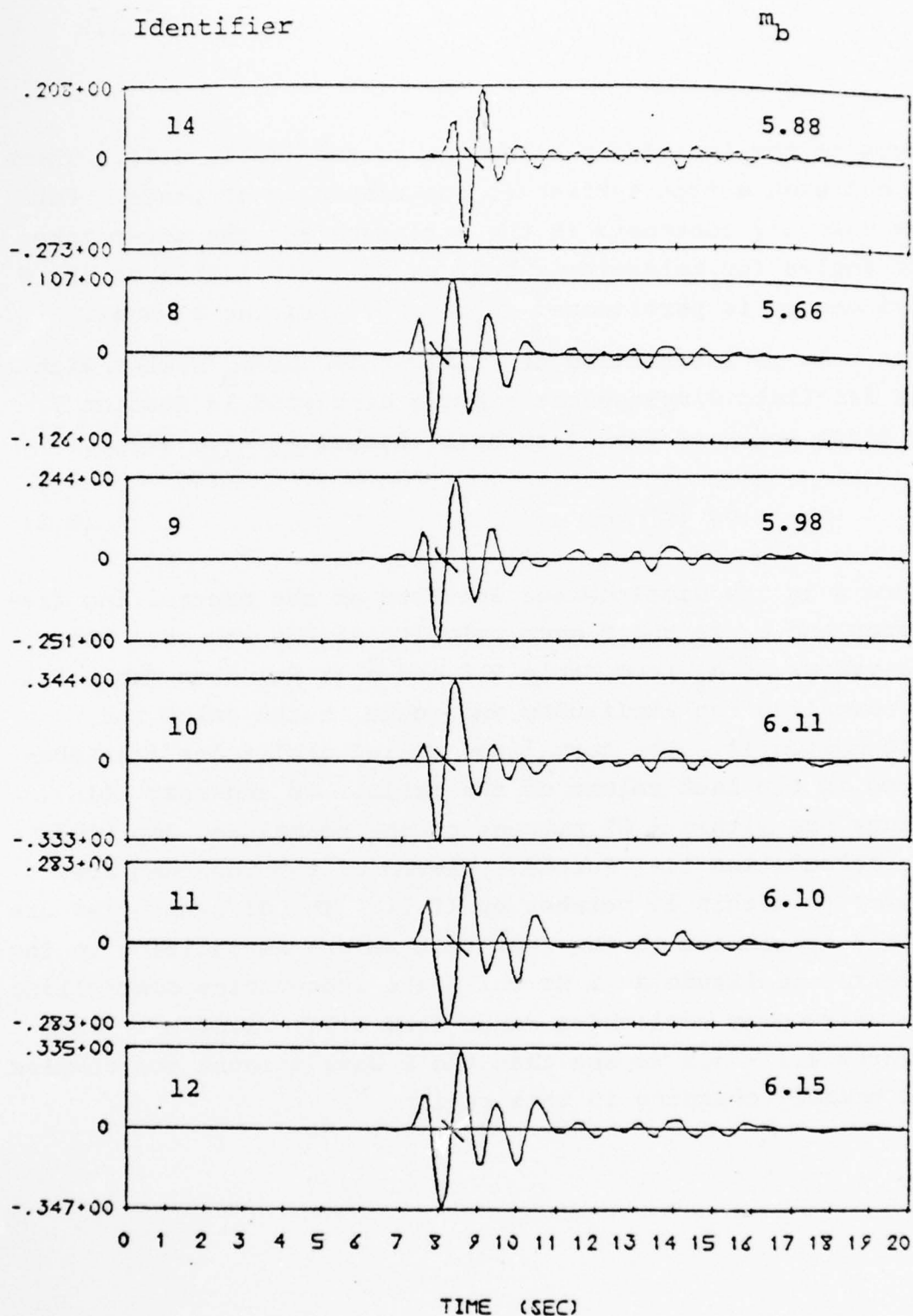


Figure 6.3. Synthetic short period seismograms for one spherically symmetric and five cratering calculations in wet sandstone. The numbers to the left are ground motion in microns at 1 Hz.

waves at the interfaces below the source (Table 6.1). There is not even a free surface to contribute an sP phase. For the velocity contrasts in the structure and the steep take-off angles for teleseismic body waves, very little of the S wave energy is partitioned into early arriving P waves.

It is interesting to examine how the  $m_b$  scales with the far-field displacement spectra discussed in Section V. To first order we expect to have [Bache, et al., 1976],

$$m_b \approx \log \left( \alpha_s^2 \hat{u} \right), \quad (6.2)$$

where  $\hat{u}$  is the displacement spectrum at the controlling frequency and  $\alpha_s$  is the P wave velocity at the source. Using the values of  $\alpha_s$  from Table 2.1 and  $\hat{u}$  (1 Hz) from Table 5.1, we normalize the amplitudes and scale to the value for calculation 14. The normalized scaled amplitudes are tabulated in the last column of the table. We see that all values are within  $\pm 27$  percent of the normalized amplitude for calculation 14. Further, eleven of the fourteen are scaled to within 15 percent by (6.2). The discrepancies are mainly attributed to the fact that we are normalizing to the spectral amplitude at 1 Hz while the frequencies controlling the seismogram amplitudes range from 0.97 - 1.32 Hz. From Figures 4.1 - 4.6 we see that the P wave spectra are complex and rapidly changing in this region.



VII. SURFACE WAVE MAGNITUDE,  $M_s$ 

In this section we present our synthetic long period seismograms for the fourteen ATI sources and give the  $M_s$  values for each. The synthetic seismogram calculations include the following elements:

1. The method for the surface wave calculations is described by Harkrider [1964] and Harkrider and Archambeau [1977]. The same equivalent elastic source formulation used for the body waves is used for the surface waves. Once again, only the down-going waves from the source are included in the calculations.
2. Two crustal models are used for the path, one for the very near source region and one for the remainder of the path to the receiver. The average path model is one proposed for North America by McEvelly [1964]. The only difference between the models is that the top three kilometers of the source region crustal model is replaced by the ATI granite, wet or dry sandstone, depending on the source material. For the long periods controlling teleseismic  $M_s$  the reflection coefficient for Rayleigh waves passing across the boundary between the source and average path crustal model is close to unity.
3. The ground motion is convolved with the response of an LRSM long period seismometer. A Q operator which has only a minor effect is also included. The Q model is that of Tryggvason [1965].
4. The seismograms were synthesized at a range of 3000 km. The  $M_s$  was computed using the formulas of Marshall and Basham [1972]. For this range

the formula reduces to

$$M_s = \log A + 1.38 + P(T)$$

where  $A$  is the maximum amplitude (zero-to-peak) of the signal with period near 20 seconds and  $P(T)$  is a period dependent path correction tabulated by Marshall and Basham [1972]. The correction is quite small for periods near 20 seconds.

The vertical component Rayleigh wave synthetic seismograms are shown in Figures 7.1 - 7.3. Two seismograms are shown for the spherically symmetric contained explosions in granite and wet sandstone (Cases 13 and 14). In one of these (13b, 14b) only the downward waves are included in the calculation. The seismograms are then the analog of the Cases 13 and 14 body wave seismograms of Figures 6.1 and 6.3. Since the  $M_s$  is relatively insensitive to depth for contained explosions (unlike  $m_b$  which is strongly affected by the pP phase), we also compute seismograms for fully contained explosions at a depth of 200 meters. The seismograms are given as Cases 13a and 14a.

The important data from the seismograms of Figures 7.1 - 7.3 are summarized in Table 7.1. The phase at which the amplitude for  $M_s$  was measured is indicated on the seismograms by a bar. The period of this phase is given in the table. Also listed in the table is the spectral amplitude of the true ground motion at a period of 20 seconds. The difference between  $M_s$  and  $\log \hat{A}$  indicates the consistency to which the  $M_s$  measurement represents a true measurement of the energy at frequencies in this range. These differences are tabulated in the last column of Table 7.1. We see that the  $M_s$  values are quite consistent with the spectral measurements with the spread between the maximum and minimum values being 0.14  $M_s$  units.

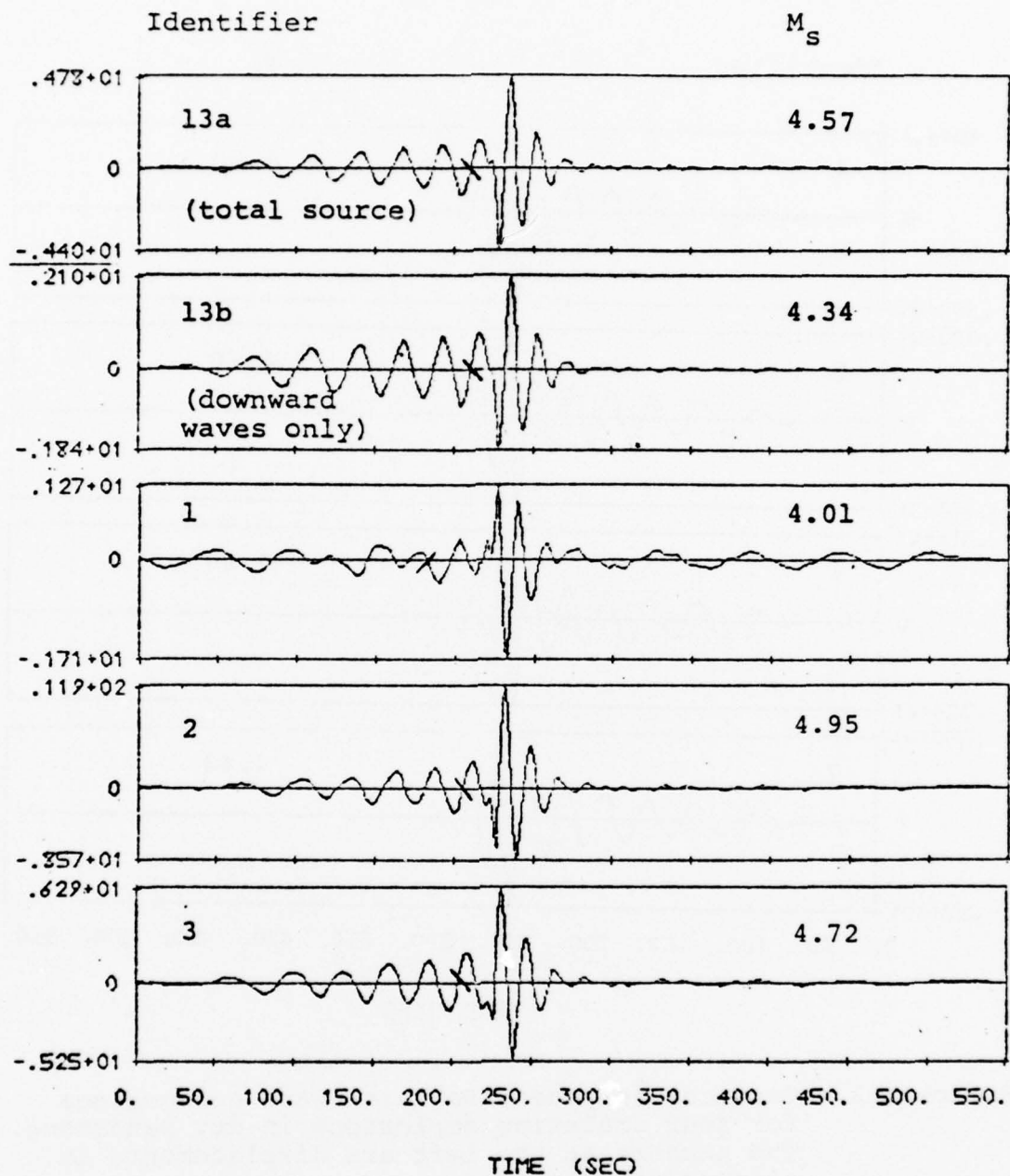


Figure 7.1. Vertical component Rayleigh wave seismograms for a spherically symmetric and three cratering explosions in granite. The numbers at the left are displacements in microns at 25 seconds.

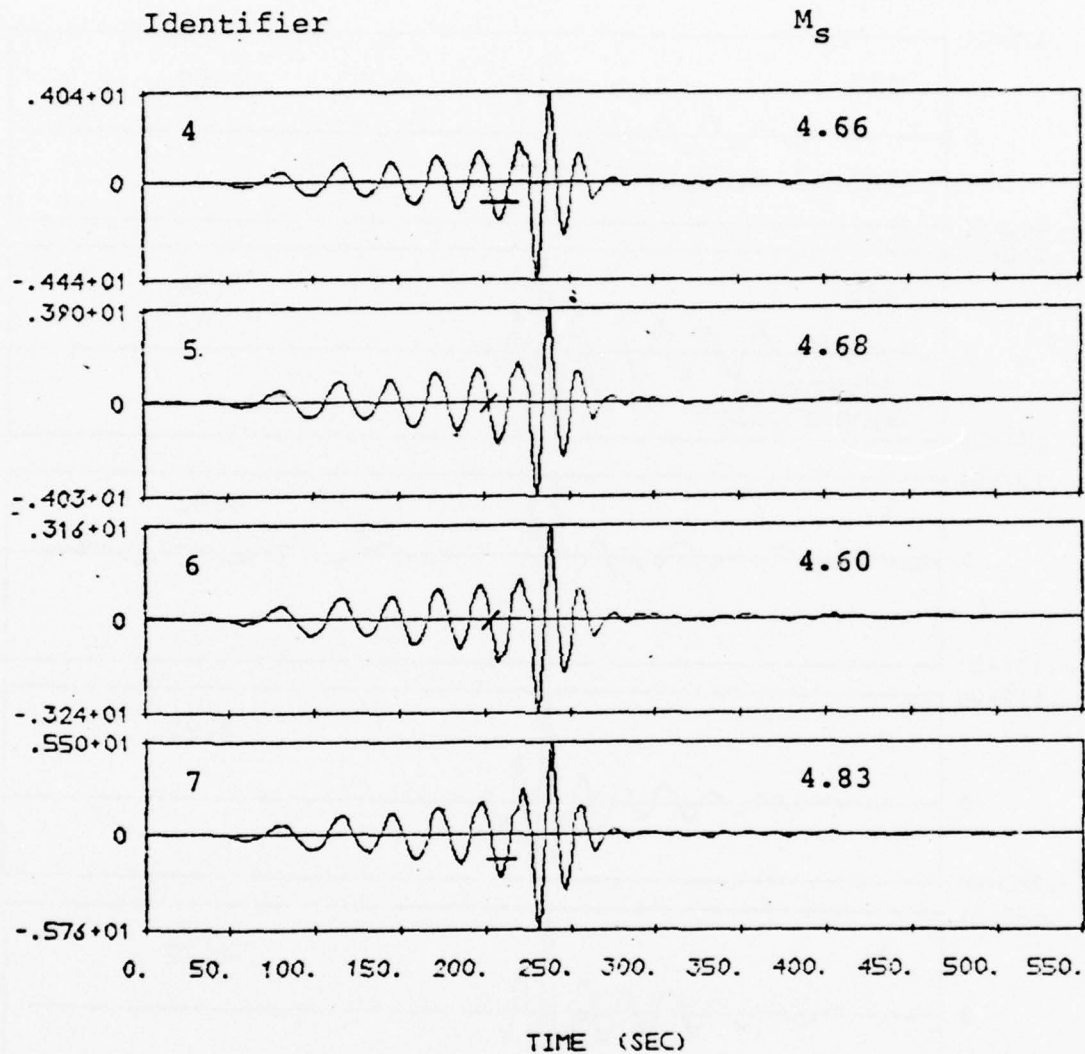


Figure 7.2. Vertical component Rayleigh wave seismograms for four cratering explosions in dry sandstone. The numbers at the left are displacements in microns at 25 seconds.

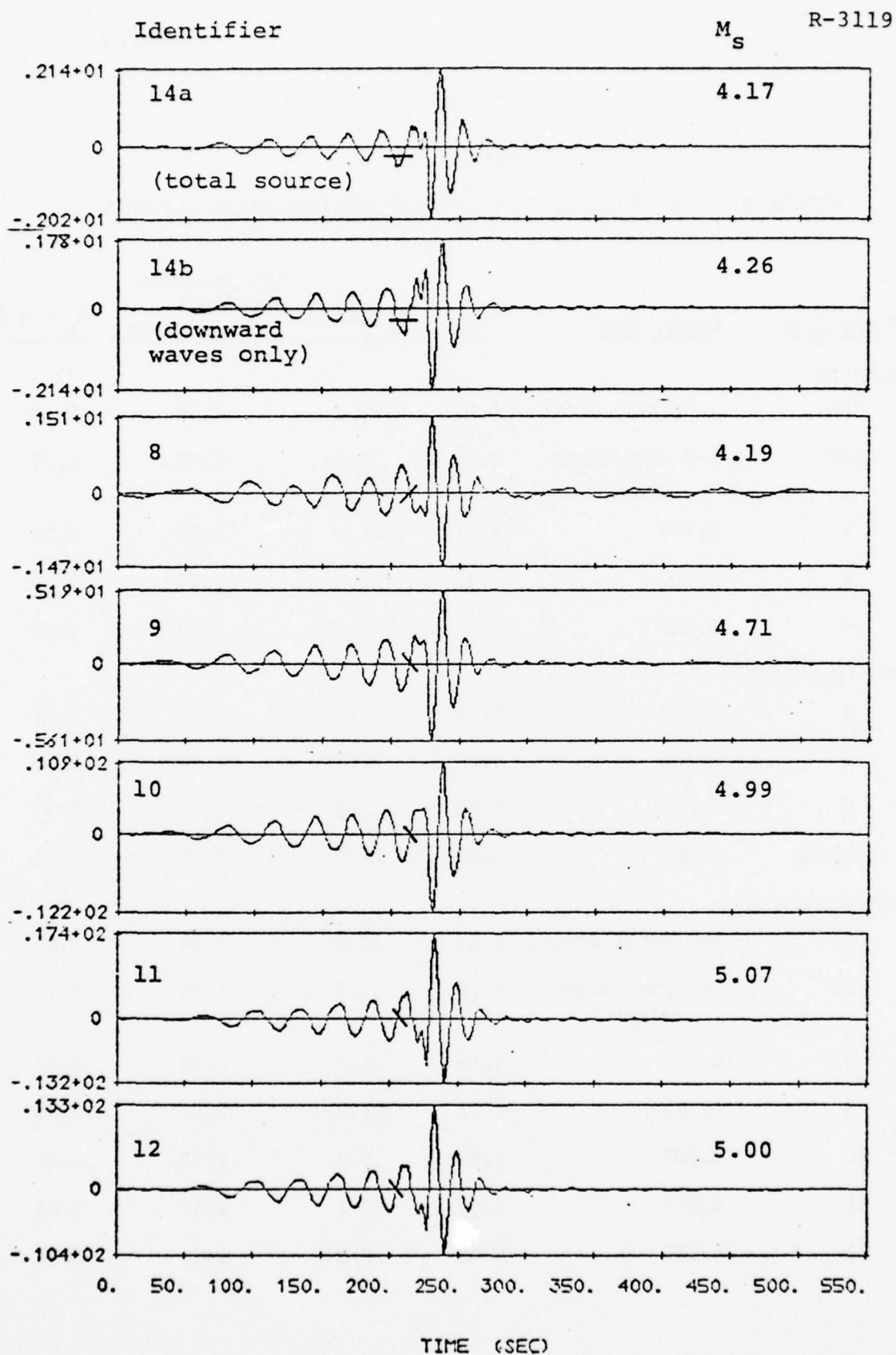


Figure 7.3. Vertical component Rayleigh wave seismograms for a spherically symmetric and five cratering explosions in wet sandstone. The numbers at the left are displacements in microns at 25 seconds.



TABLE 7.1  
SUMMARY OF  $M_s$  VALUES FOR ATI CRATERING CALCULATIONS

<u>Identifier</u>	<u>Depth (km)</u>	<u><math>M_s</math></u>	<u><math>M_s</math> Period</u>	<u>Log Spectral Amplitude, <math>\log \hat{A}</math> (20 sec)</u>	<u><math>M_s - \log \hat{A}</math></u>
Granite					
13A	1-D Total Source	4.57	20.1	1.92	2.65
13B	1-D Down Waves Only	4.34	21.5	1.62	2.72
1	0.159	4.01	20.0	1.30	2.71
2	0.207	4.95	23.6	2.25	2.70
3	0.253	4.72	21.8	2.03	2.69
Dry Sandstone					
4	0.159	4.66	22.0	1.92	2.74
5	0.207	4.68	22.7	1.92	2.76
6	0.253	4.60	22.5	1.83	2.77
7 (weak)	0.207	4.83	22.0	2.07	2.76
Wet Sandstone					
14A	1-D Total Source	4.17	22.8	1.52	2.65
14B	1-D Down Waves Only	4.26	20.0	1.53	2.73
8	0.053	4.19	21.2	1.43	2.76
9	0.159	4.71	21.2	2.02	2.69
10	0.207	4.99	19.3	2.35	2.64
11	0.253	5.07	20.1	2.44	2.63
12	0.531	5.00	19.8	2.34	2.66

Which portions of the wave field are most important for the  $M_s$ ? This is an important question since we have more confidence in some portions of the calculation than others. In particular, we expect the P waves to be computed much more accurately than the S waves in our equivalent elastic source calculation.

In Figure 7.4 we show surface wave seismograms for several cases in which the S wave portion of the field has been suppressed. The important data from these seismograms is tabulated in Table 7.2. We see that the relationship between spectral amplitudes and  $M_s$  is essentially the same as for the total field seismograms in Table 7.1.

The next step is to compare the S-suppressed seismograms to the total wave records and relate the results to the amount of S waves present in the source. This is done in Table 7.3. The S/P ratios are for the spectra at  $\tau = 70^\circ$  and are taken from Table 5.2. The cases we have selected span the range of possibilities. For granite and wet sandstone we have the cases with the most and least S wave component. The dry sandstone case has the least S waves of all those studied.

From Table 7.3 we see that if the S waves are overestimated for Case 2, and study of the spectra in Figure 4.2 indicates they may well be, we may be overestimating  $M_s$  by 0.2-0.3 magnitude units. Case 2 is by far the worst case. The S waves seem to have little effect on  $M_s$  for the dry sandstone calculations. For wet sandstone the smaller S/P ratio acts to degrade  $M_s$  while the larger ratio acts to increase it. For the other three cases with S/P between the extremes, the S waves are not likely to be too important.

TABLE 7.2

SURFACE WAVE DATA FROM THE SEISMOGRAMS OF FIGURE 7.4

<u>Identifier</u>	$M_s^P$	$M_s^P$ Period	Log Spectral Amplitude, <u>log A (20 sec)</u>	$M_s^P - \log \hat{A}^P$
Granite				
2	4.55	21.6	1.89	2.66
3	4.56	21.7	1.96	2.66
Dry Sandstone				
5	4.64	21.8	1.93	2.71
Wet Sandstone				
10	5.12	22.1	2.41	2.71
11	4.96	22.3	2.24	2.72

TABLE 7.3

COMPARISON OF DATA FOR TOTAL SOURCE AND S-SUPPRESSED  
SURFACE WAVE SEISMOGRAMS

<u>Identifier</u>	<u>S/P</u>	$M_s^T - M_s^P$	<u>log <math>\hat{A}^T - \log \hat{A}^P</math></u>
Granite			
2	13.0	0.40	0.36
3	2.3	0.16	0.13
Dry Sandstone			
5	0.54	0.04	-0.01
Wet Sandstone			
10	4.9	-0.13	-0.06
11	11.6	0.11	0.20

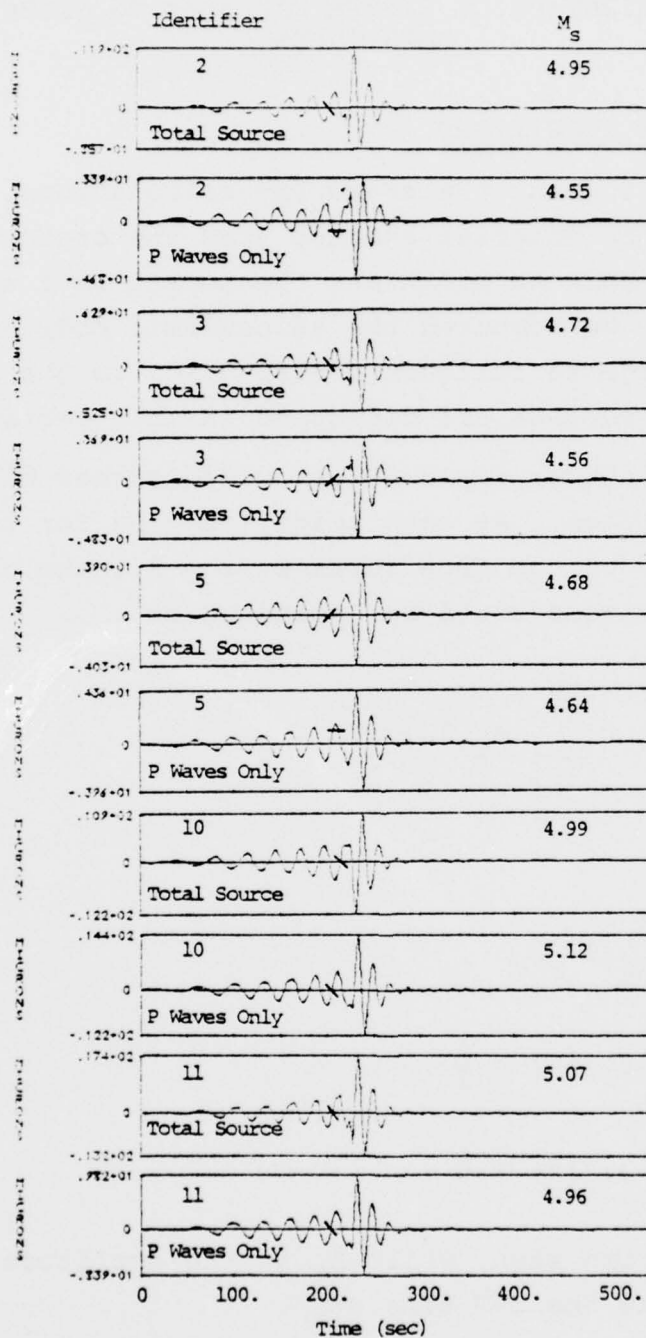


Figure 7.4. Vertical component Rayleigh wave seismograms at 3000 km for five of the cratering calculations. The first record of each pair is taken from Figures 7.1-7.3. The second record is for the same source with the S wave portion suppressed.

# VIII. CONTRIBUTION OF EJECTA FALLBACK TO TELESEISMIC MAGNITUDES

## 8.1 BOUNDARY CONDITIONS

In carrying out the cratering calculations, ATI also kept track of the material ejected from the crater. This material falls back to earth and the impact is a source of seismic waves. We computed the teleseismic body and surface waves for the ejecta fallback contribution to the cratering source and the results are discussed in this section.

For the ejecta field ATI provided stress histories on the free surface. At each point (or ring for this axisymmetric problem) on the free surface,  $r = r'$ , the time history of the normal stress could be expressed as

$$P_0(r', t) = \sum_{i=1}^N A_i \Pi(\tau_i) \quad (8.1)$$

where

$$\tau_i = \frac{t - t_i}{\Delta t},$$

$$\Pi(x) = \begin{cases} 1, & |x| < \frac{1}{2}, \\ 0, & |x| > \frac{1}{2}, \end{cases}$$

and  $\Delta t$  is the time step, while  $A_i$  is the amplitude of the normal stress at the  $i$ th time step.

We observe that

$$\mathcal{F}\{\Pi(\tau_i)\} = \int_{-\infty}^{\infty} \Pi\left(\frac{t - t_i}{\Delta t}\right) e^{-i\omega t} dt = 2 \frac{\sin\left(\frac{\omega \Delta t}{2}\right)}{\omega} e^{-i\omega t_i}. \quad (8.2)$$



Then the normal stress boundary condition applied at  $r = r'$  is

$$P_0(r', \omega) = \frac{2 \sin(\frac{\omega \Delta t}{2})}{\omega} \sum_{i=1}^N A_i e^{-i\omega t_i}, \quad (8.3a)$$

and for the shear stress it is

$$Q_0(r', \omega) = \frac{2 \sin(\frac{\omega \Delta t}{2})}{\omega} \sum_{i=1}^N B_i e^{-i\omega t_i}, \quad (8.3b)$$

where  $B_i$  is the amplitude of the applied shear stress at the  $i$ th time step.

The boundary conditions (8.3) are in the correct form for applying the theory developed in Appendix E. The total stresses on the surface enter the solution via the spatial integrals (33) of that Appendix. The quadrature is straightforward since the spatial dependence of the stresses is also in terms of rectangle functions. For example, for the normal stresses it is necessary to compute

$$\hat{P}(\omega_k) = \int_0^b P_0(r', \omega) J_0(k_{R_k} r') r' dr' \quad (8.4)$$

for each frequency  $\omega_k$  for subsequent transformation back to the time domain. Here  $k_{R_k}$  represents the wave number for the fundamental mode at frequency  $\omega_k$ . Then

$$\begin{aligned} \hat{P}(\omega_k) &= \int_a^b \gamma_k \sum_{i=1}^N A_i(r') e^{-i\omega_k t_i} J_0(k_{R_k} r') r' dr', \\ &= \gamma_k \sum_{i=1}^N e^{i\omega_k t_i} \int_a^b A_i(r') J_0(k_{R_k} r') r' dr', \end{aligned} \quad (8.5)$$

where

$$\gamma_k = \frac{2 \sin \left( \frac{\Delta t \omega_k}{2} \right)}{\omega_k}.$$

Since  $A_i(r')$  is piecewise constant:

$$A_i(r') = A_{ij}, \quad a_j < r' \leq b_j,$$

this reduces to

$$P(\omega_k) = \gamma_k \sum_{i=1}^N e^{-i\omega_k t_i} \sum_{j=1}^M \frac{A_{ij}}{k_{R_k}} \left[ b_j J_1(k_{R_k} b_j) - a_j J_1(k_{R_k} a_j) \right]. \quad (8.6)$$

A similar procedure is followed for the  $\hat{Q}(\omega_k)$  except that quadratures are used to evaluate the integrals

$$\int_{a_j}^{b_j} J_1(k_{R_j} r') r' dr'.$$

Then with  $\hat{P}(\omega_k)$  and  $\hat{Q}(\omega_k)$  we can proceed to compute tele-seismic body or surface waves using the formulas (35) and (44) of Appendix E.

## 8.2 SURFACE WAVES FROM EJECTA

Surface wave seismograms were computed for the ejecta field for several cases. The seismograms are shown in Figure 8.1. The seismograms were computed at a range of 4000 km rather than the 3000 km range used for the records of Section VII. In order to see the effect of range on  $M_s$

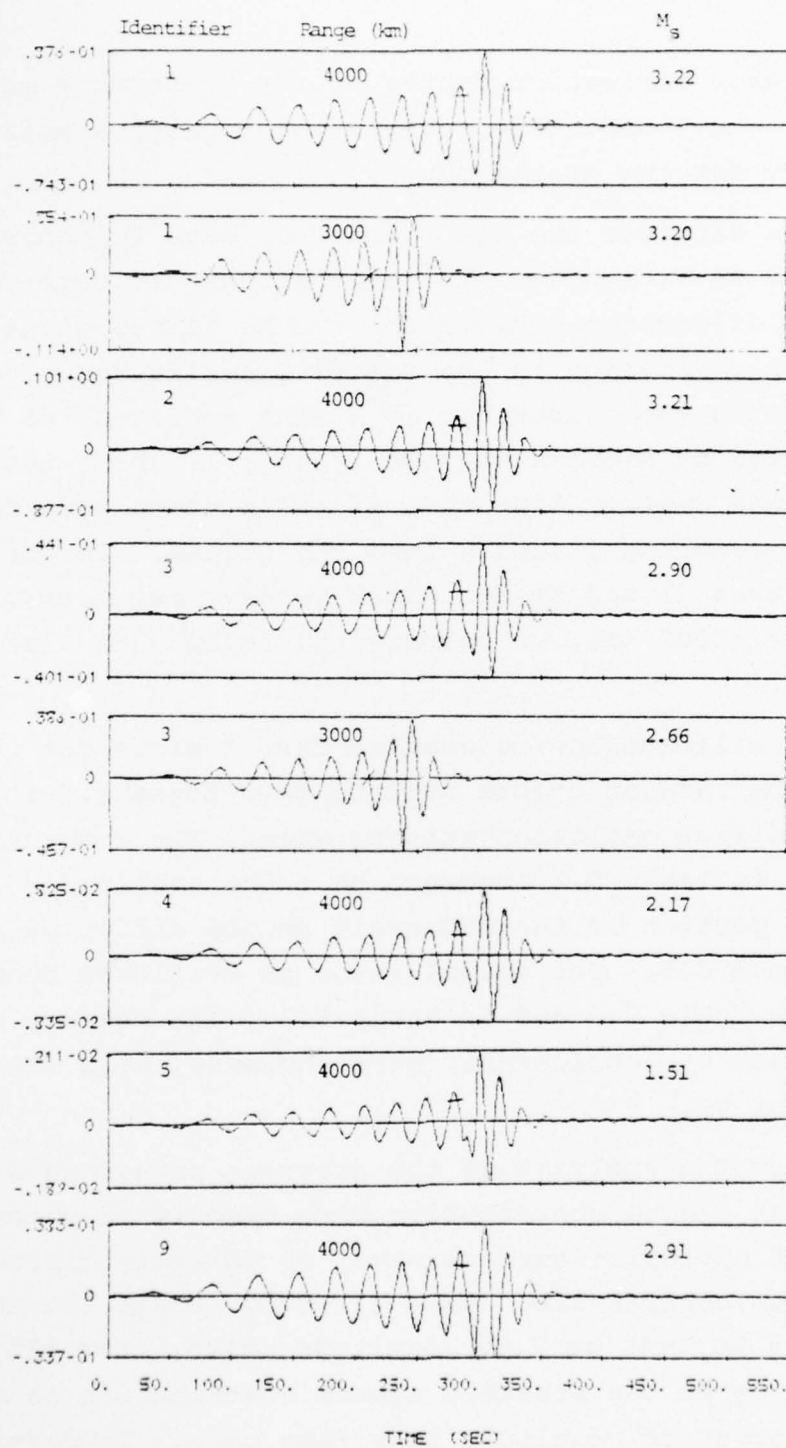


Figure 8.1. Vertical component Rayleigh wave seismograms due to the ejecta fallback from six cratering explosions. The numbers at the left are displacements in microns at 25 seconds.

(the distance correction factor in the  $M_s$  formula may differ from the actual amplitude decay), we computed a seismogram at 3000 km for two of the cases.

The data for the ejecta surface wave seismograms are summarized in Table 8.1. The explosion  $M_s$  is from Table 7.2. The difference between the two  $M_s$  values gives a reasonable approximation to the relative amplitudes. For example, when the difference is 2, the amplitude of the ejecta surface wave at periods near 20 seconds is about two orders of magnitude smaller than that of the surface wave from the explosion coupling directly into the ground. In fact, for the two cases (1 and 3) for which we have seismograms at the same range (3000 km), we compare the amplitudes directly in Table 8.2.

It will suffice to examine Case 1 since for this case we have the largest ejecta surface wave together with the smallest direct explosion surface wave. The comparison of  $M_s$  values in Table 8.1 suggests that the amplitudes of the 20 second portion of the wavetrain should differ by a factor of about 6.5. The actual ratio is available from the numbers in Table 8.2 and is about 6.8. The maximum amplitudes differ by considerably more, however, with the ratio being about 34.

From the analysis of the previous paragraph we see that if the ejecta contribution were exactly in phase with the direct explosion surface wave, an unlikely circumstance, the maximum contribution (Case 1) would change the amplitude by 15 percent or 0.06 magnitude units. For all the other cases the possible ejecta contribution is at least an order of magnitude less than this. Therefore, we feel justified in ignoring the ejecta contribution to the surface waves.

TABLE 8.1

## SURFACE WAVE DATA FROM EJECTA SEISMOGRAMS

<u>Identifier</u>	<u>Ejecta <math>M_s</math> Range (km)</u>	<u>Ejecta <math>M_s</math></u>	<u>Explosion <math>M_s</math></u>	<u>Difference</u>
Granite				
1	4000	3.22	4.01	0.79
1	3000	3.20	4.01	0.81
2	3000	3.21	4.95	1.74
3	4000	2.90	4.72	1.82
3	3000	2.66	4.72	2.06
Dry Sandstone				
4	4000	2.17	4.66	2.49
5	4000	1.51	4.68	3.17
Wet Sandstone				
9	4000	2.91	4.71	1.80

TABLE 8.2

## COMPARISON OF SURFACE WAVE AMPLITUDES AT 3000 km

(Amplitudes are in nm and are corrected for instrument response)

<u>Identifier</u>	<u><math>M_s</math> Amplitude</u>	<u><math>M_s</math> Period</u>	<u>Maximum Amplitude</u>	<u>Period of Maximum Cycle</u>
1 Explosion	425.0	20.0	5435.0	11.3
1 Ejecta	62.0	22.0	158.0	16.3
3 Explosion	2081.0	21.8	11,242.0	14.3
3 Ejecta	17.7	22.0	70.0	15.6



8.3 BODY WAVES FROM EJECTA

We saw in the previous paragraph that the ejecta is unlikely to have any noticeable effect on the surface waves or  $M_s$ . Since the source terms,  $\hat{P}(\omega)$  and  $\hat{Q}(\omega)$  of Appendix E, are the same for both cases, they would have to be strongly peaked (values at 1 Hz larger than at low frequencies) for there to be any chance of an effect on the short period body wave records. However, as is reasonably clear from (8.3) or (8.6), the source spectra have their largest values at low frequencies and decay rapidly with increasing frequency. The spectral values at the  $m_b$  frequencies are down by at least an order of magnitude from the values at  $M_s$  frequencies. Therefore, we can ignore the ejecta contribution to the short period recordings.

## IX. TELESEISMIC MAGNITUDES FOR 37.5 AND 600 kt

9.1 SOURCE SCALING

If we assume cube-root scaling is applicable, we can scale our results to obtain  $m_b$  and  $M_s$  for cratering explosions with yields different than the 150 kt at which the original calculations were made. The amplitudes of the curl and divergence of the displacement field are unchanged by the scaling, but the distance and time scales are multiplied by a factor  $(W_n/150)^{1/3}$ , where  $W_n$  is the new yield.

The basic representation of the source for computing teleseismic body and surface waves is in terms of the multipole coefficients,  $A_{\ell m}^{(\alpha)}(\omega)$ , in the frequency domain. It is easily shown that cube-root scaling implies that the scaled multipole coefficients for the new yield are related to the old coefficients by

$$A_{\ell m}^{(\alpha)}(\omega_n) = \left(\frac{W_n}{150}\right)^{1/3} A_{\ell m}^{(\alpha)}(\omega), \quad (9.1)$$

where

$$\omega_n = \left(\frac{150}{W_n}\right)^{1/3} \omega.$$

To compute seismograms for the scaled source we need to scale the multipole coefficients as indicated and then to follow through the procedures outlined in Sections VI and VII.

9.2 BODY WAVES FOR SCALED SOURCES

We compute seismograms for the sources of Table 3.1 at two new yields, 37.5 and 600 kt. The scale factor is then the cube-root of 4 and its reciprocal. The seismograms

BEST AVAILABLE COPY

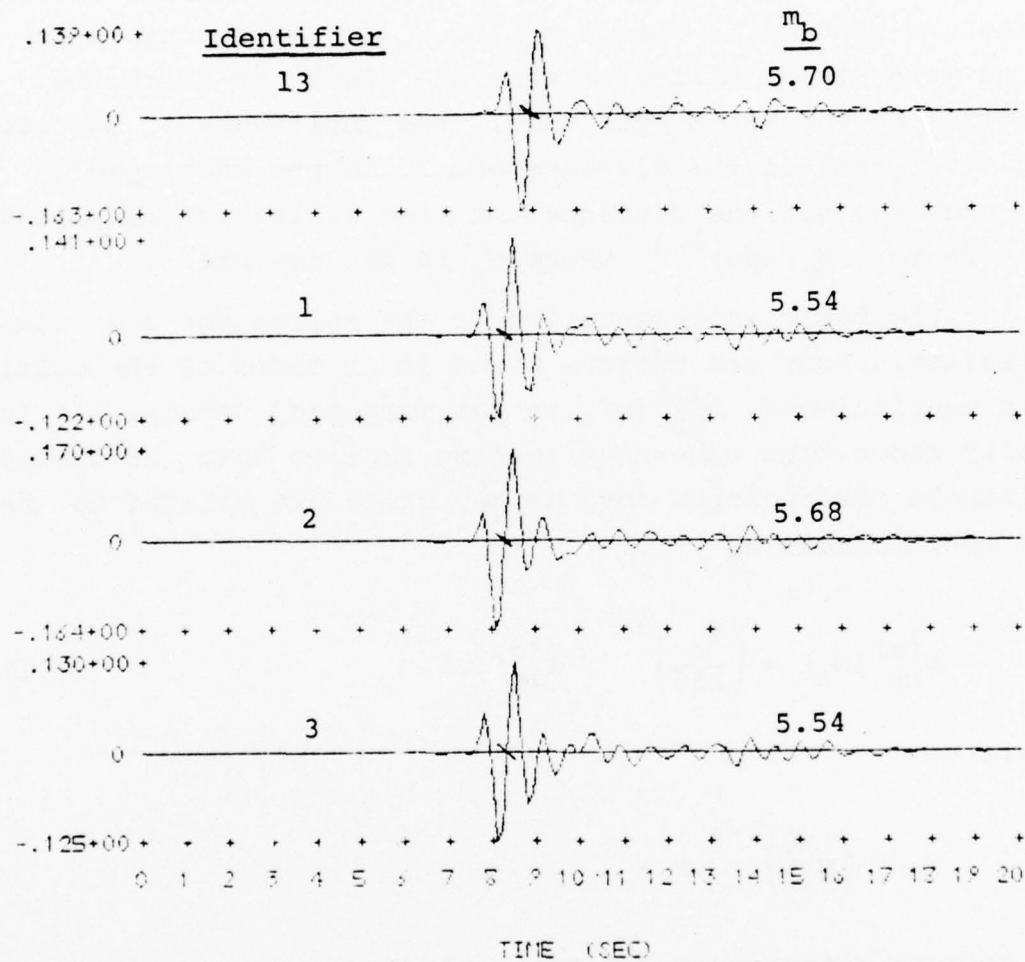


Figure 9.1. Synthetic short period seismograms for the granite sources scaled to 37.5 kt.

BEST AVAILABLE COPY

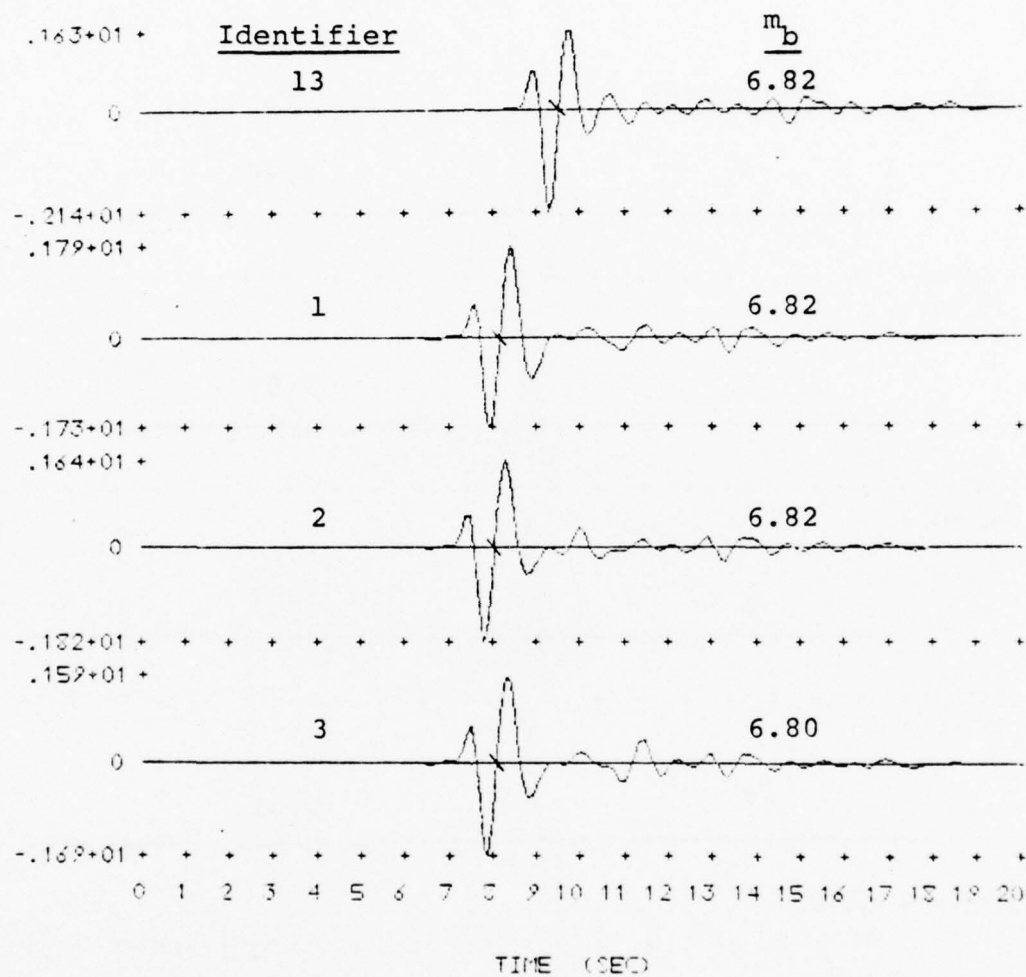


Figure 9.2. Synthetic short period seismograms for the granite sources scaled to 600 kt.

BEST AVAILABLE COPY

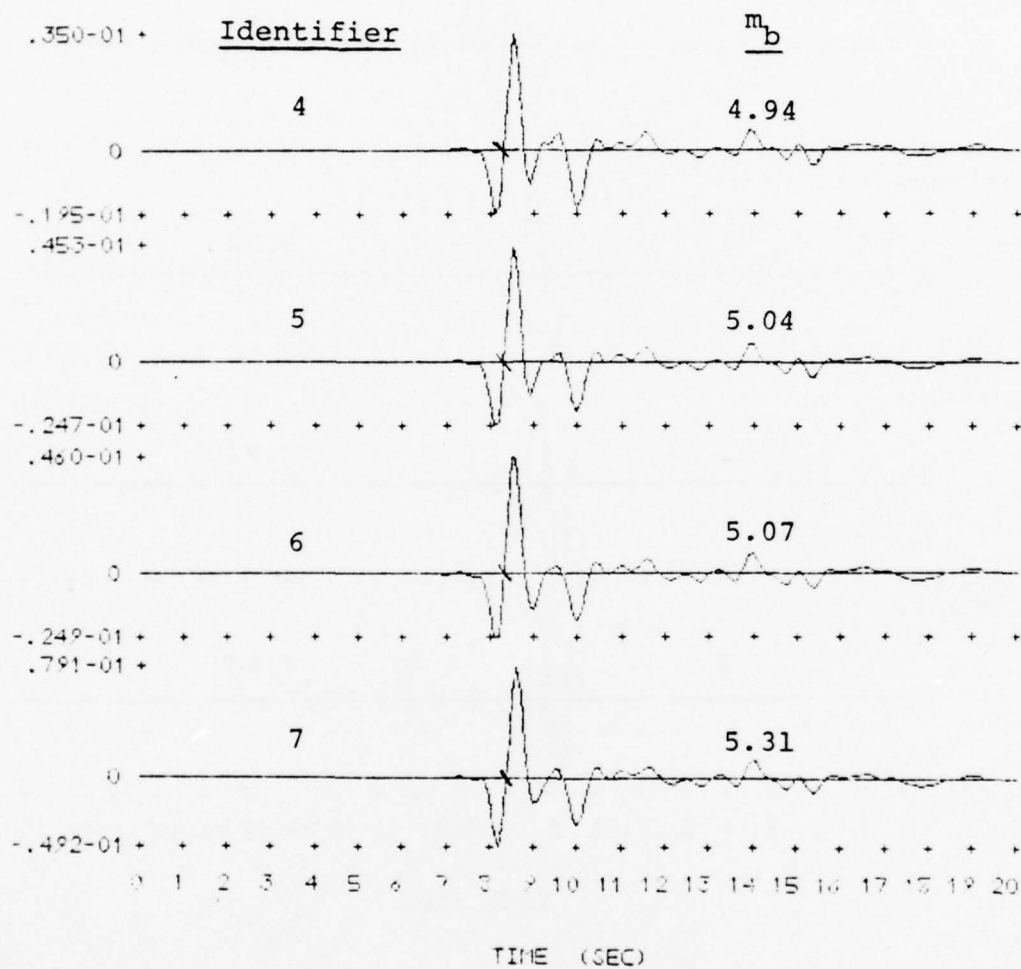


Figure 9.3. Synthetic short period seismograms for the dry sandstone sources scaled to 37.5 kt.



## BEST AVAILABLE COPY

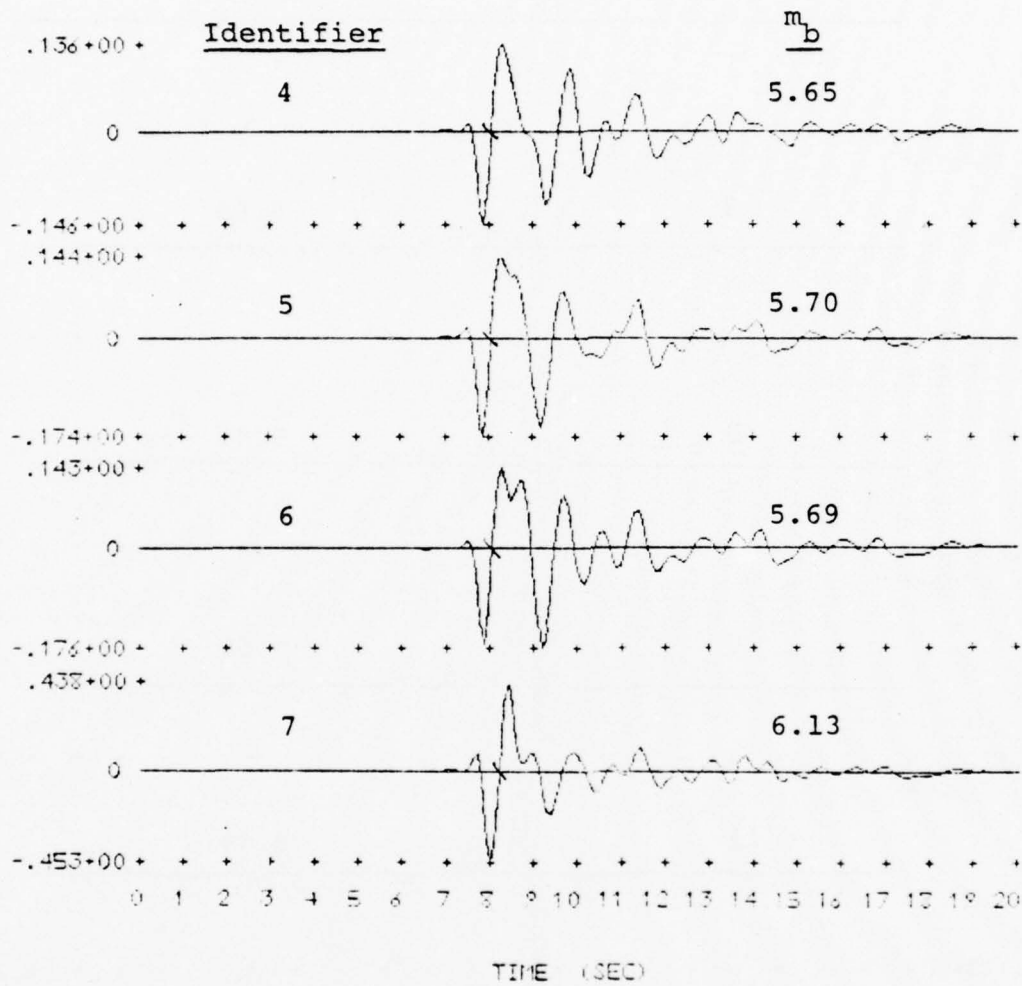


Figure 9.4. Synthetic short period seismograms for the dry sandstone sources scaled to 600 kt.

BEST AVAILABLE COPY

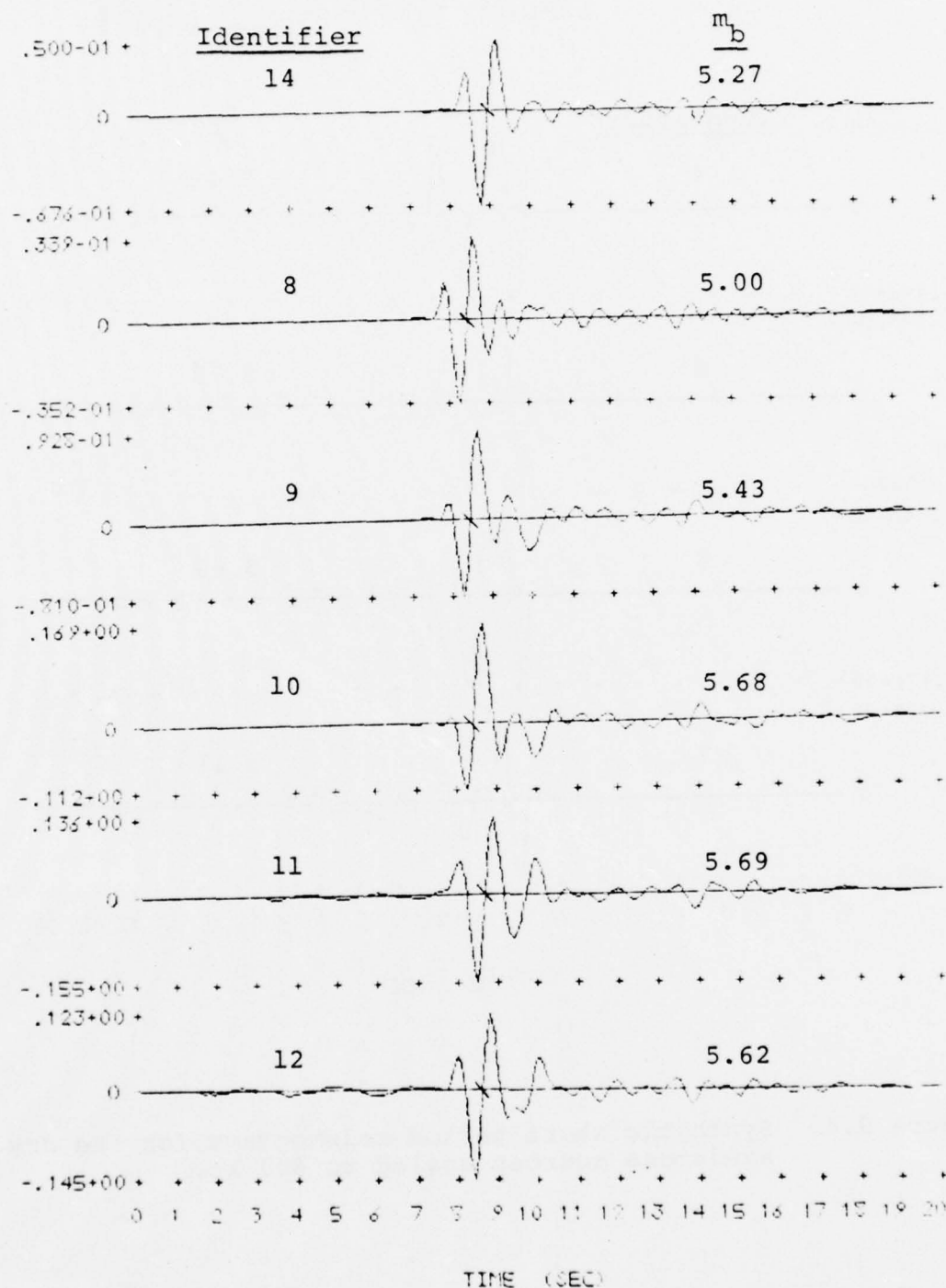


Figure 9.5. Synthetic short period seismograms for the wet sandstone sources scaled to 37.5 kt.

BEST AVAILABLE COPY

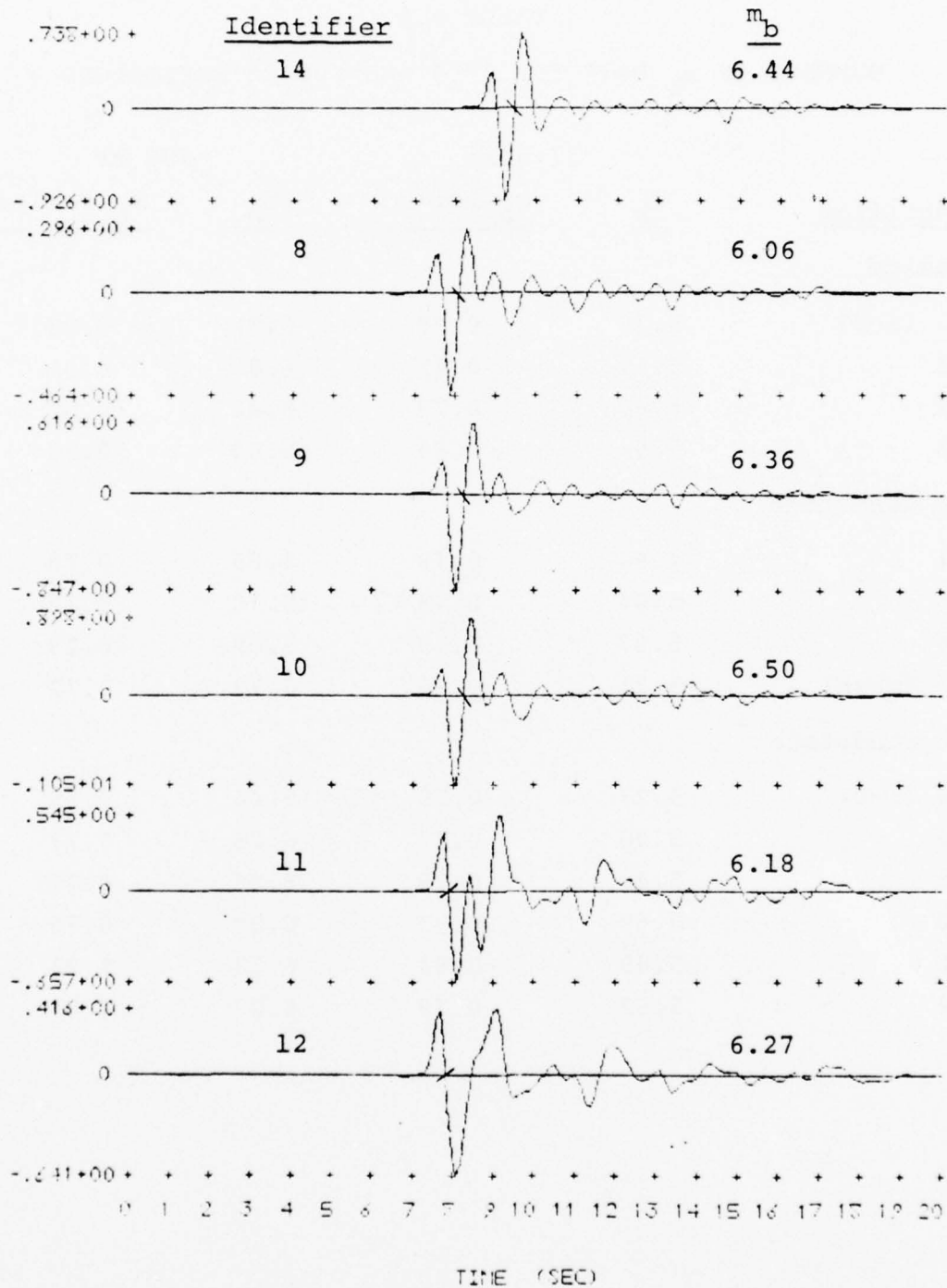


Figure 9.6. Synthetic short period seismograms for the wet sandstone sources scaled to 600 kt.

TABLE 9.1

SUMMARY OF  $m_b$  DATA FOR 37.5 AND 600 kt EXPLOSIONS

<u>Identifier</u>	37.5 kt		600 kt	
	<u><math>m_b</math></u>	<u><math>m_b</math> Period</u>	<u><math>m_b</math></u>	<u><math>m_b</math> Period</u>
Granite				
13 (1-D)	5.70	0.79	6.82	0.85
1	5.54	0.67	6.82	0.91
2	5.68	0.73	6.82	0.92
3	5.54	0.69	6.80	0.92
Dry Sandstone				
4	4.94	0.79	5.65	0.79
5	5.04	0.78	5.70	0.78
6	5.07	0.79	5.69	0.79
7 (weak)	5.31	0.80	6.13	0.77
Wet Sandstone				
14 (1-D)	5.27	0.79	6.44	0.80
8	5.00	0.72	6.06	0.77
9	5.43	0.79	6.36	0.77
10	5.68	0.83	6.50	0.78
11	5.69	0.84	6.18	0.71
12	5.62	0.79	6.27	0.87

TABLE 9.2  
COMPARISON OF  $m_b$  DATA FOR EVENTS OF VARYING YIELD

Identifier	$\frac{150}{m_b} - \frac{37.5}{m_b}$	Factor	$\frac{37.5}{T} \sqrt{\frac{150}{m_b}}$	$\frac{600}{m_b} - \frac{150}{m_b}$	Factor	$\frac{150}{T} \sqrt{\frac{600}{m_b}}$
Granite						
13 (1-D)	0.59	3.9	0.98	0.53	3.4	0.95
1	0.74	5.5	0.86	0.54	3.5	0.86
2	0.66	4.6	0.89	0.48	3.0	0.89
3	0.74	5.5	0.86	0.52	3.3	0.87
Dry Sandstone						
4	0.54	3.5	0.82	0.17	1.5	1.22
5	0.52	3.3	0.89	0.14	1.4	1.13
6	0.48	3.0	0.92	0.14	1.4	1.09
7 (weak)	0.49	3.1	0.86	0.33	2.1	1.21
Wet Sandstone						
14 (1-D)	0.61	4.1	1.0	0.56	3.6	0.99
8	0.66	4.6	0.77	0.40	2.5	1.22
9	0.55	3.6	0.86	0.38	2.4	1.19
10	0.43	2.7	0.90	0.39	2.5	1.18
11	0.41	2.6	0.82	0.08	1.2	1.45
12	0.53	3.4	0.80	0.12	1.3	1.14



are shown in Figures 9.1-9.6. The  $m_b$  data from these seismograms are summarized in Table 9.1. Once again, the phase at which the  $m_b$  is measured is indicated on the seismograms.

In Table 9.2 we compare the data for the three yields. We take the difference between the  $m_b$  for 150 kt and the  $m_b$  values for 37.5 and 600 kt. The column marked "Factor" is then the antilog of this difference. We also show the ratios of the periods of the  $m_b$  phases for the two yield pairings.

If the source spectra were flat throughout the band of interest, the "Factor" values in Table 9.2 would all be 4.0. The values that appear in the table indicate the complexity of the source. This is clearly illustrated by comparing the seismograms for the same cases in Figures 6.1-6.3 and Figures 9.1-9.6.

Comparing the 37.5 kt records to the 150 kt records, the behavior is more-or-less as expected. Sometimes the amplitude scales by more than a factor of 4, sometimes by less. The periods are shorter on the 37.5 kt records by a fairly uniform ratio throughout. For the 600 kt granite events, the results are also within the range of expected behavior.

The comparison of 600 kt and 150 kt records for the wet and dry sandstone gives some surprising results. The amplitude ratios are considerably less than four for all the cratering events. Further, the periods for the 600 kt  $m_b$  are actually shorter than for the 150 kt  $m_b$ . In fact, the periods for the 37.5 kt and 600 kt sandstone seismograms are about the same. The anomaly seems to be due to the interference pattern in the  $m_b$  portion of the wavetrain. A strong interfering phase is clearly visible on the 600 kt records for Cases 4, 5, 6, 11 and 12. Looking at the data of Table 9.2, these are the events for which the  $m_b$  is smallest compared to the expected values from scaling the 150 kt amplitudes by four.

The failure of the body wave amplitudes to scale exactly with yield is a function of the complexity of the source spectrum in the short period region. However, the long period or  $M_s$  portion of the spectrum is flat (Figures 5.1-5.6). Therefore, there is no reason to expect the  $M_s$  values to change by any value other than the log of the yield ratio or  $\pm 0.60$ .

## REFERENCES

- Bache, T. C., J. T. Cherry, D. G. Lambert, J. F. Masso and J. M. Savino [1976], "A Deterministic Methodology for Discriminating Between Earthquakes and Underground Nuclear Explosions," Systems, Science and Software Final Contract Report, ARPA, SSS-R-76-2925, July.
- Bache, T. C. and D. G. Harkrider [1976], "The Body Waves Due to a General Seismic Source in a Layered Earth Model: 1. Formulation of the Theory," BSSA, 66, pp. 1805-1819.
- Bache, T. C., J. T. Cherry, K. G. Hamilton, J. F. Masso and J. M. Savino [1975], "Applications of Advanced Methods for Identification and Detection of Nuclear Explosions from the Asian Continent," Systems, Science and Software Report SSS-R-75-2646, May.
- Cherry, J. T., T. C. Bache, C. B. Archambeau and D. G. Harkrider [1974], "A Deterministic Approach to the Prediction of Teleseismic Ground Motion from Nuclear Explosions," Systems, Science and Software Final Contract Report, DNA 3321F.
- Cherry, J. T., T. C. Bache and D. F. Patch [1975], "The Teleseismic Ground Motion Generated by a Nuclear Explosion in a Tunnel and Its Effect on the  $M_s/m_b$  Discriminant," Systems, Science and Software Final Contract Report, DNA 3645F.
- Cherry, J. T., T. C. Bache, W. O. Wray and J. F. Masso [1975a], "Teleseismic Coupling from the Simultaneous Detonation of an Array of Nuclear Explosions," Systems, Science and Software Report SSS-R-76-2865, February.
- Cherry, J. T., T. C. Bache and J. F. Masso [1976b], "A Three-Dimensional Finite Difference Simulation of Earthquake Faulting," to be submitted for publication.
- Ewing, W. M., F. Press and W. S. Jardetzky [1957], Elastic Waves in Layered Media, McGraw-Hill, New York.
- Fuchs, K. [1966], "The Transfer for P Waves for a System Consisting of a Point Source in a Layered Medium, BSSA, 56, pp. 75-108.
- Harkrider, D. G. [1964], "Surface Waves in Multilayered Media. I. Rayleigh and Love Waves from Sources in a Multilayered Half-Space," BSSA, 54, pp. 627-679.

- Harkrider, D. G. [1970], "Surface Waves in Multilayered Elastic Media. 2. Higher Mode Spectra and Spectral Ratios from Point Sources in Plane Layered Earth Models," BSSA, 60, pp. 1937-1987.
- Harkrider, D. G. and C. B. Archambeau [1977], "Theoretical Rayleigh and Love Waves from an Explosion in a Prestressed Source Region," to be submitted for publication.
- Hudson, J. A. [1969a], "A Quantitative Evaluation of Seismic Signals at Teleseismic Distances. I. Radiation from Point Sources," Geophys. J., 18, pp. 233-249.
- Hudson, J. A. [1969b], "A Quantitative Evaluation of Seismic Signals at Teleseismic Distances. II. Body and Surface Waves from an Extended Source," Geophys. J., 18, pp. 353-370.
- Marshall, P. D. and P. W. Basham [1972], "Discrimination Between Earthquakes and Underground Explosions Employing an Improved  $M_s$  Scale," Geophys. J., 28, pp. 431-458.
- McEvilly, T. V. [1964], "Central U.S. Crust-Upper Mantle Structure from Love and Rayleigh Wave Velocity Inversion," BSSA, 54, pp. 1997-2016.
- Morse, P. M. and H. Feshbach [1953], Methods of Theoretical Physics, McGraw-Hill, New York.
- Tryggvason, E. [1965], "Dissipation of Rayleigh Wave Energy," JGR, 70, pp. 1449-1455.
- Watson, G. N. [1966], A Treatise on the Theory of Bessel Functions, 2nd edition, Cambridge University Press.

# APPENDIX A

## EQUIVALENT ELASTIC SOURCE

The radiation field exterior to any kind of volume source in a homogeneous medium can be represented in terms of an expansion in spherical harmonics. Archambeau (1968) seems to have been the first to recognize the usefulness of this fundamental result and to apply it to geophysical problems. The expansion in spherical harmonics gives a compact equivalent elastic source representation of quite general character and nearly any proposed seismic source model can be cast in this form. A brief description of this source representation and its compatibility with commonly used source theories is the subject of this section.

The Fourier transformed equations of motion in a homogeneous, isotropic, linearly elastic medium may be written

$$\bar{\mathbf{u}} = - \left( \frac{1}{k_{\alpha}^2} \right) \nabla \bar{\chi}^{(4)} + \left( \frac{2}{k_{\beta}^2} \right) \nabla \times \bar{\chi} \quad , \quad (1)$$

where  $\bar{\mathbf{u}}$  is particle displacement and  $k_{\alpha}$  and  $k_{\beta}$  are the compressional and shear wave numbers. The Cartesian potentials  $\bar{\chi}^{(4)}$  and  $\bar{\chi}$  are defined by

$$\begin{aligned} \bar{\chi}^{(4)} &= \nabla \cdot \bar{\mathbf{u}} \quad , \\ \bar{\chi} &= \frac{1}{2} \nabla \times \bar{\mathbf{u}} \quad , \end{aligned} \quad (2)$$

and may be easily shown to satisfy the wave equation

$$\nabla^2 \bar{\chi}^{(j)} + k_1^2 \bar{\chi}^{(j)} = 0, \quad j = 1, 2, 3, 4, \quad (3)$$



where  $k_4 \equiv k_\alpha = \omega/\alpha$  and  $k_i \equiv k_\beta = \omega/\beta$  for  $i = 1, 2, 3$ . This equation has as a solution the following expansion in spherical eigenfunctions (e.g., Morse and Feshbach (1953)),

$$\bar{\chi}^{(j)}(\underline{R}, \omega) = \sum_{\ell=0}^{\infty} h_{\ell}^{(2)}(k_j R) \sum_{m=0}^{\ell} \left[ A_{\ell m}^{(j)}(\omega) \cos m\phi + B_{\ell m}^{(j)}(\omega) \sin m\phi \right] P_{\ell}^m(\cos\theta), \quad (4)$$

where the  $h_{\ell}^{(2)}$  are spherical Hankel functions of the second kind and the  $P_{\ell}^m$  are associated Legendre functions. The vector  $\underline{R}$  has as components the spherical coordinates  $R, \theta, \phi$ .

Equations (4), together with (1), provide an elastic point source representation of the (outgoing) displacement field. The values of the multipole coefficients,  $A_{\ell m}^{(j)}(\omega)$ ,  $B_{\ell m}^{(j)}(\omega)$ ,  $j = 1, 2, 3, 4$ , prescribe the displacement field at all points in the homogeneous medium where (1) applies. This point source representation can be viewed as a generalized form for a sum of a monopole or center of dilatation ( $\ell = 0$ ), a dipole or couple ( $\ell = 1$ ), a quadrupole or double-couple ( $\ell = 2$ ), etc. For example, a center of dilatation is represented by a single coefficient  $A_{00}^{(4)}$ , while for a horizontal double-couple the nonzero coefficients are  $-A_{21}^{(1)} = B_{21}^{(2)} = A_{22}^{(3)}$  and  $B_{22}^{(4)}$ .

Description of the character of the elastic field generated by seismic sources is, of course, a basic geophysical problem. For this paper it is convenient to discuss seismic source descriptions in three categories:

1. Those obtained using finite difference/finite element numerical methods.
2. Analytical source models of relaxation type.
3. Dislocation source models.

With numerical methods one can attempt to directly include complexities of the source mechanism in a deterministic computational scheme. For example, finite difference methods have been extensively used to compute the propagating shock wave due to an underground nuclear explosion (e.g., Cherry, et al., 1974). In this case the nonlinear behavior of the rock under high stress loading determines the character of the seismic signal. If the source region can be assumed to be embedded in a medium in which (1) applies, an equivalent elastic source of the form (4) can be obtained from the outgoing displacement field. This is indicated schematically in Figure 1. Briefly, the procedure is to monitor the outgoing displacement field or, alternatively, the potentials,  $\bar{\chi}^{(j)}$ , on a spherical surface of radius  $\hat{R}$ . Using the orthogonality of the spherical harmonics, these potentials are related to the multipole coefficients by

$$\begin{pmatrix} A_{\ell m}^{(j)}(\omega) \\ B_{\ell m}^{(j)}(\omega) \end{pmatrix} = \frac{C_{\ell m}}{h_{\ell}^{(2)}(k_j \hat{R})} \int_0^{2\pi} \int_0^{\pi} \bar{\chi}^{(j)}(\hat{R}, \omega) P_{\ell}^m(\cos \theta) \begin{pmatrix} \cos m\phi \\ \sin m\phi \end{pmatrix} \sin \theta d\theta d\phi, \quad (5)$$

where

$$C_{\ell m} = \frac{(2\ell+1)(\ell-m)!}{2\pi(\ell+m)!}, \quad m \neq 0,$$

$$C_{\ell 0} = (2\ell+1)/4\pi.$$

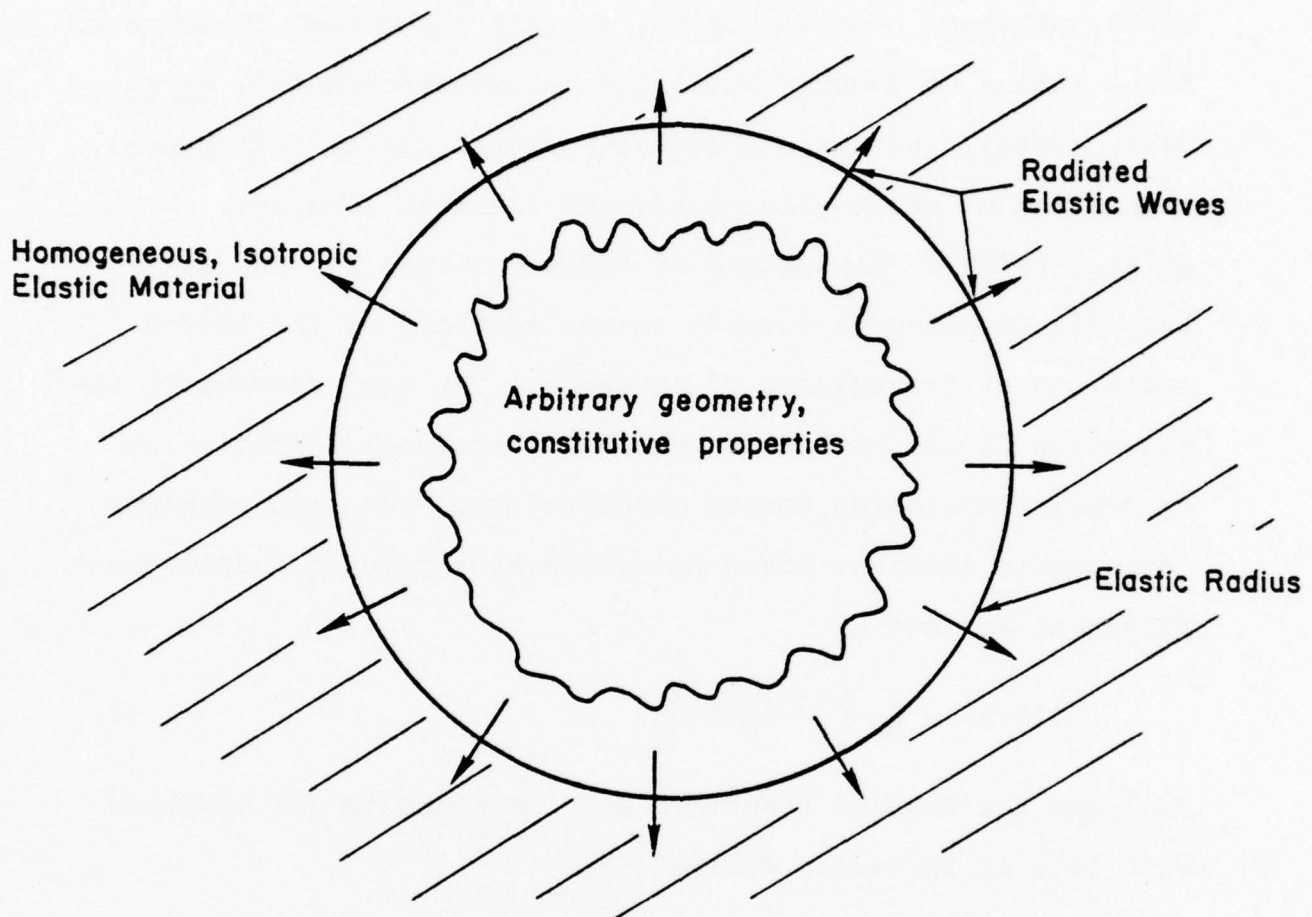


Figure 1. Schematic display of the determination of an equivalent elastic representation for an arbitrary volume source.

Use of this procedure for linking nonlinear finite difference source calculations with analytical wave propagation techniques was suggested to the first author by Archambeau (1973, personal communication), and has since been implemented for a number of complex explosion geometries (Cherry, et al., 1975, 1976a), and for a three-dimensional finite difference simulation of stick-slip earthquake faulting (Cherry, et al., 1976b). The number of terms required for the expansion (4) to converge depends on the symmetry of the source radiation at frequencies of interest. The most elementary application of the method is for one-dimensional (spherically symmetric) explosion source calculations. For such problems the elastic field is often described by a reduced displacement potential defined by

$$U(R,t) = \frac{\partial}{\partial R} \left[ \frac{\Psi(t-R/\alpha)}{R} \right]. \quad (6)$$

Applying the Fourier transform and comparing to (1) together with (4), it is easily derived that

$$A_{00}^{(4)}(\omega) = -i k_{\alpha}^3 \bar{\Psi}(\omega), \quad (7)$$

which shows the equivalence between the reduced displacement potential and the monopole. For more complex sources such as an explosion in an axisymmetric tunnel (Cherry, et al., 1975) or several explosions detonated simultaneously (Cherry, et al., 1976a) quadrupole and higher order terms occur in the expansion. When an earthquake source is computed, the

leading term is, as expected, the quadrupole (Cherry, et al., 1976b).



APPENDIX B  
APPLICATION OF THE MULTIPOLAR EXPANSION TECHNIQUE  
TO CRATERING EXPLOSIONS

In Appendix A is outlined the procedure for obtaining an equivalent elastic source representation of an arbitrary volume source. In particular, we evaluate the integrals (A.5) to obtain the multipolar coefficients  $(A_{\ell m}^{(1)}(\omega), B_{\ell m}^{(1)}(\omega))$  that define the equivalent elastic source. With these multipoles the displacement can be computed from (A.1) and (A.4) at any point in space.

The procedure outlined in Appendix A gives a unique and exact representation of the outgoing wave field when the following conditions are satisfied:

1. The spherical surface at the "elastic radius" is in a homogeneous, isotropic, linearly elastic medium.
2. No energy travels inward through this surface.
3. A sufficient number of terms are computed to insure convergence of the infinite series, Eq. (A.4) of Appendix A.

The ideal conditions listed above are certainly not satisfied in the problem of interest. The most obvious and important difficulty is the presence of a free surface. To understand the effect of the free surface, we should first describe the relevant features of how our technique works. First, the multipolar form can only represent waves that are solutions to the whole space wave equation; that is, body waves of compressional or shear type. Due to the presence of the free surface, there will be surface waves of the Rayleigh type in the numerical solution. These waves can never be properly represented in our multipolar solution. The solution will "see" the Rayleigh wave displacements

as some combination of P and S waves and will try to represent them in that form. In subsequent paragraphs we will explore the effect of the Rayleigh waves in more detail and argue that they do not seriously compromise our solution.

The second characteristic of our equivalent elastic source determination technique that needs to be understood is the way in which energy is partitioned into the various multipoles. It is the symmetry of the outgoing displacement field that controls this partitioning via the integral (A.5). We see from Eq. (A.5) that we operate on the divergence  $(\bar{\chi}^{(4)}(\hat{R}, \omega))$  and curl  $(\bar{\chi}^{(i)}(\hat{R}, \omega), i = 1, 2, 3)$  of the displacement field separately. As an illustrative example, let us assume that we have an axisymmetric source in a homogeneous whole space and examine how the propagating divergence is partitioned into the multipole coefficients  $A_{\ell m}^{(4)}(\omega), B_{\ell m}^{(4)}(\omega)$ . Since the  $\bar{\chi}^{(4)}$  is independent of  $\phi$ , the only non-zero multipoles are  $A_{\ell 0}^{(4)}(\omega)$ . Then, from (A.4), the divergence is written as follows:

$$\bar{\chi}^{(4)}(\underline{R}, \omega) = \sum_{\ell=0}^{\infty} h_{\ell}^{(2)}(k_{\alpha} R) A_{\ell 0}^{(4)}(\omega) P_{\ell}^0(\cos \theta) \quad (B.1)$$

That is, each frequency component of the source generated displacement field is made up of a sum of terms with symmetry specified by the Legendre polynomials. The radiation pattern for the first several terms is shown in Figure B.1. Then, for example, if the divergence,  $\chi^{(4)}$ , of the displacement field exhibits considerable spherical symmetry, the solution will be dominated by the first term in B.1 and the higher order terms will represent the deviation from this symmetry. The same kind of process operates for the curl and the arguments are easily extended to a more general (not axisymmetric) source.

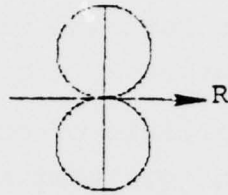
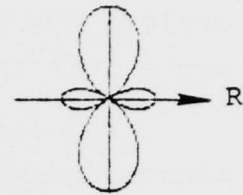
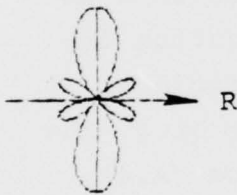
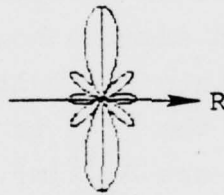
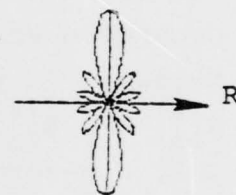

 $P_0^0$  (monopole)

 $P_1^0$  (dipole)

 $P_2^0$  (quadrupole)

 $P_3^0$ 

 $P_4^0$ 

 $P_5^0$ 

Figure B.1. The radiation patterns for the first several terms of the expansion of the divergence for an axisymmetric source. The  $P_\ell^0$  is the radiation pattern for the  $A_\ell^{(4)}(\omega)$  coefficient (see Eq. B.1).

We have pointed out that the symmetry of the source determines the partitioning of energy into the various terms of the series. But for the cratering calculations the displacement field is computed on only one hemisphere. It is necessary to assume values on the other hemisphere to compute the multipole coefficients. The way this assumption is made can have a substantial influence on the solution.

Let us now look more closely at the problem of immediate interest as we describe our modification of the multipolar expansion technique for this application. In Figure B.2 the geometry and coordinate system for a typical calculation is shown. The explosion is at a depth,  $h$ , in a homogeneous halfspace. The radius,  $R_e$ , on which the curl and divergence of the displacement field is monitored varies from  $2.3 h$  to  $24.5 h$  for the twelve calculations to be studied, though it is between  $5 h$  and  $10 h$  for most of them.

Now, how are we to select values for the curl and divergence in the upper hemisphere ( $\theta \in (0, \pi)$ ) in order to make the data compatible with our multipolar representation? The simplest and most natural choice is to make the data in the upper hemisphere depend on that in the lower hemisphere in some simple fashion.

In Appendix C we discuss the mathematical consequence of certain kinds of source symmetry. There are two cases of particular interest; that of axisymmetry plus vertical symmetry which is characterized by

$$\chi^{(4)}(\pi - \theta) = \chi^{(4)}(\theta),$$

$$\chi^{(1)}(\pi - \theta) = -\chi^{(1)}(\theta),$$

$$\chi^{(2)}(\pi - \theta) = -\chi^{(2)}(\theta),$$

and is discussed in Section C.2.2 and that of axisymmetry and vertical antisymmetry:

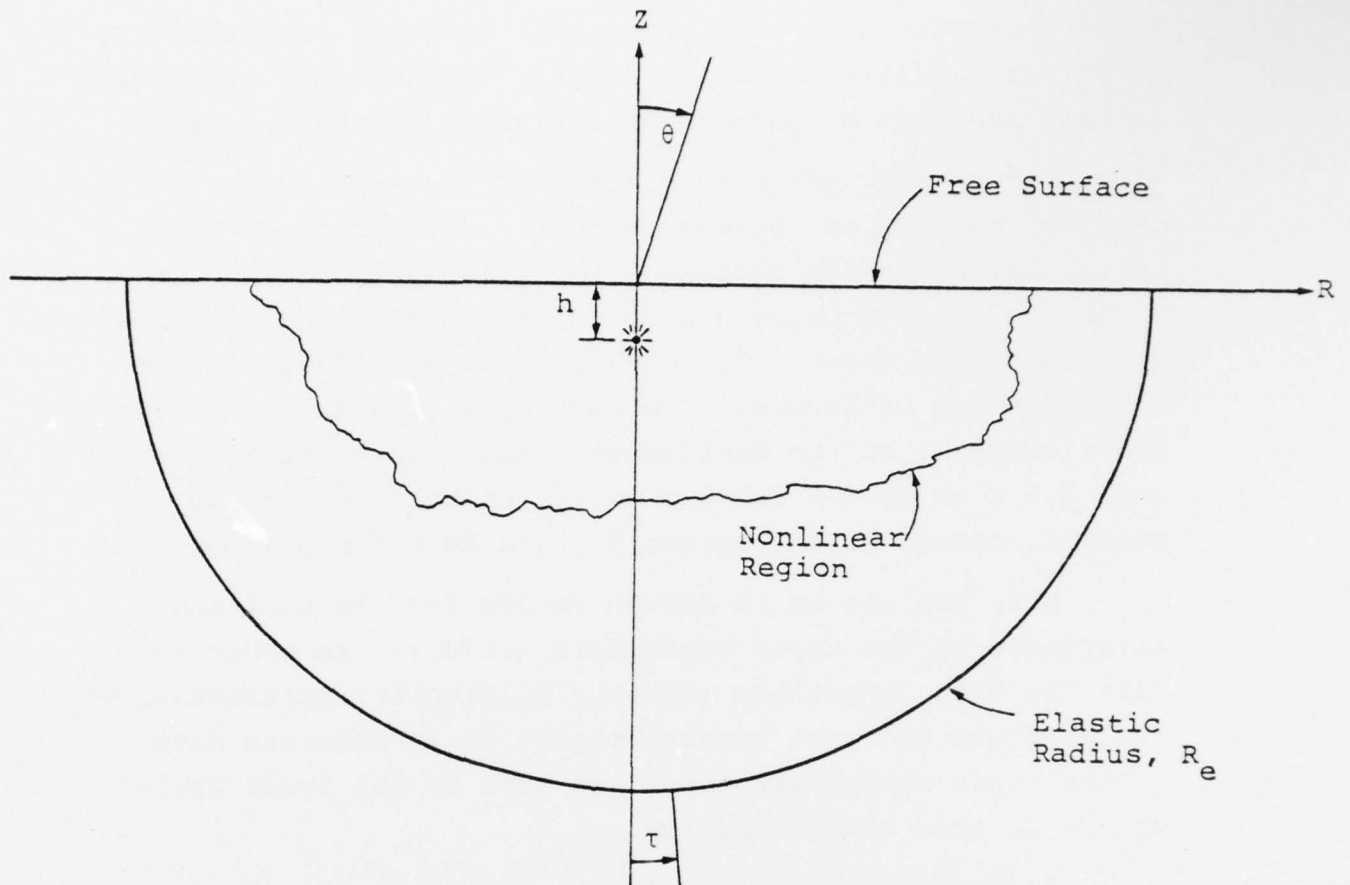


Figure B.2. The geometry and coordinate system for the cratering calculations. The solution is independent of the azimuthal coordinate.



$$\chi^{(4)}(\pi-\theta) = -\chi^{(4)}(\theta),$$

$$\chi^{(1)}(\pi-\theta) = \chi^{(1)}(\theta),$$

$$\chi^{(3)}(\pi-\theta) = \chi^{(2)}(\theta),$$

discussed in Section C.2.3. The non-zero multipole coefficients for these two cases are listed in Table C.3. In Figure B.1 we showed the radiation patterns for each term in the multipolar expansion of the divergence or P wave portion of the displacement field. If we assume vertical symmetry the even order terms (monopole, quadrupole, etc.) will be non-zero. If, on the other hand, vertical anti-symmetry is assumed, the odd order terms are non-zero.

The radiation patterns for the lower order terms are important because these terms dominate the response at long periods. In fact, we can be certain that the very first term, monopole or dipole depending on the symmetry chosen, will be the only term that matters for computing far-field surface waves and  $M_s$ . Therefore, let us look at the radiation patterns for the S wave coefficients. From Table C.3 and Eq. (A.4) we see that the radiation patterns are given by the Legendre functions  $P_\ell^1(\cos\theta)$  with  $\ell$  even for vertical symmetry and  $\ell$  odd for vertical anti-symmetry. These patterns are plotted in Figure B.3.

How are we to choose the most appropriate vertical symmetry? The first suggestion that comes to mind is to examine the angular variation of the computed data at various time points. Typical radiation pattern plots of the data are shown in Appendix D where we describe several calculations in considerable detail. We see that these radiation pattern plots are not much help. There are at least four reasons why this is so:

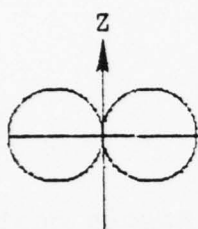
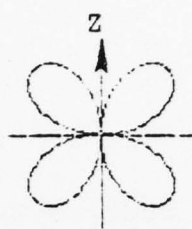
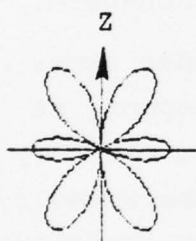
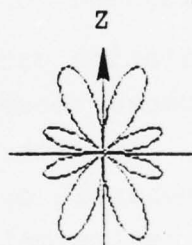

 $P_1^1$  (dipole)

 $P_2^1$  (quadrupole)

 $P_3^1$ 

 $P_4^1$ 

Figure B.3. The radiation patterns for the first several terms of the curl for an axisymmetric source.

1. The calculated divergence and curl include the influence of Rayleigh waves at late times. We want to choose a symmetry that minimizes the effect of this contribution.
2. The numerical calculations are noisy. Our multipolar source representation should act as a smoothing filter that pulls the important signal from this noisy data.
3. The calculations are really not yet complete; that is, energy is still propagating through the elastic radius at the last time point. We are mainly interested in imposing the right symmetry at long times as the high frequency solution is much less dependent on this choice.
4. Our real interest is in the radiation patterns for the far-field component of the source (that portion decaying as  $R^{-1}$ ). The patterns for the computed data are strongly influenced by near-field terms.

We can attempt to gain some insight with analytical methods. Among the class of simple problems, perhaps the closest to the creating calculations, at least at long times, is the case of a vertical point force on the surface of a homogeneous halfspace. The far-field radiation patterns for the divergence and curl are shown for this source in Figure B.4. We see that the P wave pattern is very much like that of a dipole (see Figure B.1). This suggests that vertical antisymmetry should work very well for the P wave portion of the radiation field. For the S waves vertical symmetry would probably be a better choice since the curl radiation pattern in Figure B.4 looks more like a quadrupole. But from Appendix C, especially Tables C.1 and C.2, we see that choice of different symmetries for the curl and divergence leads to inconsistencies in the displacement field.

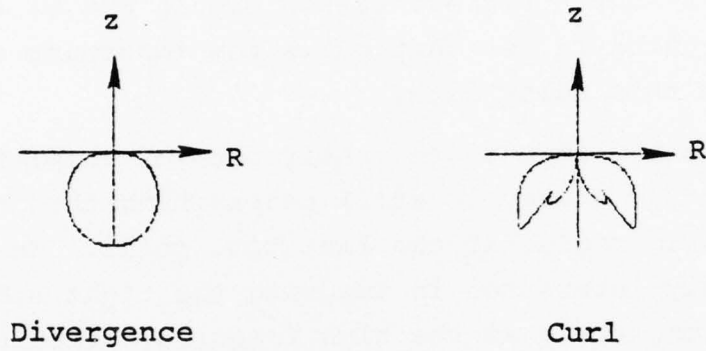


Figure B.4. Far-field radiation patterns for the divergence and curl due to a point's load on the surface of a homogeneous halfspace.

Therefore, we choose vertical antisymmetry and represent the field as a sum of terms of order 1, 3, 5, ....

It turns out that we need not be overly concerned with the accuracy of our S wave representation anyway. This is because the S waves must be many times larger than the P waves, a most unlikely circumstance, to have an appreciable effect on either  $m_b$  or  $M_s$ . This point is addressed in the main body of the report, Sections VI and VII.

What about the contribution of locally generated Rayleigh waves to our solution? First, we point out that the displacements due to the Rayleigh waves will only affect the solution in the region near the free surface. Referring to Figure B.2, we don't expect the Rayleigh waves to be of importance for takeoff angles,  $\tau$ , less than say,  $60^\circ$ . Second, the Rayleigh wave has a much greater effect on the S wave or curl portion of the field than on the P wave portion. These points were validated by an elastic test problem where we applied our procedures to the field from a point source on the surface of a homogeneous halfspace. Once again, we expect the errors to be greatest in the S wave terms and at long periods. Fortunately, the P wave terms are dominant for  $m_b$  and  $M_s$  determinations.



## APPENDIX C

## PROPERTIES OF AN AXIALLY SYMMETRIC SEISMIC SOURCE

C.1 SYMMETRY PROPERTIES OF THE DISPLACEMENT AND POTENTIAL FIELDS FROM AN AXIALLY SYMMETRIC SOURCE

In studies of the ground motion from many sources the calculation is greatly simplified if the seismic source possesses the axial symmetry. Teleseismic ground motion from many complicated seismic sources can then be computed by merging a 2D nonlinear finite difference source calculation with the elastic wave propagation methods of theoretical seismology. This has been accomplished routinely at  $S^3$  by means of an equivalent elastic source representation of the seismic source. The theoretical foundation for this representation appears in a section of a recent paper by Bache and Harkrider [1976]. This section is reproduced as Appendix A of this report.

Many sources not only possess axial symmetry but also exhibit an additional physical symmetry with respect to the plane normal to the axis of symmetry. We will refer to two special cases of this symmetry, that of vertical symmetry and that of vertical antisymmetry. Then for axially symmetric sources, three types of symmetry will be discussed:

1. Axial symmetry.
2. Axial symmetry and reflection symmetry.
3. Axial symmetry and reflection antisymmetry.

A seismic source exhibits axial symmetry if the source is invariant under rotation about a given axis, say the z-axis. As a consequence of this symmetry, the particle displacement field must be invariant with respect to

rotations about the z-axis and consequently have no azimuth component. Since the field is independent of the azimuthal coordinate,  $\phi$ , the problem can be reduced to two dimensions. This results in a substantial reduction in the computational effort. In general, for an axially symmetric source the 2D finite difference calculation can be limited to an area enclosed by a semi-circle ( $0^\circ \leq \theta \leq 180^\circ$ ). In the special case where the source exhibits either vertical symmetry or antisymmetry, the 2D source calculation can be further limited to a single quadrant ( $0^\circ \leq \theta \leq 90^\circ$ ). The calculation of the multipole coefficients representing the equivalent elastic source requires a double integration in the spherical coordinates  $\phi$  and  $\theta$  over a spherical surface in the elastic region that completely surrounds the nonlinear zone containing the seismic source. For an axially symmetric source, however, this surface integration can be reduced to a single integral along a circular arc in the elastic region. This linkage between the 2D finite difference source calculation and the elastic wave propagation methods of theoretical seismology is accomplished by the MULTEES series of computer programs which calculate the multipole coefficients for the equivalent elastic source. The 2D source calculation must be carried out into the elastic region where time histories can be saved for the displacement potentials, which are defined below in terms of the divergence and curl of the displacement field. These time histories are generated at a set of monitoring stations that are either (1) on the arc of fixed radius in the elastic region for a 2D calculation in polar coordinates  $(r, \theta)$ ; or (2) in the neighborhood of an arc in the elastic region for a 2D calculation in rectangular coordinates  $(Z, Y)$ . MULTEES performs all of the operations required to transform the 2D variables for the calculation of the multipole coefficients, in the latter case including a 2D spatial interpolation to evaluate saved variables on a circular arc. The MULTEES programs are

described in Bache, et al. [1975]. A typical 2D section of an axially symmetric source at fixed azimuthal angle  $\phi$  is illustrated in Figure C.1. The Z-axis is the axis of symmetry and the X-Y plane is a possible plane of symmetry. The relationship between Cartesian (1,2,3), spherical (R, $\theta$ , $\phi$ ) and 2D finite difference code (Y,Z) coordinate system is also illustrated.

The symmetry properties of the particle displacement field will be used to derive the symmetry properties of the scalar (dilatational) displacement potential and the vector (rotational) displacement potential. The vector and scalar potentials are defined in terms of the displacement field  $\underline{u}(\underline{r},t)$  by,

$$\begin{aligned}\underline{\chi} &= \frac{1}{2} \nabla \times \underline{u} , \\ \chi^{(4)} &= \nabla \cdot \underline{u} .\end{aligned}\tag{C.1}$$

The symmetry properties of the displacement potentials will then be applied to derive the nonzero multipole coefficients for the equivalent elastic source representation of axially symmetric sources in each of the three classes defined above.

For an axially symmetric source the displacement field is invariant to rotations about the Z-axis and has no azimuthal component. As a consequence, the dilatational potential  $\chi^{(4)}$  must be independent of  $\phi$  and the rotational potential  $\underline{\chi}$  must have only a single non-vanishing component in spherical coordinates,  $\chi_\phi$ , which is also independent of  $\phi$ . For an axially symmetric source the non-vanishing displacement and potential components in spherical coordinates are

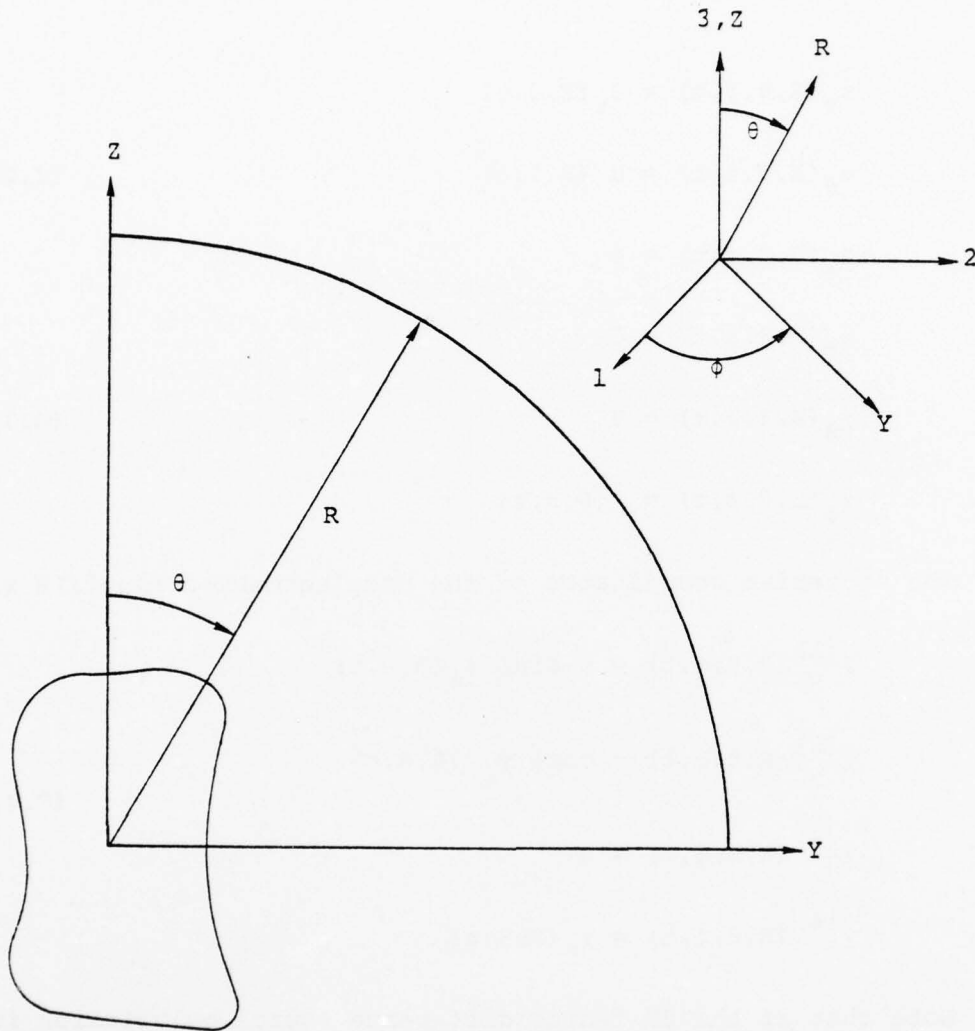


Figure C.1. Coordinate system for an axially symmetric source at fixed azimuthal angle. The inset illustrates the relation between the Cartesian (1,2,3), spherical ( $R, \theta, \phi$ ) and 2D finite difference code (Y,Z) coordinate systems.

$$\begin{aligned}
 u_r(R, \theta, \phi, t) &= u_r(R, \theta, t) \\
 u_\theta(R, \theta, \phi, t) &= u_\theta(R, \theta, t)
 \end{aligned}
 \tag{C.2}$$

$$\begin{aligned}
 u_\phi(R, \theta, \phi, t) &= 0 \\
 \chi_r(R, \theta, \phi, t) &= 0 \\
 \chi_\theta(R, \theta, \phi, t) &= 0 \\
 \chi_\phi(r, \theta, \phi, t) &= \chi_\phi(R, \theta, t)
 \end{aligned}
 \tag{C.3}$$

The Cartesian coordinates of the displacement potentials are

$$\begin{aligned}
 \chi^{(1)}(R, \theta, \phi, t) &= -\sin\phi \chi_\phi(R, \theta, t) \\
 \chi^{(2)}(R, \theta, \phi, t) &= \cos\phi \chi_\phi(R, \theta, t) \\
 \chi^{(3)}(R, \theta, \phi, t) &= 0 \\
 \chi^{(4)}(R, \theta, \phi, t) &= \chi_4(R, \theta, t)
 \end{aligned}
 \tag{C.4}$$

Note that if the 2D finite difference source calculation is carried out in the YZ plane, then one can identify the azimuthal component  $\chi_\phi$  as,

$$\chi_\phi(0, Y, Z, t) = -\frac{1}{2} [\text{curl } \underline{u}] = -\frac{1}{2} \left( \frac{\partial w}{\partial Y} - \frac{\partial v}{\partial Z} \right).$$

Because of the reduction in the number of non-vanishing spherical components of  $\underline{u}$  and  $\underline{\chi}$ , the symmetry properties that are characteristic of an axially symmetric source can be first expressed for the spherical components and then derived for Cartesian coordinates by means of the coordinate transformation for any vector  $\underline{A}$ ,



$$\begin{aligned}
A_1 &= \sin\theta \cos\phi A_r + \cos\theta \cos\phi A_\theta - \sin\phi A_\phi \\
A_2 &= \sin\theta \sin\phi A_r + \cos\theta \sin\phi A_\theta + \cos\phi A_\phi \\
A_3 &= \cos\theta A_r - \sin\theta A_\theta.
\end{aligned} \tag{C.5}$$

The symmetry properties of an axially symmetric source are given for the particle displacement field in Table C.1. The symbols  $u$ ,  $v$ , and  $w$  represent the  $X$ ,  $Y$  and  $Z$  components of the displacement field  $\underline{u}$ . Values for these components in the second, third and fourth octants are related to their corresponding value in the first octant. If either case of vertical symmetry obtains, an additional relation exists for points below the  $Z = 0$  plane (fifth octant). Consequently, displacement, velocity and potential components at all points on the surface of a sphere in the elastic region can be derived from the time histories saved on the circular arc  $0^\circ \leq \theta \leq 180^\circ$  for axial symmetry or on the arc  $0^\circ \leq \theta \leq 90^\circ$  for axial plus vertical (anti) symmetry.

The symmetry properties of the dilatational and rotational displacement potential can be derived from those for the displacement field. The results of this derivation are given in Table C.2. One example illustrates the method employed. From the definition of the rotational potential, Eq. (C.1) and the symmetry properties for vertical symmetry,

$$\begin{aligned}
\chi^{(1)} &= \frac{1}{2} [\text{curl } \underline{u}] = \frac{1}{2} \left( \frac{\partial w}{\partial y} - \frac{\partial v}{\partial z} \right) \\
\chi^{(1)}(x, y, -z) &= \frac{1}{2} \left( \frac{\partial (-w)}{\partial y} - \frac{\partial v}{\partial (-z)} \right) = -\chi^{(1)}(x, y, z)
\end{aligned} \tag{C.6}$$

As a consequence of the symmetry properties, the following boundary conditions will apply:

TABLE C.1

SYMMETRY PROPERTIES OF THE DISPLACEMENT FIELD FOR AN AXIALLY  
SYMMETRIC SOURCE

Field components in the 2nd, 3rd, 4th and 5th octants (column 2) are related to their values in the 1st octant (columns 3-5).

( $u, v, w$  = X, Y and Z components of particle displacement).

<u>Octant</u>	<u>Field Component</u>	<u>Axial Symmetry Only</u>	<u>Vertical Symmetry</u>	<u>Vertical Antisymmetry</u>
5	$u_r(r, \pi - \theta)$	*	$+u_r(r, \theta)$	$-u_r(r, \theta)$
	$u_\theta(r, \pi - \theta)$	*	$-u_\theta(r, \theta)$	$+u_\theta(r, \theta)$
5	$u(x, y, -z)$	*	$+u(x, y, z)$	$-u(x, y, z)$
	$v(x, y, -z)$	*	$+v(x, y, z)$	$-v(x, y, z)$
	$w(x, y, -z)$	*	$-w( \quad )$	$+w( \quad )$
2	$u(-x, y, z)$	$-u(x, y, z)$	$-u(x, y, z)$	$-u( \quad )$
	$v(-x, y, z)$	$+v( \quad )$	$+v( \quad )$	$+v( \quad )$
	$w(-x, y, z)$	$+w( \quad )$	$+w( \quad )$	$+w( \quad )$
3	$u(-x, -y, z)$	$-u( \quad )$	$-u( \quad )$	$-u( \quad )$
	$v(-x, -y, z)$	$-v( \quad )$	$-v( \quad )$	$-v( \quad )$
	$w(-x, -y, z)$	$+w( \quad )$	$+w( \quad )$	$+w( \quad )$
4	$u(x, -y, z)$	$+u( \quad )$	$+u( \quad )$	$+u( \quad )$
	$v(x, -y, z)$	$-v( \quad )$	$-v( \quad )$	$-v( \quad )$
	$w(x, -y, z)$	$+w( \quad )$	$+w( \quad )$	$+w( \quad )$

\* Relationship undefined

TABLE C.2

SYMMETRY PROPERTIES OF THE DISPLACEMENT POTENTIALS FOR AN  
AXIALLY SYMMETRIC SOURCE

Field components in the 2nd, 3rd, 4th and 5th octants (column 2) are related to their values in the 1st octant (columns 3-5).

( $\chi^{(1)}$ ,  $\chi^{(2)}$ ,  $\chi^{(3)}$  = X, Y and Z components of rotation displacement potentials).

Octant	Field Component	Axial Symmetry Only	Vertical Symmetry	Vertical Antisymmetry
5	$\chi_\phi(r, \pi - \theta)$	*	$-\chi_\phi(r, \theta)$	$+\chi_\phi(r, \theta)$
5	$\chi^{(1)}(x, y, -z)$	*	$-\chi^{(1)}(x, y, z)$	$+\chi^{(1)}(x, y, z)$
	$\chi^{(2)}(x, y, -z)$	*	$-\chi^{(2)}( )$	$+\chi^{(2)}( )$
	$\chi^{(4)}( )$	*	$+\chi^{(4)}(x, y, z)$	$-\chi^{(4)}( )$
2	$\chi^{(1)}(-x, y, z)$	$+\chi^{(1)}(x, y, z)$	$+\chi^{(1)}(x, y, z)$	$+\chi^{(1)}(x, y, z)$
	$\chi^{(2)}(-x, y, z)$	$-\chi^{(2)}( )$	$+\chi^{(2)}( )$	$+\chi^{(2)}( )$
	$\chi^{(4)}( )$	$+\chi^{(4)}( )$	$+\chi^{(4)}( )$	$+\chi^{(4)}( )$
3	$\chi^{(1)}(-x, -y, z)$	$-\chi^{(1)}( )$	$-\chi^{(1)}( )$	$-\chi^{(1)}( )$
	$\chi^{(2)}(-x, -y, z)$	$-\chi^{(2)}( )$	$-\chi^{(2)}( )$	$-\chi^{(2)}( )$
	$\chi^{(4)}( )$	$+\chi^{(4)}( )$	$+\chi^{(4)}( )$	$+\chi^{(4)}( )$
4	$\chi^{(1)}(x, -y, z)$	$-\chi^{(1)}( )$	$-\chi^{(1)}( )$	$-\chi^{(1)}( )$
	$\chi^{(2)}(x, -y, z)$	$+\chi^{(2)}( )$	$+\chi^{(2)}( )$	$+\chi^{(2)}( )$
	$\chi^{(4)}( )$	$+\chi^{(4)}( )$	$+\chi^{(4)}( )$	$+\chi^{(4)}( )$

\* Relationship undefined

1. Axial Symmetry Only

On the Z-axis corresponding to  $x = y = 0$  or  
 $\theta = 0$ ,  $\chi = 0$  or

$$\chi^{(1)}(R, 0, t) = 0,$$

$$\chi^{(2)}(R, 0, t) = 0. \quad (C.7)$$

2. Axial Plus Vertical Symmetry

On the XY plane (the plane of symmetry) corresponding to  $z = 0$  or  $\theta = 90^\circ$ ,  $\chi = 0$ , or

$$\chi^{(1)}(R, \pi/2, t) = 0,$$

$$\chi^{(2)}(R, \pi/2, t) = 0. \quad (C.8)$$

3. Axial Plus Vertical Antisymmetry

On the XY plane corresponding to  $z = 0$ , or  
 $\theta = 90^\circ$ ,

$$\chi^{(4)}(R, \pi/2, t) = 0. \quad (C.9)$$

C.2 MULTIPOLE COEFFICIENTS FOR AN AXIALLY SYMMETRIC SOURCE

The equivalent elastic source representation for any arbitrary seismic source is defined by a multipole expansion in spherical harmonics. Calculation of the multipole coefficients requires a double integration over the surface of a sphere in the elastic region. The symmetry properties defined above can be applied in order to derive the non-vanishing multipole coefficients for any axially symmetric source. While the nonzero coefficients derived in this manner define the equivalent elastic source for a specific configuration in the source coordinate system, the coefficients for any other configuration can be obtained from this set by

performing the appropriate transformations to the source coordinate system.

The multipole coefficients in the time domain (see Bache, et al. [May, 1975]) can be expressed as

$$\begin{pmatrix} A_{\ell m}^{(\alpha)}(R, t) \\ B_{\ell m}^{(\alpha)}(R, t) \end{pmatrix} = C_{\ell m} \int_0^{2\pi} \int_0^{\pi} \chi^{(\alpha)}(R, \theta, \phi, t) \times P_{\ell}^m(\cos \theta) \sin \theta d\theta \begin{pmatrix} \cos m\phi \\ \sin m\phi \end{pmatrix} d\phi, \quad (C.10)$$

where

$$C_{\ell m} = \frac{\epsilon_m (2\ell+1) (\ell-m)!}{4\pi (\ell+m)!}$$

with  $\epsilon_0 = 1$  and  $\epsilon_m = 2$ ,  $m \neq 0$  and  $P_{\ell}^m$  are associated Legendre functions; the double integration is carried out on a sphere of radius  $R$  in the elastic region and  $\alpha = 1, 2, 3, 4$  corresponds to the dilatational ( $\alpha=4$ ) and rotational potential ( $\alpha=1, 2, 3$ ).

#### C.2.1 Axial Symmetry Only

The case in which the seismic source exhibits only axial symmetry will be considered first. The integration in can be carried out explicitly by utilizing the following integral properties:

$$\int_0^{2\pi} \begin{pmatrix} \cos m\phi \\ \sin m\phi \end{pmatrix} d\phi = \begin{pmatrix} 0 & m \neq 0; & 2\pi & m = 0 \\ 0 & & & \end{pmatrix} \quad (C.11)$$



$$\int_0^{2\pi} \sin\phi \begin{Bmatrix} \cos m\phi \\ \cos m\phi \end{Bmatrix} d\phi = \begin{Bmatrix} 0 \\ \pi \quad m = 1 \end{Bmatrix} \quad (\text{C.12})$$

$$\int_0^{2\pi} \cos\phi \begin{Bmatrix} \cos m\phi \\ \sin m\phi \end{Bmatrix} d\phi = \begin{Bmatrix} \pi \quad m = 1 \\ 0 \end{Bmatrix} \quad (\text{C.13})$$

Since the dilatational potential  $\chi^{(4)}$  is independent of  $\phi$ , the only nonvanishing P wave multipole coefficient must have  $m = 0$ ,

$$A_{\ell 0}^{(4)}(R, t) = 2\pi C_{\ell 0} \int_0^\pi \chi^{(4)}(R, \theta, t) P_\ell(\cos\theta) \sin\theta d\theta, \quad (\ell = 0, 1, 2, 3, \dots) \quad (\text{C.14})$$

$$B_{\ell m}^{(4)}(R, t) = 0 \quad (\text{C.15})$$

Using the relationship (Eq. (C.4)) between the two nonzero rotation potential components  $\chi^{(1)}$  and  $\chi^{(2)}$  and the azimuthal potential  $\chi_\phi$ , the rotation potentials can be reduced to the following single integrals.

$$\begin{Bmatrix} A_{\ell m}^{(1)}(R, t) \\ B_{\ell m}^{(1)}(R, t) \end{Bmatrix} = C_{\ell m} \int_0^{2\pi} \chi_\phi(R, \theta, t) P_\ell^m(\cos\theta) \sin\theta d\theta \times \int_0^{2\pi} (-\sin\phi) \begin{Bmatrix} \cos m\phi \\ \sin m\phi \end{Bmatrix} d\phi, \quad (\text{C.16})$$

$$A_{\ell m}^{(1)}(R, t) = 0 \quad (\text{C.17})$$

$$B_{\ell 1}^{(1)}(R, t) = -\pi C_{\ell 1} \int_0^{\pi} \chi_{\phi}(R, \theta, t) P_{\ell}^1(\cos \theta) \sin \theta d\theta,$$

$$(\ell = 1, 2, 3, \dots) \quad (C.18)$$

$$\begin{pmatrix} A_{\ell m}^{(2)}(R, t) \\ B_{\ell m}^{(2)}(R, t) \end{pmatrix} = C_{\ell m} \int_0^{\pi} \chi_{\phi}(R, \theta, t) P_{\ell}^m(\cos \theta) \sin \theta d\theta$$

$$\times \int_0^{2\pi} \cos \phi \begin{pmatrix} \cos m\phi \\ \sin m\phi \end{pmatrix} d\phi, \quad (C.19)$$

$$A_{\ell 1}^{(2)}(R, t) = C_{\ell 1} \int_0^{\pi} \chi_{\phi}(R, \theta, t) P_{\ell}^1(\cos \theta) \sin \theta d\theta,$$

$$(\ell = 1, 2, 3, \dots) \quad (C.20)$$

$$B_{\ell m}^{(2)}(R, t) = 0 \quad (C.21)$$

$$A_{\ell m}^{(3)}(R, t) = 0 \quad (C.22)$$

$$B_{\ell m}^{(3)}(R, t) = 0 \quad (C.23)$$

This completes the derivation of the nonvanishing multipole coefficients for an axially symmetric source that does not exhibit any other special symmetry. One result of this reduction is that only a single S wave rotational potential needs to be calculated, since

$$A_{\ell 1}^{(2)}(R, t) = -B_{\ell 1}^{(1)}(R, t). \quad (C.24)$$

The divergence and curl of the displacement field are monitored in the 2D finite difference source calculation at stations on the circular arc of radius  $R$  in the elastic region. If the coordinates used in the 2D source calculation are  $(Y, Z)$  for a rectangular grid or  $(R, \theta)$  for a polar grid (see Figure C.1), one can make the following identification,

$$\begin{aligned}\chi_{\phi}(R, \theta, t) &= -\frac{1}{2} \text{CURLD}(R, \theta, t) = -\frac{1}{2} \text{CURLD}(Y, Z, t), \\ \chi^{(4)}(R, \theta, t) &= \text{DIVD}(R, \theta, t) = \text{DIVD}(Y, Z, t)\end{aligned}\quad (\text{C.25})$$

where

$$R = (Z^2 + Y^2)^{1/2},$$

$$\theta = \tan^{-1}(Y/Z),$$

and DIVD and CURLD are the divergence and curl of the displacement field, respectively, as generated by the source calculation. By applying these relations for  $\chi^{(4)}$  in Eq. (C.14) and for  $\chi_{\phi}$  in Eq. (C.19), the numerical integration in  $\theta$  is carried out in a straightforward fashion.

### C.2.2 Axial and Vertical Symmetry

Whenever the seismic source exhibits symmetry or antisymmetry with respect to reflections in the XY plane, the integration in  $\theta$  can be reduced to

$$\int_0^{\pi/2} \left[ 1 \pm (-)^{\ell+m} \right] \chi^{(\alpha)}(R, \theta, \phi, t) P_{\ell}^m(\cos\theta) \sin\theta \, d\theta, \quad (\text{C.26})$$

Since  $P_{\ell}^m(\cos(\pi-\theta)) = (-)^{\ell+m} P_{\ell}^m(\cos\theta)$ ; the positive (negative) sign in the bracket corresponds to the case where

$\chi^{(\alpha)}$  is symmetric (antisymmetric) with respect to reflection in the XY plane. For the case of axial and vertical symmetry,

$$\begin{aligned}\chi^{(4)}(\pi-\theta) &= + \chi^{(4)}(\theta), \\ \chi^{(1)}(\pi-\theta) &= - \chi^{(1)}(\theta), \\ \chi^{(2)}(\pi-\theta) &= - \chi^{(2)}(\theta).\end{aligned}\tag{C.27}$$

Consequently, the nonvanishing P wave multipole coefficients are reduced to

$$A_{\ell 0}^{(4)}(R, t) = 4\pi C_{\ell 0} \int_0^{\pi/2} \chi^{(4)}(R, \theta, t) P_{\ell}(\cos\theta) \sin\theta d\theta,$$

$$(\ell = 0, 2, 4, \dots)\tag{C.28}$$

Note that the integration in  $\phi$  first eliminates all terms except those with  $m = 0$ ; the  $\theta$  integration eliminates all odd-order terms. The nonvanishing S wave multipole coefficients are reduced to

$$B_{\ell 1}^{(1)}(R, t) = - 2\pi C_{\ell 1} \int_0^{\pi/2} \chi_{\phi}(R, \theta, t) P_{\ell}^1(\cos\theta) \sin\theta d\theta,$$

$$(\ell = 2, 4, 6, \dots)\tag{C.29}$$

$$A_{\ell 1}^{(2)}(R, t) = 2\pi C_{\ell 1} \int_0^{\pi/2} \chi_{\phi}(R, \theta, t) P_{\ell}^1(\cos\theta) \sin\theta d\theta,$$

$$(\ell = 2, 4, 6, \dots)\tag{C.30}$$

In summary, the calculation of the multipole coefficients for a source having axial as well as vertical symmetry is greatly simplified to a set of integrals along an arc ( $0^\circ \leq \theta \leq 90^\circ$ ) at a radius  $R$  in the elastic region. Only a single term is found to be nonzero for each even order multipole, namely that corresponding to  $m = 0$  for P wave terms and  $m = 1$  for S wave terms. The leading term in the equivalent elastic source representation corresponds to a P wave monopole ( $\ell=0$ )  $A_{00}^{(4)}$ , followed by both P wave and S wave quadrupole terms ( $\ell=2$ ),  $A_{20}^{(4)}$ ,  $B_{21}^{(1)}$ ,  $A_{21}^{(2)}$ . Vertical symmetry is often referred to as "quadrupole" symmetry. Multipole coefficients for complex axially symmetric sources were first calculated and applied in teleseismic studies by Cherry, et al. [May, 1975].

### C.2.3 Axial and Vertical Antisymmetry

For an axially symmetric source, which also exhibits vertical antisymmetry with respect to reflections in the XY plane, the relations

$$\begin{aligned}\chi^{(4)}(\pi-\theta) &= -\chi^{(4)}(\theta), \\ \chi^{(1)}(\pi-\theta) &= +\chi^{(1)}(\theta), \\ \chi^{(2)}(\pi-\theta) &= +\chi^{(2)}(\theta),\end{aligned}\tag{C.31}$$

Can be employed in Eq. (C.25) to derive the following non-vanishing multipole coefficients,

$$\begin{aligned}A_{\ell 0}^{(4)}(R, t) &= 4\pi C_{\ell 0} \int_0^{\pi/2} \chi^{(4)}(R, \theta, t) P_\ell(\cos\theta) \sin\theta d\theta, \\ (\ell &= 1, 3, 5, \dots)\end{aligned}\tag{C.32}$$



$$B_{\ell 1}^{(1)}(R, t) = -2\pi C_{\ell 1} \int_0^{\pi/2} \chi_{\phi}(R, \theta, t) P_{\ell}^1(\cos\theta) \sin\theta d\theta,$$

$$(\ell = 1, 3, 5, \dots) \quad (C.33)$$

$$A_{\ell 1}^{(2)}(R, t) = -B_{\ell 1}^{(1)}(R, t).$$

$$(\ell = 1, 3, 5, \dots) \quad (C.34)$$

The leading terms in the equivalent elastic source representation corresponds to a P wave dipole ( $\ell=1$ )  $A_{10}^{(4)}$  and an S wave dipole ( $\ell=1$ )  $B_{11}^{(1)}$  and  $A_{11}^{(2)}$ . Vertical antisymmetry is often referred to as "dipole" symmetry. There is no monopole or quadrupole terms in such a case. The nonzero multipole coefficients are summarized in Table C.3.

### C.3 FAR-FIELD DISPLACEMENT SPECTRA FOR AN AXIALLY SYMMETRIC SOURCE

For the determination of the teleseismic signature for an axially symmetric source, only the far-field portion of the displacement field, which includes only those terms decaying with  $R^{-1}$  in the multipole expansion, is required. The displacement spectrum can be expressed in terms of the potential spectrum by

$$\bar{u}(\underline{R}, \omega) = \frac{1}{k_p^2} \nabla \bar{\chi}(\underline{R}, \omega) + \frac{2}{k_s^2} \nabla \times \bar{\chi}(\underline{R}, \omega), \quad (C.35)$$

where

$$\bar{\chi}^{(4)}(\underline{R}, \omega) = \sum_{\ell=0}^{\infty} A_{\ell 0}^{(4)}(\omega) P_{\ell}(\cos\theta) h_{\ell}^{(2)}(k_p R), \quad (C.36)$$

TABLE C.3  
SUMMARY OF NONVANISHING MULTIPOLE COEFFICIENTS FOR A SOURCE  
WITH AXIAL SYMMETRY ABOUT THE Z-AXIS AND VERTICAL SYMMETRY  
OR ANTISYMMETRY ABOUT THE XY PLANE

Axial Symmetry Only	$A_{00}^{(4)}, A_{10}^{(4)}, A_{20}^{(4)}$	$B_{11}^{(1)}, A_{11}^{(2)}, B_{21}^{(1)}, A_{21}^{(2)}$
	$A_{30}^{(4)}, A_{40}^{(4)}, A_{50}^{(4)}$	$B_{31}^{(1)}, A_{31}^{(2)}, B_{41}^{(1)}, A_{41}^{(2)}, \dots$
	$A_{60}^{(4)}, \dots$	
Axial and Vertical Symmetry	$A_{00}^{(4)}, A_{20}^{(4)}, A_{40}^{(4)}$	$B_{21}^{(1)}, A_{21}^{(2)}, B_{41}^{(1)}, A_{41}^{(2)}$
	$A_{60}^{(4)}, \dots$	$B_{61}^{(1)}, A_{61}^{(2)}, \dots$
Axial and Vertical Antisymmetry	$A_{10}^{(4)}, A_{30}^{(4)}, A_{50}^{(4)}$	$B_{11}^{(1)}, A_{11}^{(2)}, B_{31}^{(1)}, A_{31}^{(2)}$
	$\dots$	$B_{51}^{(1)}, A_{51}^{(2)}, \dots$

$$\bar{\chi}^{(2)}(\underline{R}, \omega) = \sum_{\ell=1}^{\infty} \bar{B}_{\ell 1}^{(2)}(\omega) P_{\ell}^1(\cos \theta) \sin \phi h_{\ell}^{(2)}(k_s R), \quad (C.37)$$

$$\bar{\chi}^{(2)}(\underline{R}, \omega) = \sum_{\ell=1}^{\infty} A_{\ell 1}^{(2)}(\omega) P_{\ell}^1(\cos \theta) \cos \phi h_{\ell}^{(2)}(k_s R), \quad (C.38)$$

$$\bar{\chi}^{(3)}(\underline{R}, \omega) = 0,$$

with

$$\bar{B}_{\ell 1}^{(1)} = \bar{A}_{\ell 1}^{(2)}$$

$$\bar{\chi}^{(2)} = -\cos \phi \bar{\chi}^{(1)};$$

$k_p = \omega/\alpha$ ,  $k_s = \omega/\beta$ , where  $\alpha$  and  $\beta$  are the P wave and S wave body wave velocities, respectively;  $h_{\ell}$  are spherical Hankel functions of the second kind; and the vector  $\underline{R}$  has as spherical components  $R, \theta, \phi$ . The multipole coefficients are calculated by taking the Fourier transform as defined by

$$\bar{A}_{\ell m}^{(\alpha)}(\omega) = \frac{1}{h_{\ell}^{(2)}(k_{\alpha} R)} \int_{-\infty}^{\infty} A_{\ell m}^{(\alpha)}(R, t) e^{-i\omega t} dt. \quad (C.39)$$

The far-field spherical components of the displacement spectrum are

$$\left[ \bar{u}_R(\underline{R}, \omega) \right]_{FF} = -\frac{1}{k_p^2} \frac{\partial}{\partial r} \bar{\chi}^{(4)}(\underline{R}, \omega), \quad (C.40)$$

$$\left[ \bar{u}_{\theta}(\underline{R}, \omega) \right]_{FF} = \frac{2}{k_s^2} \left[ \sin \phi \frac{\partial \bar{\chi}^{(1)}}{\partial r} - \cos \phi \frac{\partial \bar{\chi}^{(2)}}{\partial r} \right] \quad (C.41)$$

$$\left[ \bar{u}_{\phi}(R, \omega) \right]_{FF} = 0, \quad (C.42)$$

where in the far-field and radial displacement results only from P wave terms involving  $\bar{\chi}^{(4)}$  and the transverse displacement is only excited by S wave terms involving  $\chi$ .

In general, for an axially symmetric source the far-field displacement spectrum reduces to

$$\left[ \bar{u}_R(R, \omega) \right]_{FF} = - \frac{e}{k_p^2 R} e^{-ik_p R} \sum_{\ell=0}^{\infty} i^{\ell} \bar{A}_{\ell 0}^{(4)}(\omega) P_{\ell}(\cos \theta) \quad (C.43)$$

$$\left[ \bar{u}_{\theta}(R, \omega) \right]_{FF} = \frac{e}{k_s^2 R} e^{-ik_s R} \sum_{\ell=0}^{\infty} i^{\ell} \bar{B}_{\ell 1}^{(1)}(\omega) P_{\ell}^1(\cos \theta), \quad (C.44)$$

If the source exhibits axial plus vertical symmetry, the leading terms for the displacement spectrum are

$$\begin{aligned} \left[ \bar{u}_R(R, \omega) \right]_{FF} = - \frac{e}{k_p^2 R} e^{-ik_p R} & \left\{ \bar{A}_{00}^{(4)}(\omega) - \bar{A}_{20}^{(4)}(\omega) P_2(\cos \theta) \right. \\ & + \bar{A}_{40}^{(4)}(\omega) P_4(\cos \theta) \\ & \left. + \dots \right\} \quad (C.45) \end{aligned}$$

$$\begin{aligned} \left[ \bar{u}_{\theta}(R, \omega) \right]_{FF} = \frac{2}{k_s^2 R} e^{-ik_s R} & \left\{ -\bar{B}_{21}^{(1)}(\omega) P_2^1(\cos \theta) \right. \\ & + \bar{B}_{41}^{(1)}(\omega) P_4^1(\cos \theta) \\ & \left. + \dots \right\} \quad (C.46) \end{aligned}$$

For the case of axial symmetry plus vertical antisymmetry, the leading terms for the displacement spectrum are

$$\left[ \bar{u}_R(R, \omega) \right]_{FF} = + \frac{ie}{k_p^2} e^{-ik_p R} \left\{ \bar{A}_{10}^{(4)}(\omega) \cos\theta - \bar{A}_{30}^{(4)}(\omega) P_3(\cos\theta) + \dots \right\} \quad (C.47)$$

$$\left[ \bar{u}_R(R, \omega) \right]_{FF} = \frac{2ie}{k_s^2} e^{-ik_s R} \left\{ \bar{B}_{11}^{(1)}(\omega) P_1^1(\cos\theta) - \bar{B}_{31}^{(1)}(\omega) P_3^1(\cos\theta) + \dots \right\} \quad (C.48)$$



APPENDIX D  
DESCRIPTION OF A TYPICAL CALCULATION

Teleseismic ground motion is determined by linking the source calculations performed by Applied Theory, Inc. (ATI) with elastic wave propagation methods. This has been accomplished numerically by means of the MULTEES series of general purpose computer routines developed at S<sup>3</sup>. MULTEES calculates the MULTipole coefficients for the Equivalent Elastic Source representation for any arbitrary numerical source, which has been carried into the small displacement elastic region. MULTEES accepts the output generated in either a rectangular or spherical (polar) coordinate grid system by any two or three dimensional finite difference source code.

A brief outline of the key steps in the computational procedure will be presented in order to illustrate selected features of a typical calculation. Three numerical procedures will be described, namely:

1. Preprocessing of the ground motion fields and generation of the displacement potential fields (MULTEES.M2);
2. Calculation of the multipole coefficients in the time domain for the equivalent elastic source (MULTEES.M4);
3. Calculation of the Fourier transform of the multipole coefficients (MULTEES.M5).

The corresponding computer program applied in each step is indicated in parenthesis. Once the set of multipole coefficients has been generated at selected frequencies, far-field displacement spectra and ground motion can be calculated.

## D.1 PREPROCESSING OF THE 2D SOURCE OUTPUT

### D.1.1 Raw 2D Source Calculation Output

The configuration for a near surface explosion source with a depth of burial given by DOB is illustrated in Figure D.1. For each of the sources calculated by ATI, the 2D output data for the ground motion fields consist of the following quantities at 190 stations for each time cycle:

T	Time (sec)
UH	Horizontal component of velocity (cm/sec)
UV	Vertical component of velocity (cm/sec)
SIGH	Horizontal component of stress (dynes/cm <sup>2</sup> )
SIGV	Vertical component of stress (dynes/cm <sup>2</sup> )
SIGPHI	Azimuthal component of stress (dynes/cm <sup>2</sup> )
SIGHV	In-plane component of shear stress (dynes/cm <sup>2</sup> )
DIVD	Divergence of the displacement field
CURLD	Curl of the displacement field.

The direction of the curl is that of the cross product  $\hat{u}_h \times \hat{u}_v$ , where  $\hat{u}_h$  and  $\hat{u}_v$  define, respectively, a positive horizontal direction and the upward vertical direction. The first 91 monitoring stations were located at 1-degree intervals, starting at the horizontal axis, on a circle of radius  $R_1$ , whose center lies at the ground surface on the axis of symmetry. The second group of 91 stations were also at 1-degree intervals but at a radius  $R_2$ . There are also 8 stations at intervals of 2.5 degrees at a radius of  $R_3$ , starting at the axis of symmetry, where  $R_3 > R_2 > R_1$ . The relationship between the spherical coordinates  $(R, \theta)$  and the rectangular coordinates  $(Z, Y)$  used in the 2D finite difference calculation is also illustrated in Figure D.1. The Z and Y axes represent the vertical and horizontal directions, respectively.

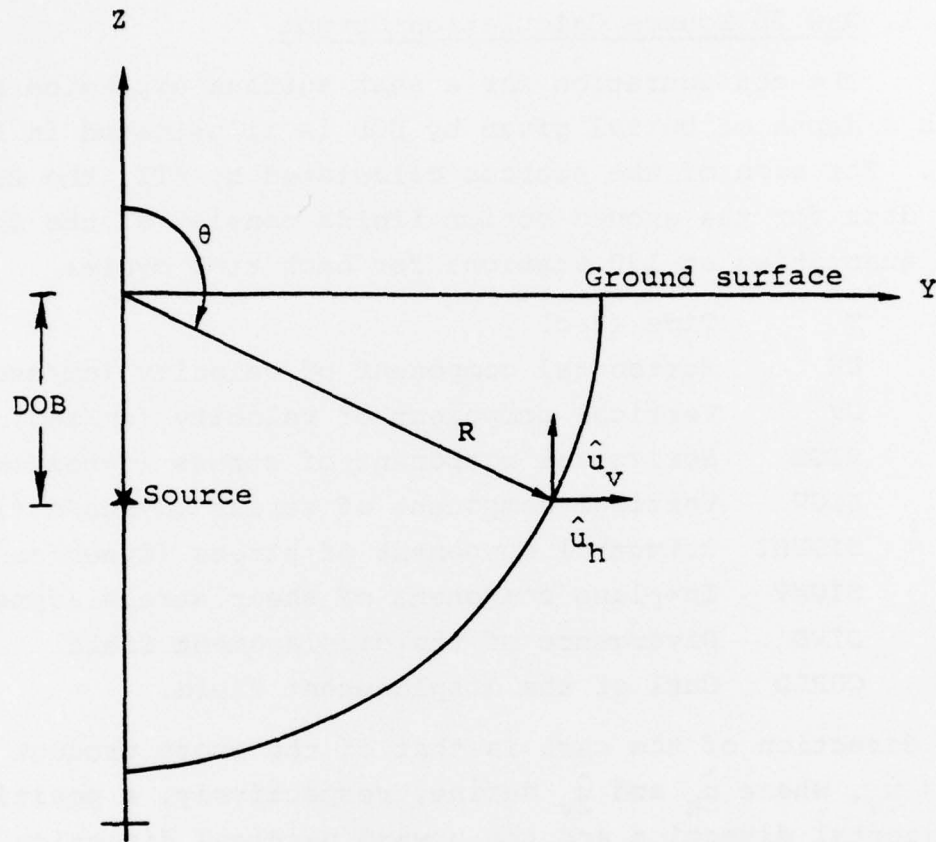


Figure D.1. Configuration and coordinate system for a near surface explosion source with a depth of burial DOB. The relation between the spherical coordinates  $(R, \theta)$  and the rectangular coordinate system  $(Z, Y)$  used in the 2D finite difference calculation is illustrated.

The symmetry properties of the displacement and potential fields of an axially symmetric source are discussed in Appendix C. The derivation of the non-zero multipole coefficients for an axially symmetric source, which is also assumed to have vertical (reflection) symmetry or antisymmetry, is given in Appendix C.2. There it is shown that the calculation of the multipole coefficients in the time domain can be reduced to a numerical integration of these potentials over a single quadrant of the circle of radius  $R$ , namely from  $\theta = 90^\circ$  to  $\theta = 180^\circ$ . The required Cartesian displacement potentials are defined in terms of the 2D source output variables  $(Y, Z)$  as follows:

$$\begin{aligned} \chi^{(1)}(R, \theta, \phi=\pi/2, t) &= \frac{1}{2} \text{CURLD}(Y, Z, t) \\ \chi^{(4)}(R, \theta, t) &= \text{DIVD}(Y, Z, t) \end{aligned} \quad (\text{D.1})$$

where

$$R = (Y^2 + Z^2)^{1/2},$$

$$\theta = \tan^{-1}(Y/Z),$$

and DIVD and CURLD are the divergence and curl output source variables from the 2D finite difference calculation.

The first computational step in a typical calculation consists of a detailed examination of the raw 2D source output data. This is accomplished by a series of computer runs applying various facilities of the MULTEES program M2, including such operations as

1. Plotting versus time all raw output variables at selected stations;
2. Plotting versus angle all raw output variables at selected times;



3. Listing the complete set of raw output data at selected times.

For monitoring purposes, simple "printer plots", which are generated routinely by the MULTEES programs, are most convenient and appropriate. In addition to the eight raw output variables defined above, radial (R) and colatitude ( $\theta$ ) components of particle velocity and acceleration are also computed and plotted versus both angle and time. The objective of all of this preprocessing is

1. To identify the general characteristics of the raw source calculation.
2. To check if the numerical solution has reached or is approaching a steady-state condition at the last time cycles.
3. To identify any special features or peculiarities of the numerical data.

The magnitude as well as the general shape of the ground motion fields were compared with other 2D axisymmetric calculations for complex explosion sources. As a result of such comparisons, the features which are unique to cratering calculations were further highlighted.

The angular variation of the displacement potentials  $\chi^{(1)}$  and  $\chi^{(4)}$  on the elastic radius at a few selected times is illustrated in Figures D.2-D.4 for two typical cases. The calculations are identified by number in Section III of this report. In these graphs the horizontal axis gives the colatitude angle  $\theta$  in degrees, which measures the position of each of the 91 monitoring stations on the elastic radius with respect to the upward vertical position; the left and right boundaries correspond to the free surface ( $\theta = 90^\circ$ ) and the downward vertical direction ( $\theta = 180^\circ$ ), respectively. Figures D.2(a), (b) and (c) display the divergence (with



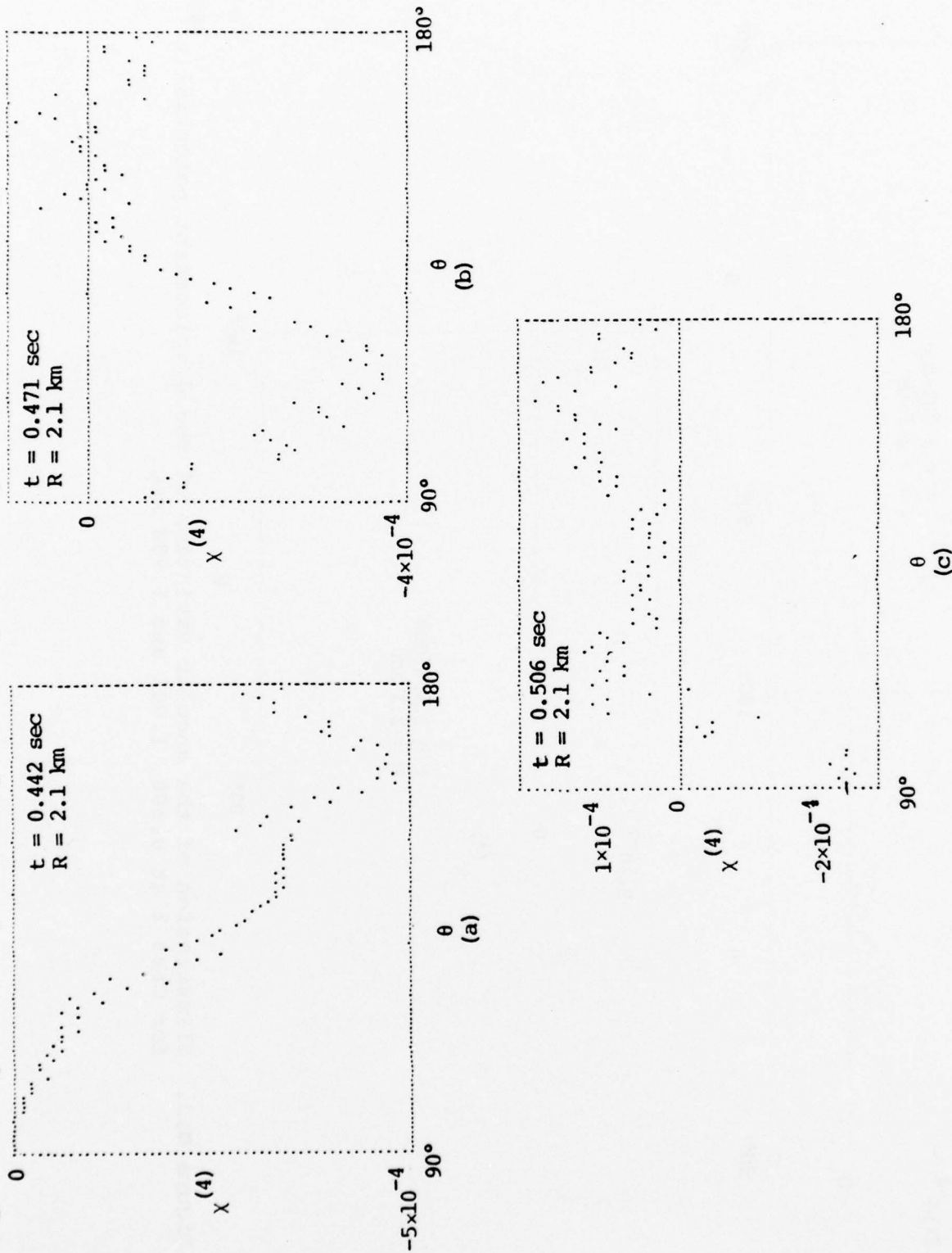


Figure D.2. Illustration of angular variation of displacement potential  $\chi^{(4)}$  at selected times for Case 1. Figures (a), (b) and (c) display the divergence (with overburden removed) at times of 0.442, 0.471 and 0.506 sec.

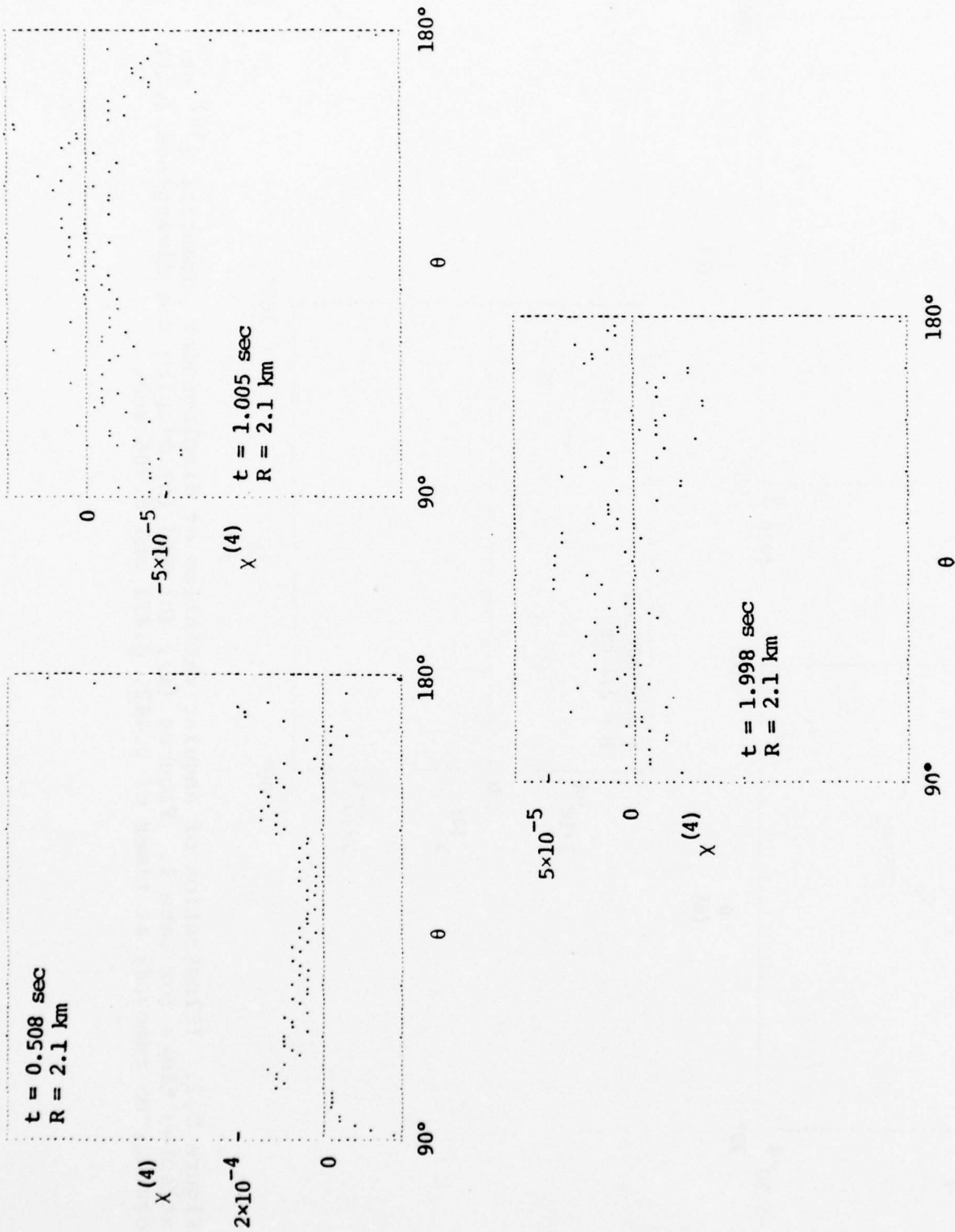


Figure D.3. Illustration of the angular variation of the displacement potential  $\chi^{(4)}$  for Case 2 at 0.508, 1.005 and 1.998 sec.

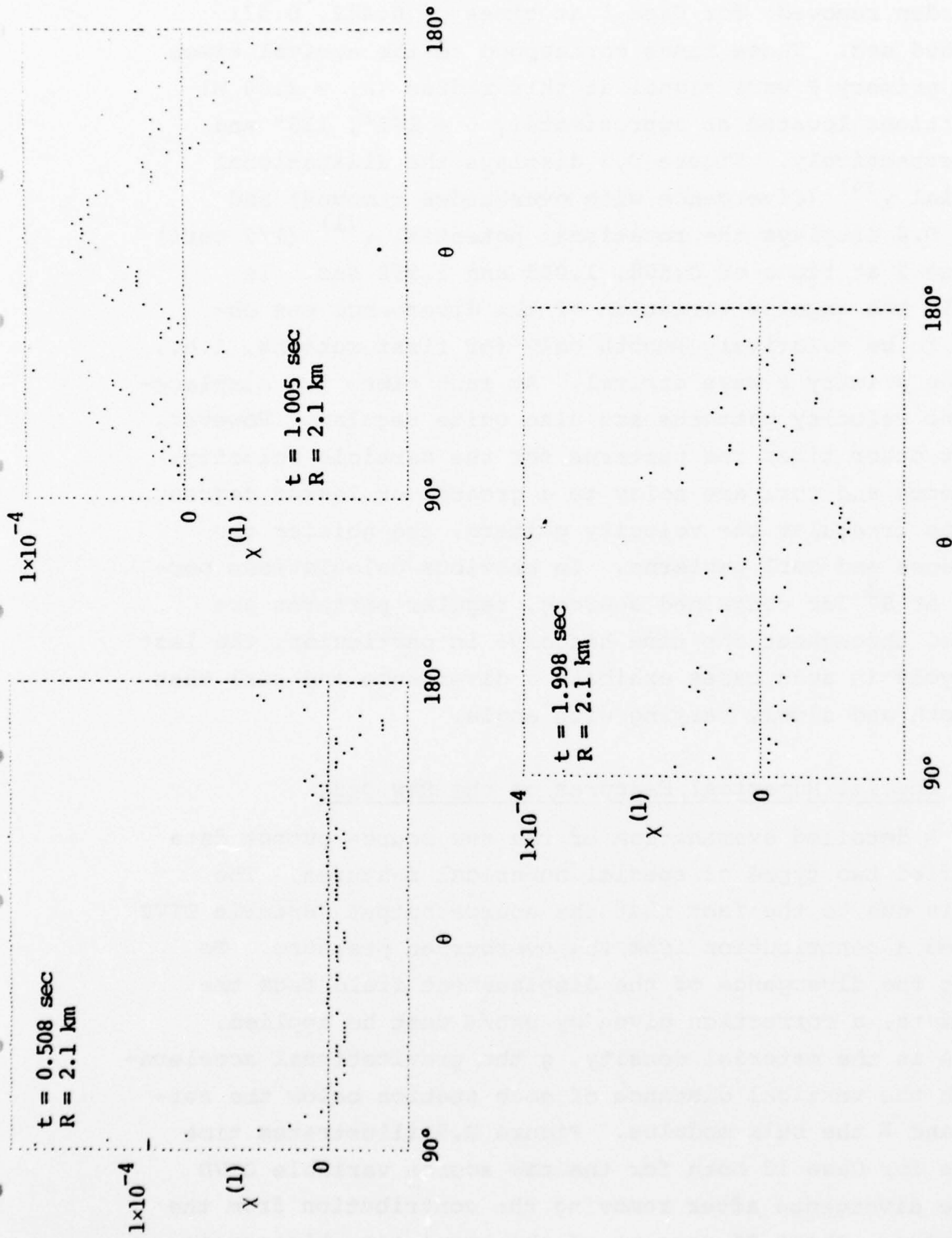


Figure D.4. Illustration of the angular variation of the displacement potential  $\chi^{(1)}$  ( $1/2 \times \text{curl}$ ) for Case 2 at 0.508, 1.005 and 1.998 sec.

overburden removed) for Case 1 at times of 0.442, 0.471 and 0.506 sec. These times correspond to the arrival times of the primary P wave signal at this radius ( $R_1 = 2100$  M) for stations located at approximately  $\theta = 161^\circ$ ,  $118^\circ$  and  $98^\circ$ , respectively. Figure D.3 displays the dilatational potential  $\chi^{(4)}$  (divergence with overburden removed) and Figure D.4 displays the rotational potential  $\chi^{(1)}$  ( $1/2$  curl) for Case 2 at times of 0.508, 1.005 and 1.998 sec. In general, the angular variation of the divergence was observed to be relatively smooth only for first motions, i.e., near the primary P wave arrival. At such times the displacement and velocity patterns are also quite regular. However, at most other times the patterns for the particle velocity, divergence and curl are noisy to a greater or lesser degree. The more irregular the velocity pattern, the noisier the divergence and curl patterns. In previous calculations performed at  $S^3$  for contained sources, regular patterns are observed throughout the time history; in particular, the last time cycle in such cases exhibits a divergence and curl that is smooth and slowly varying with angle.

#### D.1.2 Special Numerical Features of the Raw Data

A detailed examination of the raw source output data identified two types of special numerical features. The first is due to the fact that the source output variable DIVD included a contribution from the overburden pressure. To extract the divergence of the displacement field from the given data, a correction given by  $\rho gh/K$  must be applied, where  $\rho$  is the material density,  $g$  the gravitational acceleration,  $h$  the vertical distance of each station below the surface, and  $K$  the bulk modulus. Figure D.5 illustrates time records for Case 12 both for the raw source variable DIVD and the divergence after removing the contribution from the overburden. About 25 percent of the total time history is shown.

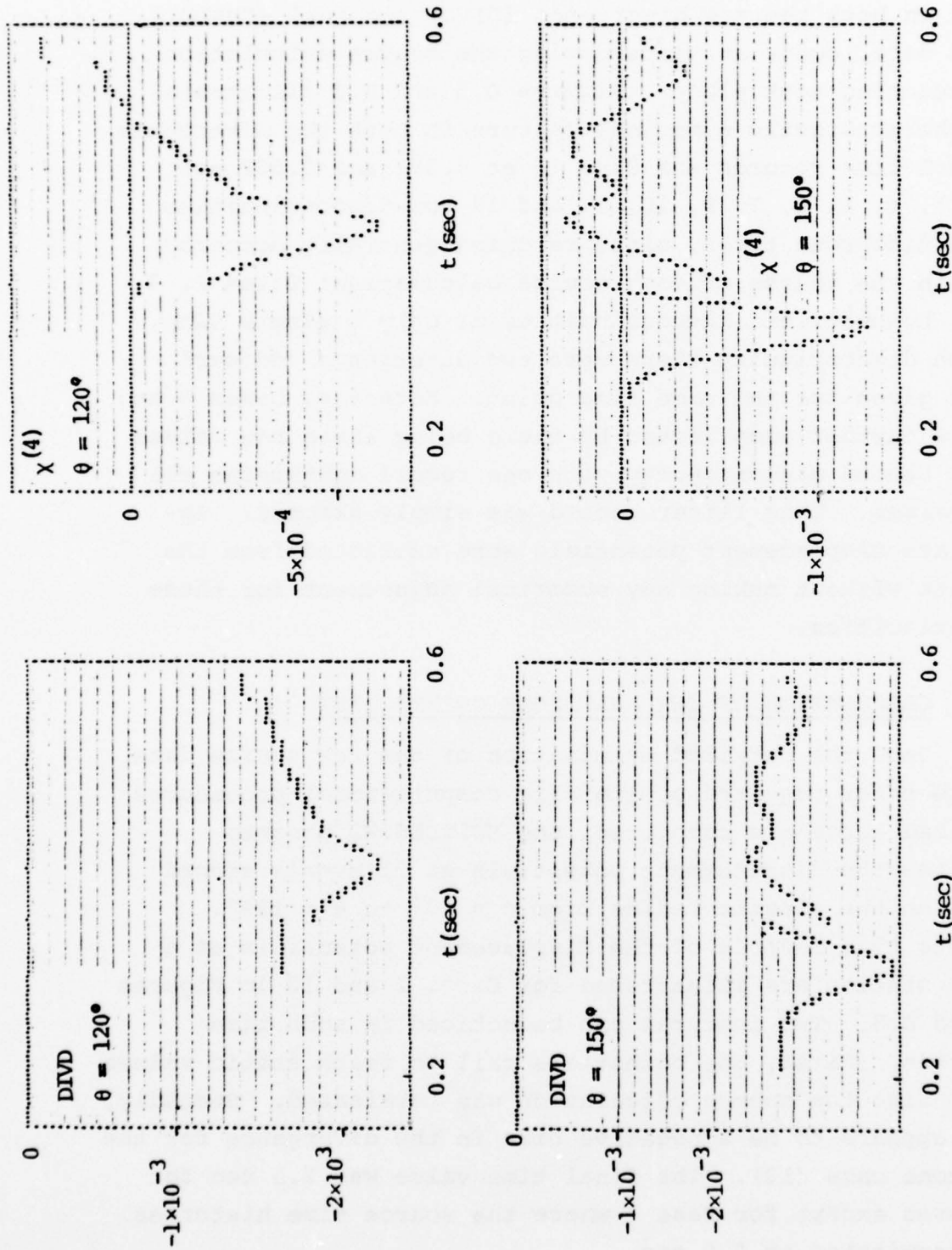


Figure D.5. The time history of the divergence for the first 0.6 seconds of the calculation for Case 12. The graphs on the left represent the raw output (DIVD) generated by the source calculation. In the graphs on the right the overburden correction has been applied to derive the divergence ( $\chi^{(4)}$ ) at  $\theta = 120^\circ$  and  $\theta = 150^\circ$ .



The second class of discontinuities, which were observed in both the raw divergence (DIVD) and curl (CURLD) output data, occur at times during the source calculation when rezoning took place. Figures D.5 and D.6 illustrate this characteristic numerical feature in both the divergence and curl time records for Case 12 at 0.351 and 0.562 sec. Cases 1, 4, 5, 6, 7, 9, 10, 11 and 12 had discontinuities at two different times, since rezoning generally occurred twice in the course of each source calculation; Cases 2, 3 and 8, however, had discontinuities at only a single time. At each discontinuity there were two divergence and curl values given for the same time point. Moreover, Cases 9 and 12 were further complicated by there being three raw values at the second discontinuity with one record containing all null values. This latter record was simply skipped. Appropriate displacement potentials were extracted from the raw data without making any numerical adjustment for these discontinuities.

## D.2 CALCULATION OF THE MULTIPOLE COEFFICIENT

Once the detailed examination of the raw source data and the other required preliminary computational procedures described above are completed, the MULTEES.M2 program generates the displacement potentials at 91 evenly spaced points on the elastic radius from  $\theta = 90^\circ$  to  $\theta = 180^\circ$ . Complete time records of the displacement potentials at a single station are illustrated for Cases 2 and 12 in Figures D.7 and D.8. Two features can be noticed in such time histories. First, the potentials fail to reach static values at the time the source calculation was terminated. Secondly, there appears to be a negative bias in the divergence for the sandstone case (12). The final time value was 2.5 sec for all cases except for Case 2 where the source time histories were terminated at 2.0 sec.

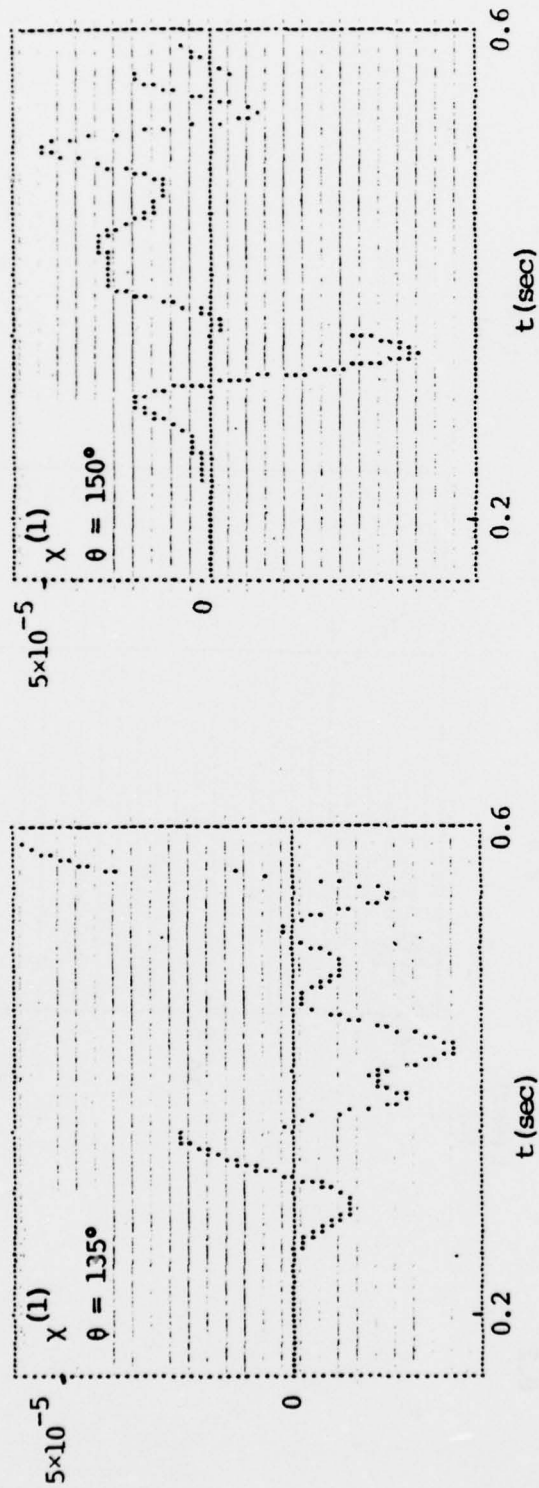


Figure D.6. Illustration of raw source time records for the displacement potential  $\chi(l)$  for Case 12 at  $\theta = 135^\circ$  and  $\theta = 150^\circ$ .

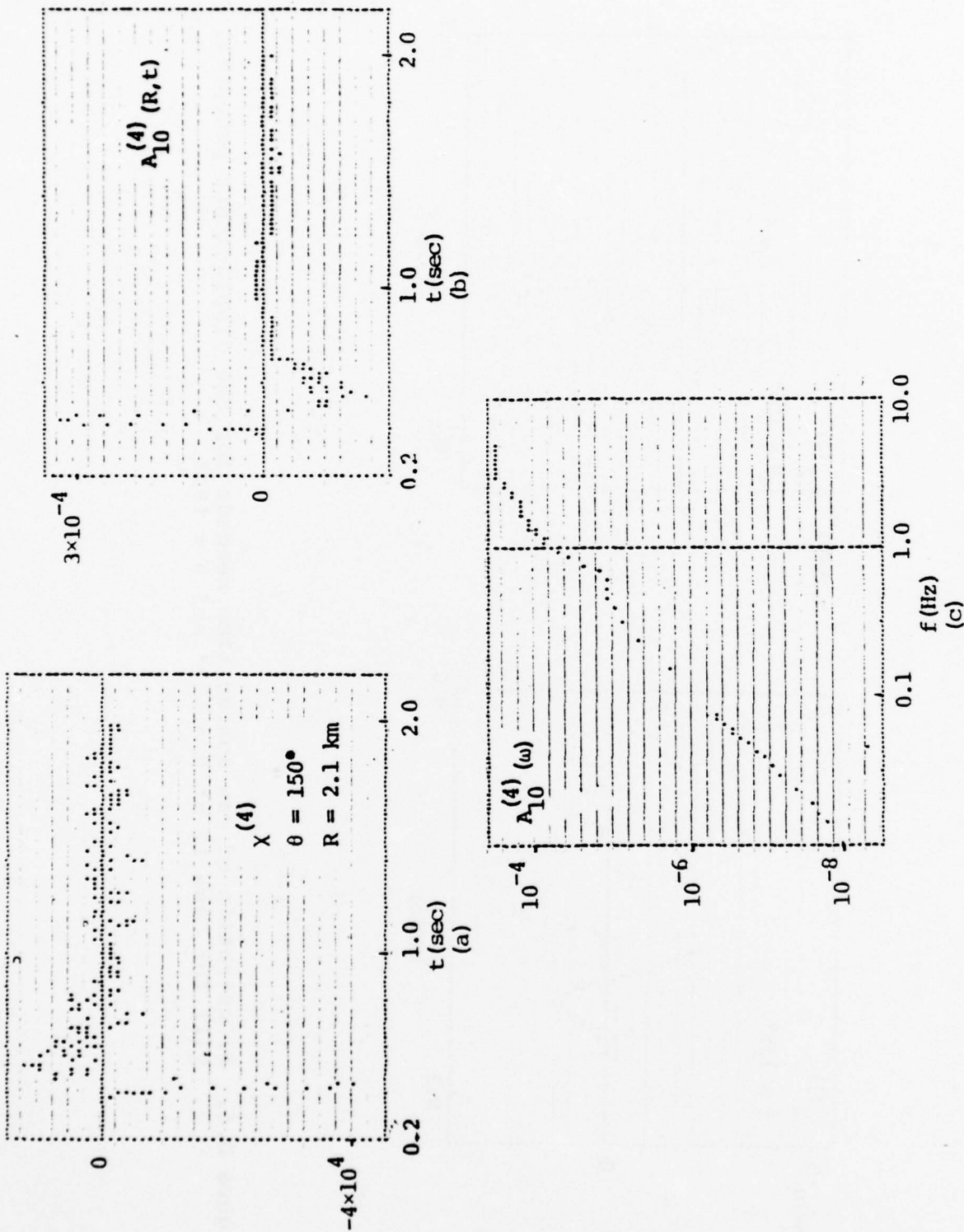


Figure D.7. Illustration of three steps in the numerical computation of the equivalent elastic source for Case 2. Figures (a) and (d) display complete time histories of the displacement potentials  $\chi^{(4)}$  and  $\chi^{(1)}$  at a single station ( $\theta = 150^\circ$ ). Figures (b) and (e) display the dipole P wave and S wave terms  $A_{10}^{(4)}(R, t)$  and  $A_{11}^{(2)}(R, t)$ . Figures (c) and (f) display the transformed P wave and S wave multipole coefficients  $A_{10}^{(4)}(\omega)$  and  $A_{11}^{(2)}(\omega)$ .

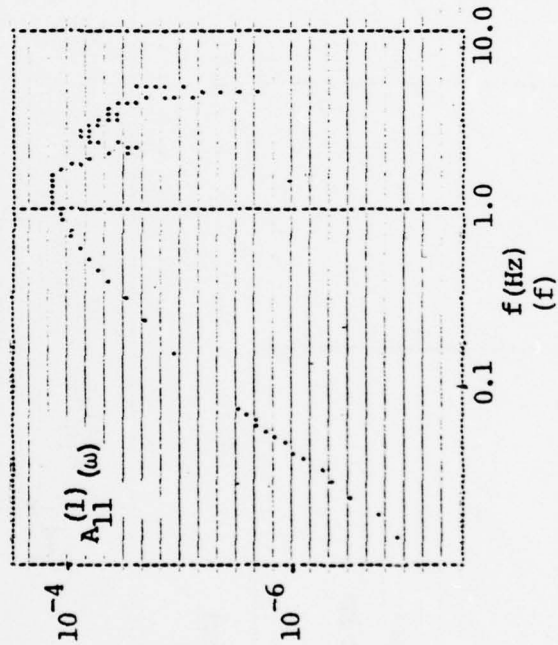
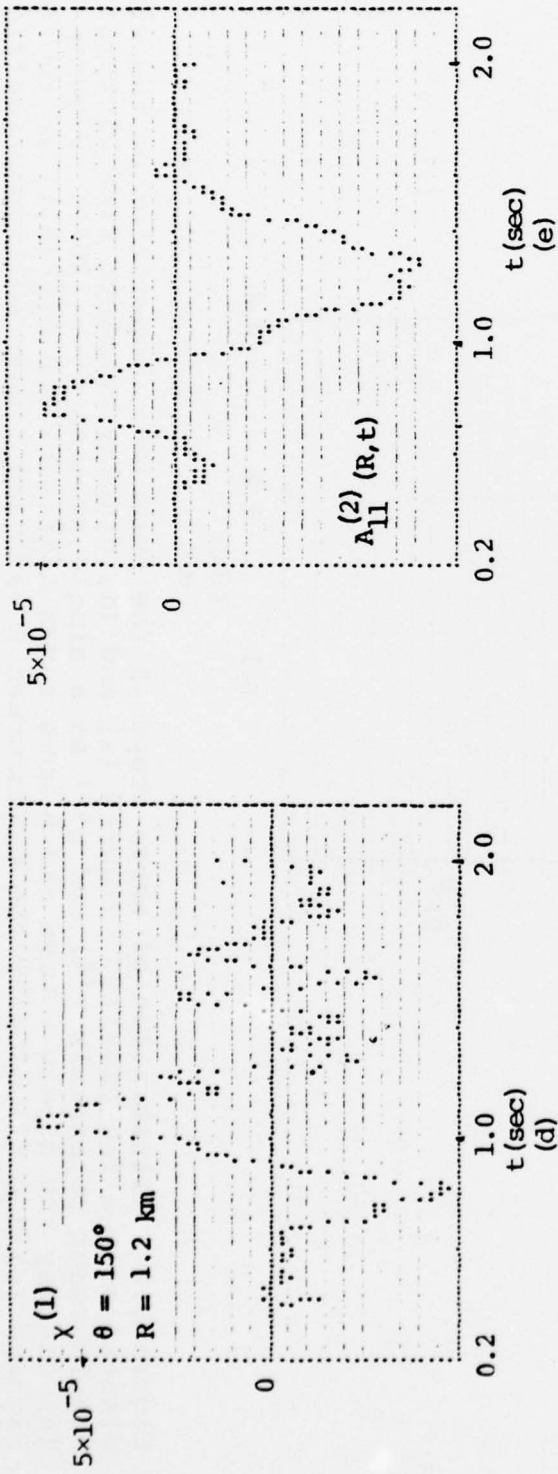


Figure D.7 (Concluded)

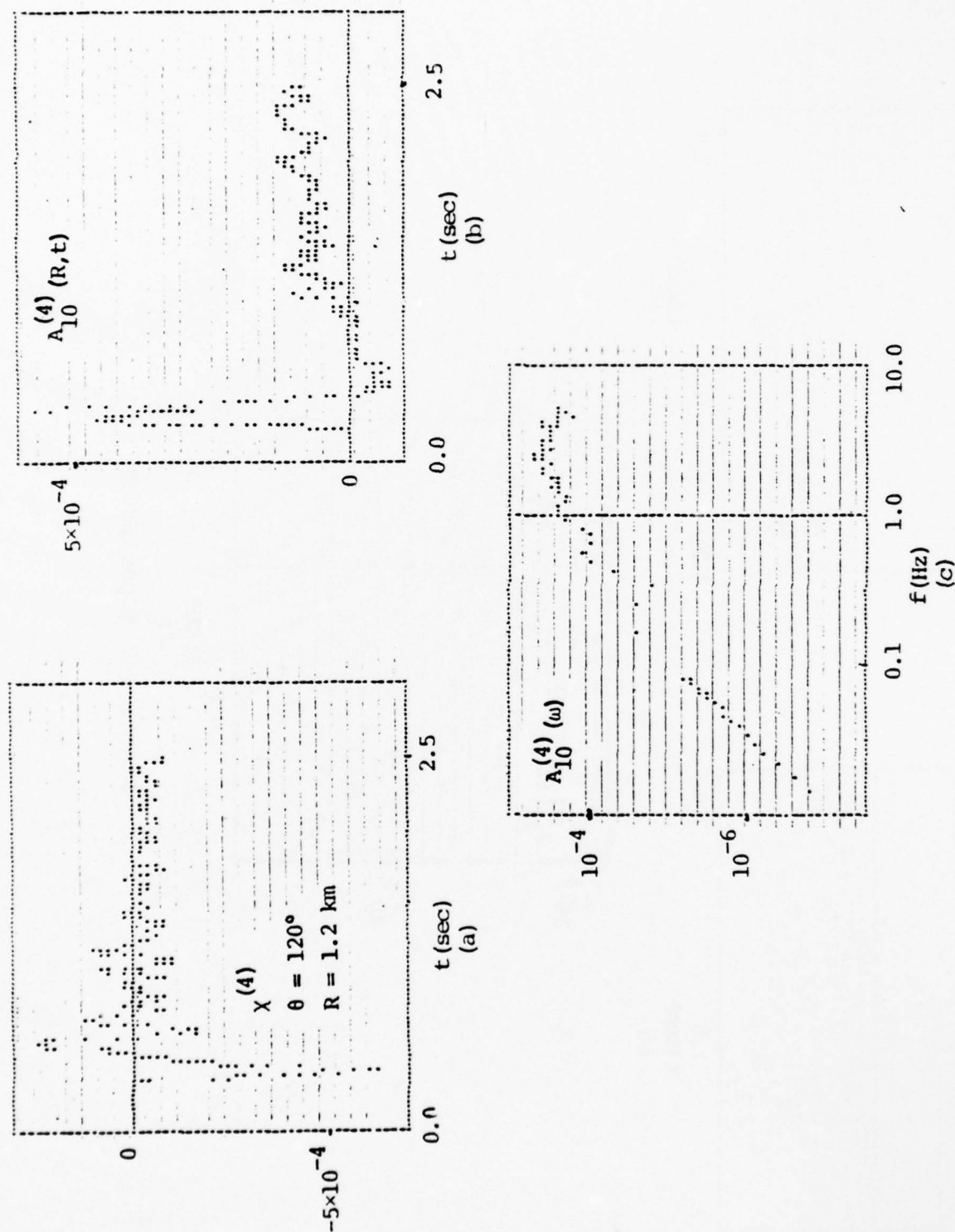


Figure D.8. Illustration of three steps in the numerical computation of the equivalent elastic source for Case 12. Figures (a) and (d) display complete time histories of the displacement potentials  $\chi^{(4)}$  and  $\chi^{(1)}$  at a single station ( $\theta = 120^\circ$ ). Figures (b) and (e) display the dipole P wave and S wave terms  $A_{10}^{(4)}(R,t)$  and  $A_{11}^{(2)}(R,t)$  in the time domain. Figures (c) and (f) display the transformed P wave and S wave multipole coefficients  $A_{10}^{(4)}(\omega)$  and  $A_{11}^{(2)}(\omega)$ .



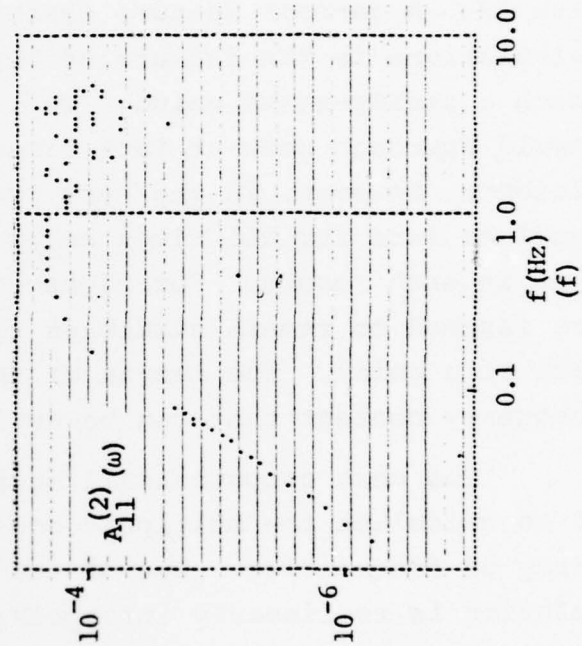
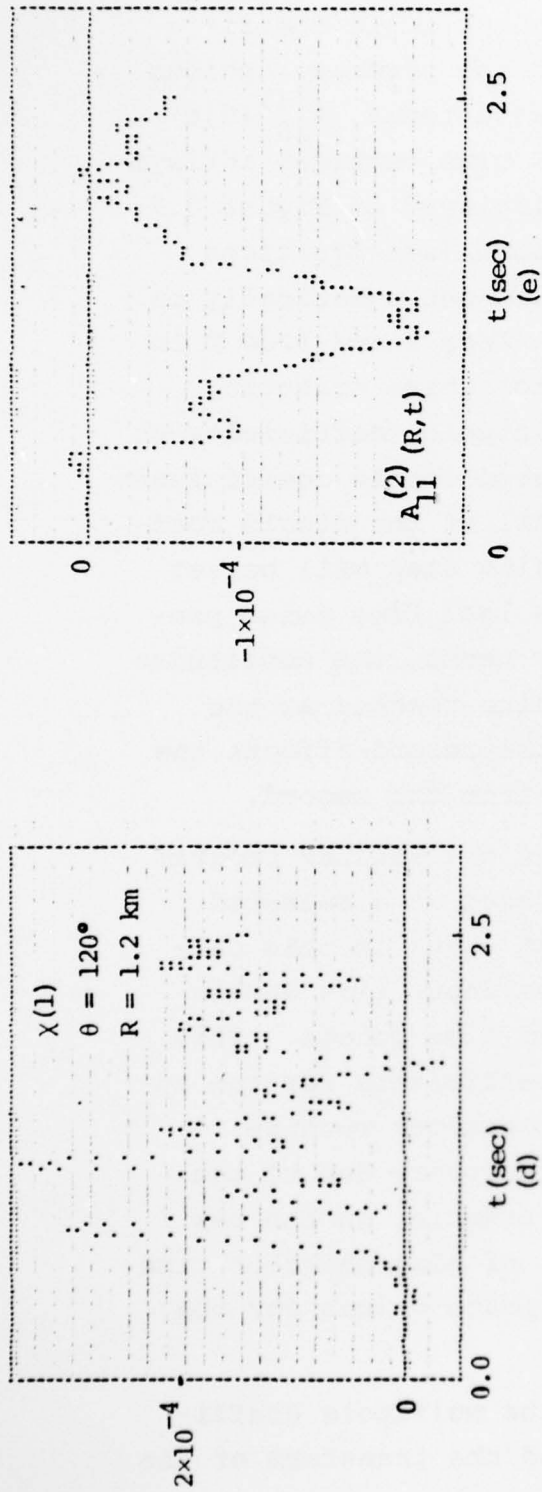


Figure D.8 Concluded

The MULTEES program M4 uses the displacement potentials generated by M2 to calculate the multipole coefficients in the time domain according to the symmetry options specified. The leading P wave and S wave terms,  $A_{10}^{(4)}(R,t)$  and  $A_{11}^{(2)}(R,t)$ , respectively, for axial plus vertical antisymmetry (i.e., "dipole" symmetry) are displayed in Figure D.7 and Figure D.8. The angular integrations (see Equations C.32 and C.33 in Appendix C) are carried out numerically on the elastic radius, which is 2100 M in Case 2 and 1200 M in Case 12. A general feature observed for these cratering calculations is the failure of the multipole coefficients to reach a steady-state value. Well-behaved dipole coefficients should approach zero at late times. All of the dipole coefficients, however, in the next processing step will be set equal to zero for all times beyond the last time point present in each record. For higher-order terms, the amplitudes are assumed to remain static at the value reached at the last time point. The length of the time record affects the frequency content that can be derived from the record.

The next computational step uses the MULTEES program M5 to calculate the multipole coefficients at a selected array of frequencies. One of the first steps in this calculation is to linearly interpolate the input time domain multipole coefficients to evenly spaced time points. This process is necessary to prepare the coefficients for the application of a standard fast Fourier transform routine. Moreover, this removes a possible discrepancy due to the existence of duplicated records. For example, in the raw source output data for Case 2, a total of nine pairs of time cycles were identified containing duplicate values for the variables DIVD and CURLD.

The fast Fourier transform of the multipole coefficient is taken for the dipole terms and the transform of the derivative of the coefficient is taken for terms higher than

dipole for a total of 1024 frequencies. The frequency interval used in each calculation is given as

$$\Delta f = \frac{1}{2048 \Delta t},$$

where

$$\Delta t = (T_n - T_1)/(n - 1),$$

$T_1, T_n$  = First and last time record ,

$n$  = Number of time cycles processed.

As an illustration, for Case 2

$$\Delta f = 0.076521 \text{ Hz}, T_n = 2.0015 \text{ sec},$$

$$n = 400, T_1 = 0.15517 \text{ sec}.$$

The complex multipole coefficients are transformed to amplitude and phase. The next step is a logarithmic interpretation of the amplitudes and a linear interpolation of the phases to extract values of the multipole coefficients for a set of requested output frequencies. Since some of the output frequencies requested may be below the minimum  $\Delta f$  defined above, the M5 program extrapolates the amplitudes for the dipole terms proportional to  $\omega^{-2}$ . The output from this series of calculations performed by MULTEES.M5 is a set of multipole coefficients for a specified array of frequencies. Multipole coefficients were computed for the twelve different cratering sources up to order  $L = 5$ . Figures D.7 and D.8(c) and (f) display the leading P wave and S wave terms  $A_{10}^{(4)}(\omega)$  and  $A_{11}^{(2)}(\omega)$ , respectively, for Cases 2 and 12. The amplitudes are plotted versus frequency on a log-log scale (logarithms are in base 10). Higher order terms ( $\ell = 3$  and  $\ell = 5$ ) are illustrated in Figures D.9 and D.10 for Cases 2 and 12. It should be pointed out

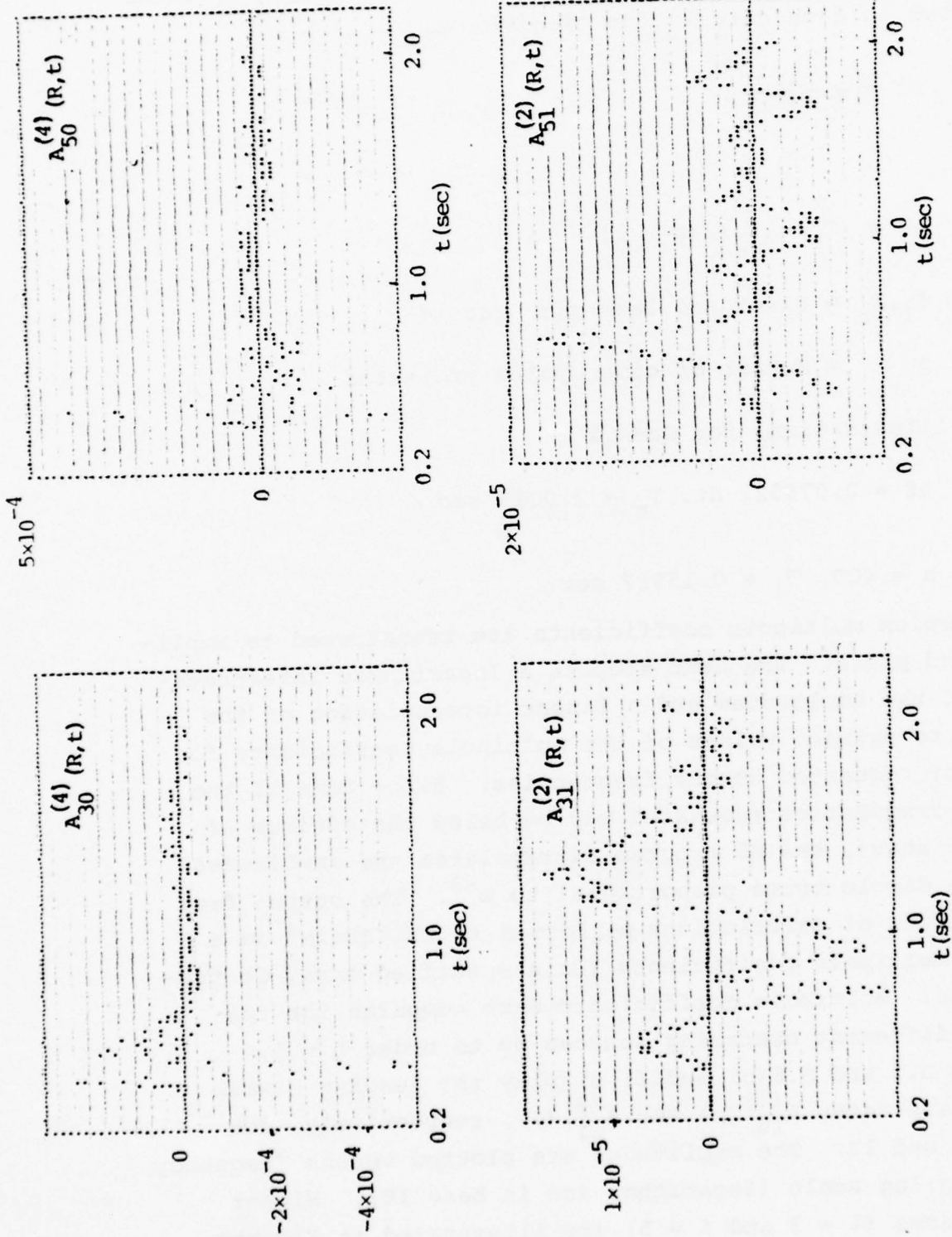


Figure D.9. Illustration of higher order multipole coefficients for Case 2 (granite). The first four graphs display the terms  $A_{30}^{(4)}$ ,  $A_{40}^{(4)}$ ,  $A_{50}^{(4)}$  and  $A_{60}^{(4)}$  in the time domain. The last four (log-log) graphs display the corresponding multipole coefficients  $A_{30}^{(4)}$ ,  $A_{40}^{(4)}$ ,  $A_{50}^{(4)}$  and  $A_{60}^{(4)}$  versus frequency.



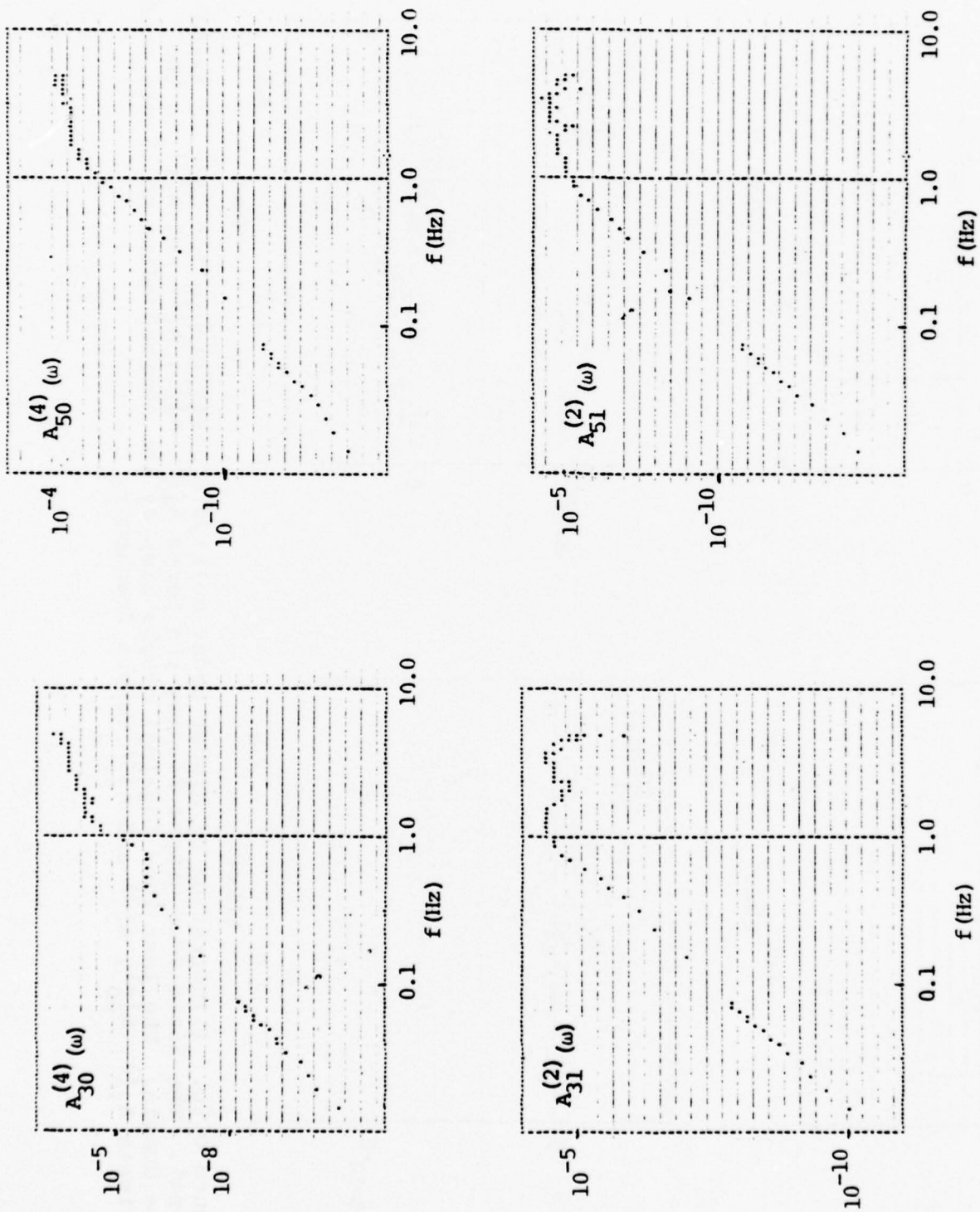


Figure D.9 Concluded



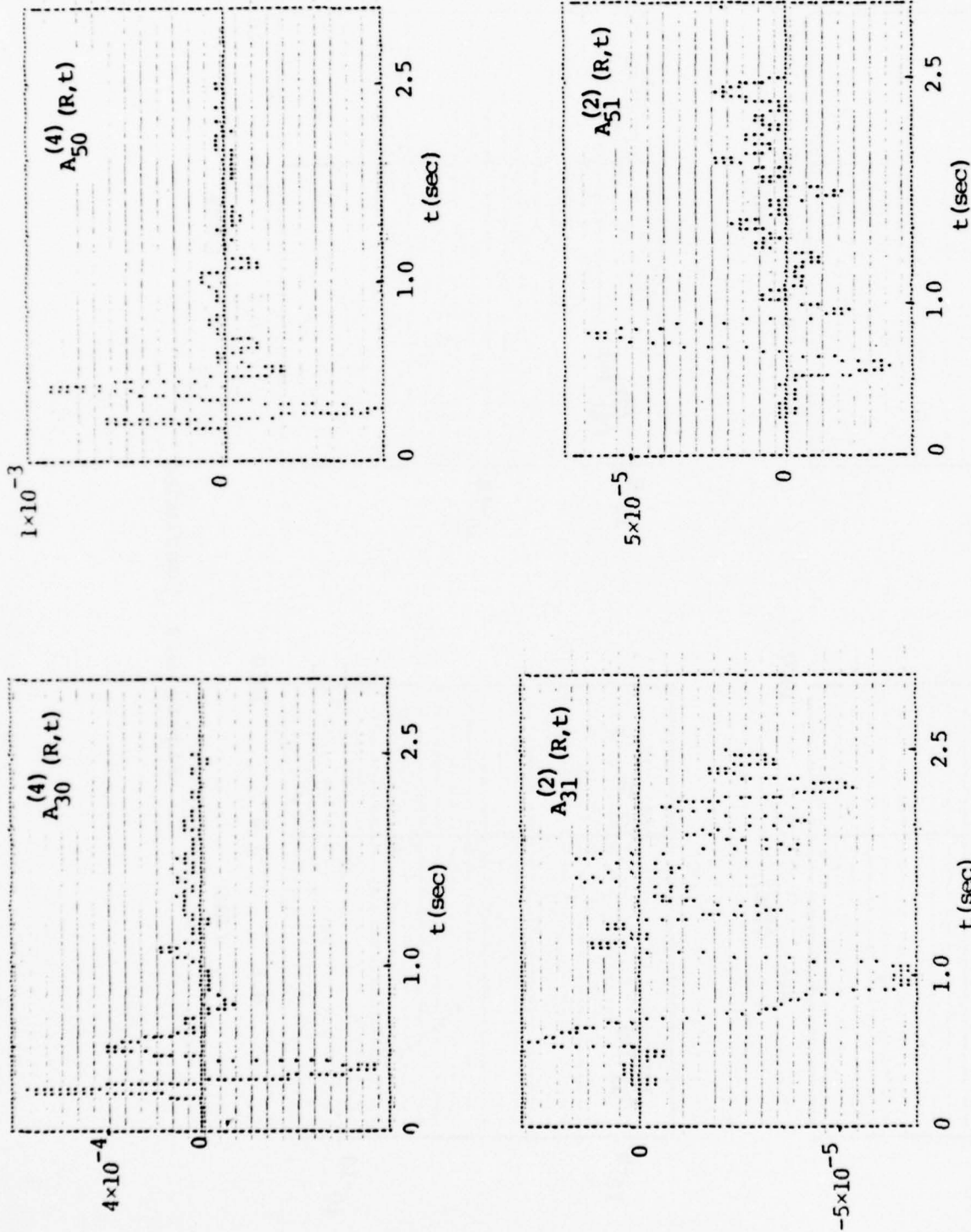


Figure D.10. Illustration of higher order multipole coefficients for Case 12 (sandstone). The first four graphs display the terms  $A_{30}^{(4)}$ ,  $A_{50}^{(4)}$ ,  $A_{31}^{(2)}$  and  $A_{51}^{(2)}$  in the time domain. The last four (log-log) graphs display the corresponding multipole coefficients  $A_{30}^{(4)}$ ,  $A_{50}^{(4)}$ ,  $A_{31}^{(2)}$  and  $A_{51}^{(2)}$  versus frequency.

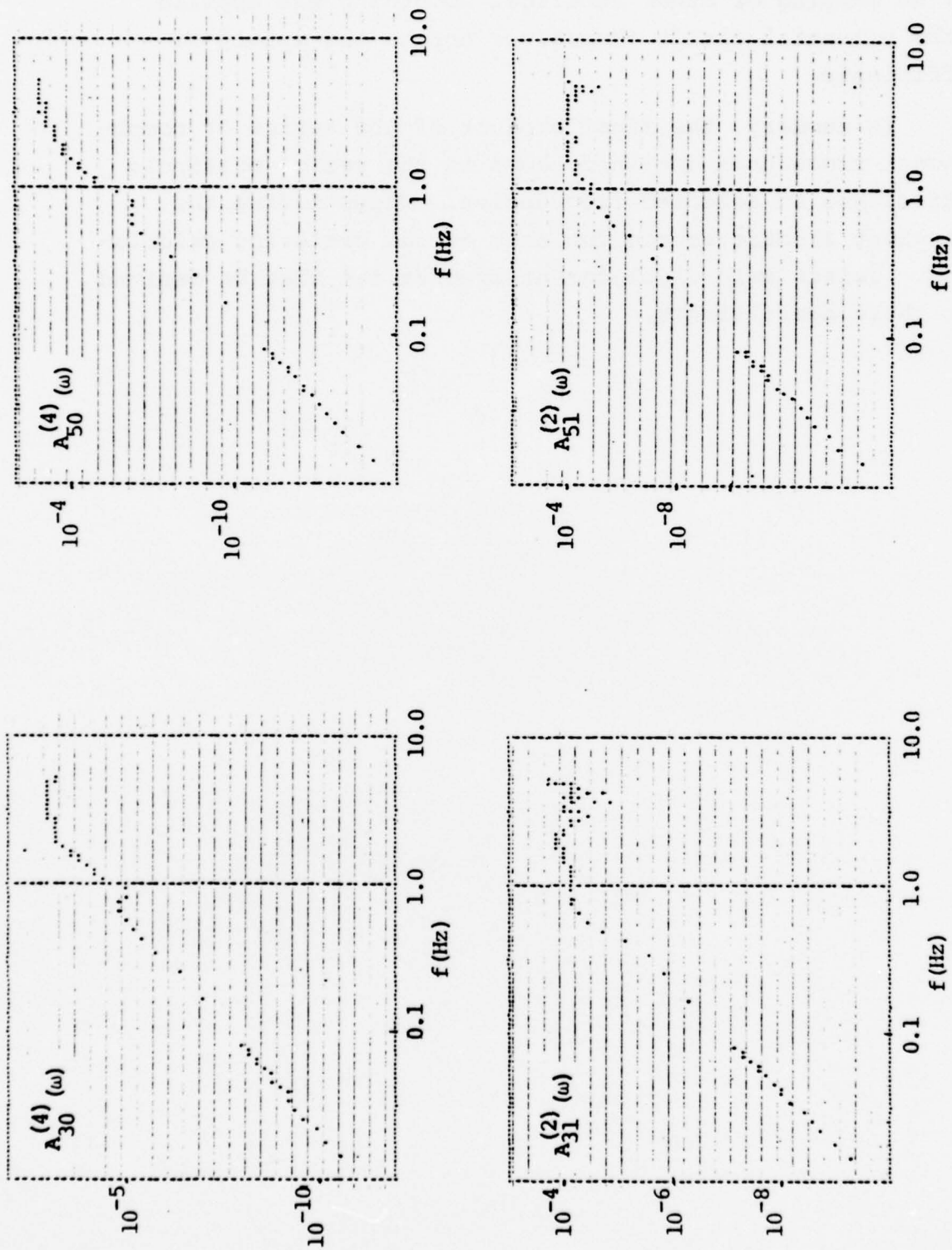


Figure D.10 Concluded

that no damping or other numerical smoothing was applied to the potential fields themselves nor to the multipole coefficients.

In summary, the final product of the series of computational procedures outlined above is the set of multipole coefficients at selected frequencies. These define the equivalent elastic source for each of the cratering calculations. Teleseismic displacement spectra can then be derived from these coefficients.

## APPENDIX E

THE SEISMIC WAVES DUE TO A STRESS DISTRIBUTION APPLIED  
AT THE SURFACE OF A MULTILAYERED HALFSPACEE.1 INTRODUCTION

We consider the elastic waves generated by the application of an axisymmetric stress distribution at the surface of a medium consisting of plane elastic layers. We are interested in both the body and surface waves propagating in the medium. Harkrider [1964, 1970] has derived the appropriate expressions for the Rayleigh waves generated by simple sources at depth in a multilayered halfspace. Harkrider, et al. [1974] extended this theory to the case of an overpressure applied at the free surface. The surface waves generated by the free surface boundary condition of interest here can be obtained from appropriate modification of these results.

For far-field body waves we could follow the procedure used by Fuchs [1966], Hudson [1969] and Bache and Harkrider [1976] for multilayered media, modifying the boundary conditions appropriately. However, it will be sufficient for our purposes to compute the far-field body waves in a homogeneous halfspace. Treatment of this elementary problem is as in Ewing, Jardetsky and Press [1957, Chapter 2].

Let us assume that the surface loading consists of an axisymmetric distribution of normal and shear stress components. The geometry is shown in Figure 1. If we Fourier transform all transient quantities, the free surface boundary conditions are:

$$\begin{aligned} P_{zz}(r, \theta, 0, \omega) &= P_0(r, \omega) , \\ P_{zr}(r, \theta, 0, \omega) &= Q_0(r, \omega) , \end{aligned} \tag{1}$$

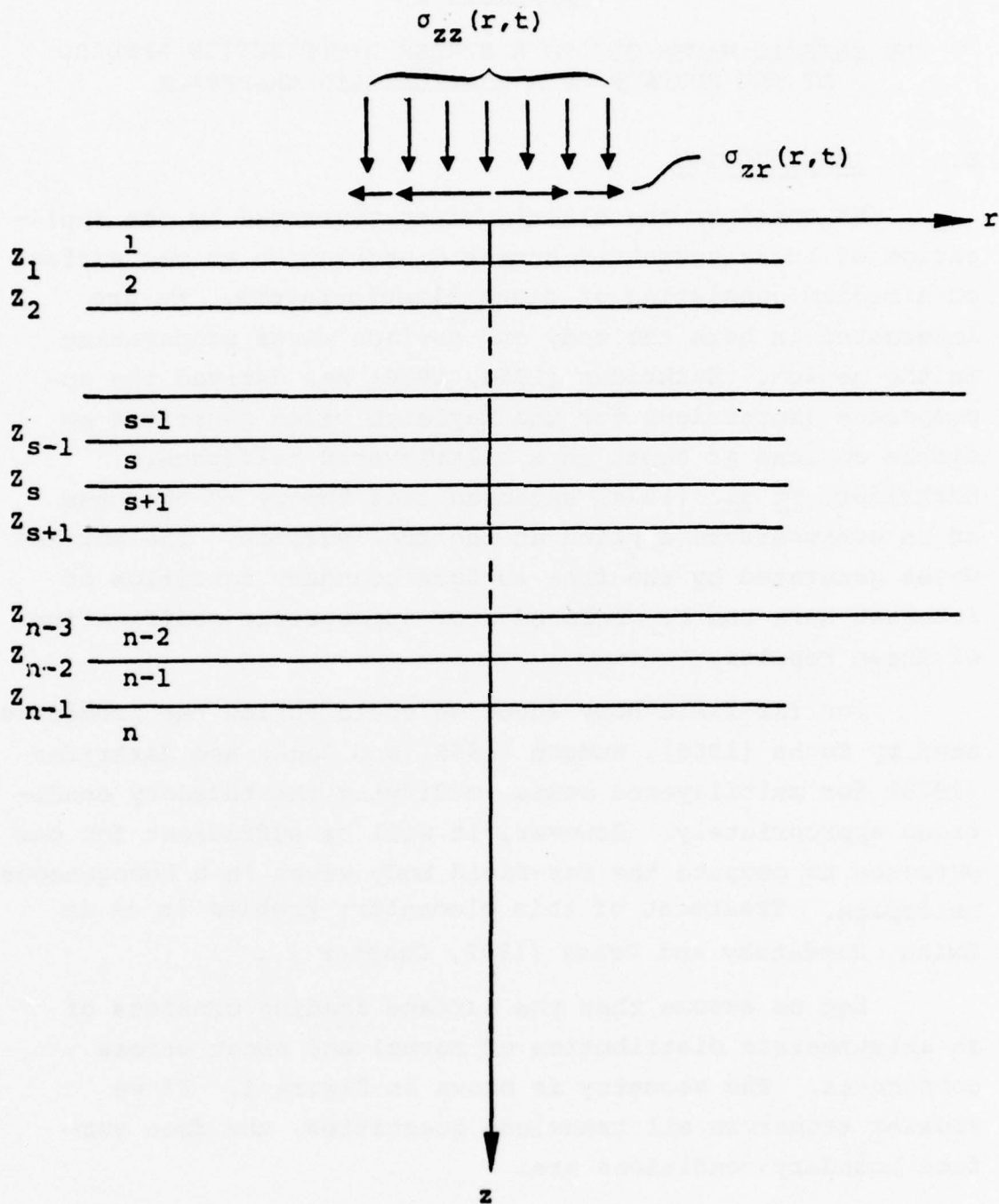


Figure 1. The geometry and coordinate system for an axisymmetric distribution of normal and shear stress applied at the surface of a multilayered halfspace.



where  $P_{zz}$  and  $P_{zr}$  are the Fourier transformed normal and shear stresses and  $P_0$ ,  $Q_0$  represent applied stress distributions.

To solve the problem we first compute the seismic waves for impulse loading. The result is the Green's function solution and the total response may then be obtained by area integration.

## E.2 GREEN'S FUNCTION FORMULATION

For polar coordinates the Green's function for inhomogeneous boundary conditions is the response to boundary loading of the form  $\delta(r-r')/r$  [Morse and Feshbach [1953], Chapter 7]. A convenient representation for our purpose is (e.g., Watson [1966], Section 14.3),

$$\frac{\delta(r-r')}{r} = \int_0^{\infty} J_v(kr) J_v(kr') k dk . \quad (2)$$

For the normal traction boundary condition the appropriate form of (2) has  $v = 0$ . For the shear traction the  $v = 1$  case is appropriate. Therefore, the Green's function boundary conditions are:

$$P_0(r, \omega) = \int_0^{\infty} J_0(kr) J_0(kr') k dk ,$$

$$Q_0(r, \omega) = \int_0^{\infty} J_1(kr) J_1(kr') k dk . \quad (3)$$

The solution is obtained by solving for the seismic waves due to the normal and shear traction boundary conditions (3) applied separately. The result is the Green's functions,  $G_N(r/r')$  and  $G_T(r/r')$ , for the normal and shear tractions. The total solution,  $U_T(\omega)$ , is then given by the spatial integration:

$$U_T(\omega) = \int_0^\infty P_0(r, \omega) G_N(r/r') r' dr' + \int_0^\infty Q_0(r, \omega) G_T(r/r') r' dr'. \quad (4)$$

### E.3 SURFACE WAVES - THE GREEN'S FUNCTION

The formalism of Harkrider [1964] is used to compute the surface waves. Since the problem is axisymmetric, the  $\theta$  dependent quantities vanish. The important steps in the analysis are summarized below. The notations used are essentially the same of those of Harkrider [1964].

Assume a cylindrical coordinate system with origin at the free surface. The geometry is shown in Figure 1. The nonvanishing displacements and stresses in the layers are related to potentials by

$$\begin{aligned} q^i(r, z) &= \frac{\partial \phi^i}{\partial r} + \frac{\partial^2 \psi^i}{\partial r \partial z}, \\ w^i(r, z) &= \frac{\partial \phi^i}{\partial z} + k^2 \psi^i, \end{aligned} \quad (5)$$

$$p_{zz}^i(r, z) = 2\mu_i \left[ \frac{\partial^2 \phi^i}{\partial z^2} + \frac{\partial^3 \psi^i}{\partial z^3} + k_{\beta_i}^2 \frac{\partial \psi^i}{\partial z} \right] - \lambda_i k_{\alpha_i}^2 \phi^i,$$

$$p_{rz}^i(r, z) = \mu_i \left[ \frac{2\partial^2 \phi^i}{\partial z \partial r} + \frac{2\partial^3 \psi^i}{\partial z^2 \partial r} + k_{\beta_i}^2 \frac{\partial \psi^i}{\partial r} \right].$$

Define

$$q^i(r, z) = \int_0^\infty q_i(r, z; k) dk ,$$

$$w^i(r, z) = \int_0^\infty w_i(r, z; k) dk ,$$

$$\phi^i(r, z) = \int_0^\infty \phi_i(r, z; k) dk ,$$

$$\psi^i(r, z) = \int_0^\infty \psi_i(r, z; k) dk ,$$

(6)

$$P_{zz}^i(r, z) = \int_0^\infty P_{zz_i}(r, z; k) dk ,$$

$$P_{rz}^i(r, z) = \int_0^\infty P_{rz_i}(r, z; k) dk .$$

Since the location of material boundaries depends only on  $r$ , the  $r$  and  $z$  dependence of the potentials can be separated:

$$\phi_i(r, z; k) = \phi_i(z) J_0(kr) ,$$

(7)

$$\psi_i(r, z; k) = \psi_i(z) J_0(kr) .$$

If (5) and (6) are substituted into (4) we obtain:

$$\begin{aligned}
 q_i(r, z; k) &\equiv -\frac{1}{k} \frac{\dot{u}_{R_i}}{c} J_1(kr) , \\
 w_i(r, z; k) &\equiv -\frac{i}{k} \frac{\dot{w}_{R_i}}{c} J_0(kr) , \\
 p_{zz_i}(r, z; k) &\equiv \sigma_{R_i}(z) J_0(kr) , \\
 p_{rz_i}(r, z; k) &\equiv -i \tau_{R_i}(z) J_1(kr) ,
 \end{aligned} \tag{8}$$

where the newly introduced normalized velocities and stresses are defined in terms of the potentials in Eq. (7) of Harkrider [1964].

The potentials satisfy the wave equations and therefore may be written

$$\begin{aligned}
 \phi_i(z) &= \tilde{\Delta}'_i e^{-ikr_{\alpha_i} z} + \tilde{\Delta}''_i e^{ikr_{\alpha_i} z} , \\
 \psi_i(z) &= \tilde{\omega}' e^{-ikr_{\beta_i} z} + \tilde{\omega}''_i e^{ikr_{\beta_i} z} .
 \end{aligned} \tag{9}$$

Define

$$\begin{aligned}
 \hat{\Delta}'_i &= -k_{\alpha_i}^2 e^{-ikr_{\alpha_i} z_{i-1}} \tilde{\Delta}'_i , \\
 \hat{\Delta}''_i &= -k_{\alpha_i}^2 e^{ikr_{\alpha_i} z_{i-1}} \tilde{\Delta}''_i , \\
 \hat{\omega}'_i &= ik \frac{k_{\beta_i}^2}{2} e^{-ikr_{\beta_i} z_{i-1}} \tilde{\omega}'_i , \\
 \hat{\omega}''_i &= ik \frac{k_{\beta_i}^2}{2} e^{ikr_{\beta_i} z_{i-1}} \tilde{\omega}''_i .
 \end{aligned} \tag{10}$$

Then continuity of stresses and displacements at layer interfaces may be expressed by

$$\begin{bmatrix} \frac{\dot{u}_{R_i}}{c}(z_i) \\ \frac{\dot{w}_{R_i}}{c}(z_i) \\ \sigma_{R_i}(z_i) \\ \tau_{R_i}(z_i) \end{bmatrix} = a_{R_i} \begin{bmatrix} \frac{\dot{u}_{R_i}}{c}(z_{i-1}) \\ \frac{\dot{w}_{R_i}}{c}(z_{i-1}) \\ \sigma_{R_i}(z_{i-1}) \\ \tau_{R_i}(z_{i-1}) \end{bmatrix}, \quad (11)$$

with  $a_{R_i}$  a matrix with elements given by Eq. (16) of Harkrider [1964].

The relationship between the coefficients in (8) and the velocity-stress vector can be written as

$$\begin{bmatrix} \hat{\Delta}'_i + \hat{\Delta}''_i \\ \hat{\Delta}'_i - \hat{\Delta}''_i \\ \hat{\omega}'_i - \hat{\omega}''_i \\ \hat{\omega}'_i + \hat{\omega}''_i \end{bmatrix} = E_{R_i}^{-1} \begin{bmatrix} \frac{\dot{u}_{R_i}}{c}(z_{i-1}) \\ \frac{\dot{w}_{R_i}}{c}(z_{i-1}) \\ \sigma_{R_i}(z_{i-1}) \\ \tau_{R_i}(z_{i-1}) \end{bmatrix}, \quad (12)$$



Applying the boundary conditions at the free surface,

$$\begin{bmatrix} \frac{\dot{u}_{R_n}}{c} (z_{n-1}) \\ \frac{\dot{w}_{R_n}}{c} (z_{n-1}) \\ \sigma_{R_n} (z_{n-1}) \\ \tau_{R_n} (z_{n-1}) \end{bmatrix} = A_R \begin{bmatrix} \frac{\dot{u}_{R_0}}{c} \\ \frac{\dot{w}_{R_0}}{c} \\ \sigma_{R_0} \\ \tau_{R_0} \end{bmatrix}, \quad (13)$$

where  $A_R = a_{R_{n-1}} \cdot a_{R_{n-2}} \cdots a_{R_1}$ .

From (11) and (9) together with the condition that there be no radiation from infinite depth,

$$\begin{bmatrix} \hat{\Delta}'_n \\ \hat{\Delta}'_n \\ \hat{\omega}'_n \\ \hat{\omega}'_n \end{bmatrix} = E_{R_n}^{-1} \begin{bmatrix} \frac{\dot{u}_{R_n}}{c} (z_{n-1}) \\ \frac{\dot{w}_{R_n}}{c} (z_{n-1}) \\ \sigma_{R_n} (z_{n-1}) \\ \tau_{R_n} (z_{n-1}) \end{bmatrix}. \quad (14)$$

Therefore, we get Harkrider's [1964] equation (62):

$$\begin{bmatrix} \hat{\Delta}'_n \\ \hat{\Delta}'_n \\ \hat{\omega}'_n \\ \hat{\omega}'_n \end{bmatrix} = J \begin{bmatrix} W \\ X \\ Y \\ Z \end{bmatrix} \quad (15)$$

with  $J = E_{Rn}^{-1} A_R$  and  $W, X, Y, Z$  the elements of the vector on the right side of (12); i.e., the free surface velocities and stresses.

The system of equations (14) can be solved for  $W$  and  $X$ . The result is

$$\begin{aligned} \frac{\dot{w}_R}{c} &= - \frac{(GN-LH)Y + (RN-SL)Z}{F_R}, \\ \frac{\dot{u}_R}{c} &= - \frac{(RN-SL)Y + (RN-SK)Z}{F_R}, \end{aligned} \quad (16)$$

where  $F_R, G, N$ , etc. are combinations of elements of the  $J$  matrix given by Harkrider. Rewrite these as

$$\begin{aligned} \frac{\dot{w}_R}{c} &= - \frac{N_R^{(1)}}{F_R}, \\ \frac{\dot{u}_R}{c} &= \frac{N_R^{(3)}}{F_R}. \end{aligned} \quad (17)$$

By (5) and (7)

$$w_0 \equiv w'(r, 0) = - \int_0^\infty \frac{i}{k} \frac{\dot{w}_R}{c} J_0(kr) dk , \quad (18)$$

$$q_0 \equiv q'(r, 0) = - \int_0^\infty \frac{1}{k} \frac{\dot{u}_R}{c} J_1(kr) dk .$$

Then, using (16),

$$w_0 = i \int_0^\infty \frac{N_R^{(1)}}{k F_R} J_0(kr) dk , \quad (19)$$

$$q_0 = - \int_0^\infty \frac{N_R^{(3)}}{k F_R} J_1(kr) dk .$$

For the surface waves we evaluate the residue contribution to these integrals. For  $\omega$  fixed we find for the  $j^{\text{th}}$  mode that the displacements are:

$$\{w_0\}_{R_j} = \frac{\pi}{k_{R_j}} \frac{N_{R_j}^{(1)}}{\left(\frac{\partial F_R}{\partial k}\right)_j} H_0^{(2)}(k_{R_j} r) , \quad (20)$$

$$\{q_0\}_{R_j} = \frac{\pi i}{k_{R_j}} \frac{N_{R_j}^{(3)}}{\left(\frac{\partial F_R}{\partial k}\right)_i} H_1^{(2)}(k_{R_j} r) ,$$

where  $(\partial F_R / \partial k)_j$ ,  $N_{R_j}^{(1)}$ ,  $N_{R_j}^{(3)}$  are evaluated at  $(\omega, k_{R_j})$  such that  $F_R(\omega, k_{R_j}) = 0$ . These can be combined to give

$$\{q_0\}_{R_j} = -i \left[ \frac{\dot{u}_0}{\dot{w}_0} \right]_{H_j} \{w_0\}_{R_j} \frac{H_1^{(2)}(k_{R_j} r)}{H_0^{(2)}(k_{R_j} r)} . \quad (21)$$

where  $[\dot{u}_0/\dot{w}_0]_{H_j} = -K/L$ , the ellipticity.

It remains to cast (19) in a form suitable for computation. We have

$$\begin{aligned} N_{R_j}^{(1)} &= -(GN - LN) \left( Y + \frac{K}{L} Z \right) , \\ &= -i(G^*N - L^*N) \left\{ Y - \left( \frac{\dot{u}_0}{\dot{w}_0} \right)_{H_1} Z \right\} , \end{aligned} \quad (22)$$

where  $G = iG^*$ , etc. Also,

$$\begin{aligned} N_{R_j}^{(3)} &= - \left( \frac{\dot{u}_0}{\dot{w}_0} \right)_{H_j} N_{R_j}^{(1)} , \\ &= (G^*N - L^*N) \left( \frac{\dot{u}_0}{\dot{w}_0} \right)_{H_j} \left\{ Y - \left( \frac{\dot{u}_0}{\dot{w}_0} \right)_{H_j} Z \right\} . \end{aligned} \quad (23)$$

Then the vertical and radial components of the Rayleigh wave displacement are

$$\begin{aligned} \{w_0\}_{R_j} &= -\frac{\pi i}{k_{R_j}} A_{R_j} \left\{ Y - \left[ \frac{\dot{u}_0}{\dot{w}_0} \right]_{H_j} Z \right\} H_0^{(2)}(k_{R_j} r) , \\ \{q_0\}_{R_j} &= -\frac{\pi}{k_{R_j}} \left[ \frac{\dot{u}_0}{\dot{w}_0} \right]_{H_j} A_{R_j} \left\{ Y - \left[ \frac{\dot{u}_0}{\dot{w}_0} \right]_{H_j} Z \right\} H_1^{(2)}(k_{R_j} r) , \end{aligned} \quad (24)$$

where

$$\tilde{A}_{R_j} = \frac{(G^*N - L^*H)}{\left(\frac{\partial F_R}{\partial k}\right)_j} .$$

To complete the Green's function formulation it is necessary to interpret  $Y$  and  $Z$  in terms of the boundary conditions given by (3). From (5) and (7)

$$[P_{zz}]_{z=0} = \int_0^\infty \sigma_{R_0} J_0(kr) dk , \quad (25)$$

$$[P_{rz}]_{z=0} = -i \int_0^\infty \tau_{R_0} J_1(kr) dk ,$$

where  $\sigma_{R_0} \equiv Y$  and  $\tau_{R_0} \equiv Z$ .

Comparing (24) with (1) and (3), we see that

$$\begin{aligned} \sigma_{R_0} &= k J_0(kr') , \\ \tau_{R_0} &= ik J_1(kr') , \end{aligned} \quad (26)$$

give the desired Green's functions. For the two cases of normal and shear traction they are:

Case 1 Applied normal traction: The Green's function is

$$G_N^S(r|r') = -i\pi \tilde{A}_{R_j} J_0(k_{R_j} r') H_0^{(2)}(k_{R_j} r) \quad (27)$$



and the surface wave displacements are given by

$$\{w_0\}_{R_j}^N = G_N^S(r|r') , \quad (28)$$

$$\{q_0\}_{R_j}^N = \epsilon_j \frac{H_1^{(2)}(k_{R_j} r)}{H_0^{(2)}(k_{R_j} r)} G_N^S(r|r') ,$$

where  $\epsilon_j = -i[\dot{u}_0/\dot{w}_0]_{H_j}$  has been introduced.

Case 2 Applied shear traction: The Green's function is

$$G_T^S(r|r') = -i\pi A_{R_j} \epsilon_j J_1(k_{R_j} r') H_0^{(2)}(k_{R_j} r) , \quad (29)$$

and the displacements are given by (27) with  $G_T^S(r|r')$  replacing  $G_N^S(r|r')$ .

#### E.4 SURFACE WAVES - SOLUTION FOR A DISTRIBUTED SURFACE LOAD

Equations (26) and (28) give the Green's functions for normal and shear traction loading applied at the point  $r = r'$ . From these Green's functions we can derive the solutions for loads distributed over the free surface. The basic equation relating the Green's function to the total solution is (4).

##### Case 1: Applied Normal Traction

We consider the boundary conditions (1) and assume initially that  $Q_0(r, \omega)$  vanishes. Let us also assume that the loading is restricted in spatial extent; that is,

$$\begin{aligned} P_{zz}(r, \theta, 0, \omega) &= P_0(r, \omega), \quad a \leq r \leq b, \\ &= 0, \quad \text{elsewhere.} \end{aligned} \quad (30)$$

Then

$$\begin{aligned} \{w_0\}_{R_j}^N &= \int_a^b P_0(r, \omega) G_N(r|r') r' dr', \\ &= -i\pi A_{R_j} H_0^{(2)}(k_{R_j} r) \int_a^b P_0(r', \omega) J_0(k_{R_j} r') r' dr', \end{aligned} \quad (31)$$

and

$$\{q_0\}_{R_j}^N = \epsilon_j \frac{H_1^{(2)}(k_{R_j} r)}{H_0^{(2)}(k_{R_j} r)} \{w_0\}_N.$$

### Case 2: Applied Shear Traction

In this case we compute the displacements for boundary conditions (1) with  $P_0(r, \omega)$  vanishing. Again, let us assume that the loading is applied for  $a \leq r \leq b$ . Then

$$\begin{aligned} \{w_0\}_{R_j}^S &= \int_a^b Q_0(r, \omega) G_T(r|r') r' dr', \\ &= -i\pi A_{R_j} \epsilon_j H_0^{(2)}(k_{R_j} r) \int_a^b Q_0(r', \omega) J_1(k_{R_j} r') r' dr', \\ \{q_0\}_{R_j}^S &= \epsilon_j \frac{H_1^{(2)}(k_{R_j} r)}{H_2^{(2)}(k_{R_j} r)} \{w_0\}_S. \end{aligned} \quad (32)$$

From (31) and (32) we see that the boundary stress-time histories appear only in the spatial integrals

$$\hat{P}(\omega) = \int_a^b P_0(r', \omega) J_0(k_{R_j} r') r' dr',$$

$$\hat{Q}(\omega) = \int_a^b Q_0(r', \omega) J_1(k_{R_j} r') r' dr',$$
(33)

It is necessary to evaluate these integrals for each frequency,  $\omega$ , of interest for the surface wave calculations. In general, this is done numerically.

Since the problem is linear, we can superimpose the solutions (31) and (32) to obtain the solution when both normal and shear tractions are applied. The total Rayleigh wave displacement is

$$\{w_0\}_{R_j} = \{w_0\}_{R_j}^N + \{w_0\}_{R_j}^S,$$

$$\{q_0\}_{R_j} = \{q_0\}_{R_j}^N + \{q_0\}_{R_j}^S$$
(34)

Substituting from (31) and (32), this may be written

$$\{w_0\}_{R_j} = -i\pi A_{R_j} H_0^{(2)}(k_{R_j} r) [\hat{P} + \epsilon_j \hat{Q}],$$

$$\{q_0\}_{R_j} = \epsilon_j \frac{H_1^{(2)}(k_{R_j} r)}{H_0^{(2)}(k_{R_j} r)} \{w_0\}_{R_j}.$$
(35)

where  $\hat{P}$  and  $\hat{Q}$  are given by the integrals (33). Finally, note that in the far-field ( $k_{R_j} r \gg 1$ ) we can use the asymptotic approximation for the Hankel functions which is

$$H_j^{(2)}(z) \approx \sqrt{\frac{2}{\pi z}} e^{-i(z - \frac{\nu\pi}{2} - \frac{\pi}{4})}.$$
(36)

Then the expression for  $\{q_0\}_{R_j}$  reduces to

$$\{q_0\}_{R_j} = i \epsilon_j \{w_0\}_{R_j} . \quad (37)$$

For the fundamental mode ( $j = 0$ ) Rayleigh wave  $\epsilon_j < 0$  and (37) prescribes retrograde elliptic particle motion.

#### E.5 BODY WAVES -- THE GREEN'S FUNCTION

As we pointed out in the introduction, we could derive the expressions for the body waves due to distributed surface loading using procedures analogous to those followed for surface waves. However, it will be sufficient to consider only the homogeneous halfspace case which is quite easy since the solution follows directly from results given by Ewing, Jardetsky and Press [1957], subsequently referred to as EJP.

##### Case 1: Applied Normal Traction

Consider the Green's function boundary conditions (3) and set  $Q(r, \omega) = 0$ . Then from EJP, equations (2-59) to (2-68), it is quite easy to show that the dilatational potential,  $\phi$ , may be written as

$$\phi_N = \frac{1}{\mu} \int_0^\infty \frac{(2k^2 - k_\beta^2)}{F(k)} e^{-\nu z} J_0(kr) J_0(kr') k dk, \quad (38)$$

where  $F(k)$ , the Rayleigh function, and the other notations are as in EJP.

The  $k$ -integral (38) represents the total solution. The far-field body wave portion of the solution can be shown to result from evaluating (38) in the complex plane and approximating the branch line contribution to the integral by using the method of steepest descent. A number of authors have dealt with integrals of this form including EJP, Chapter 2, and Fuchs [1966]. Bache and Harkrider [1976, Eq. 30] write

the solution for far-field body waves in compact form. Observing this formula, the solution is

$$\phi_N^b = \frac{i}{\mu} \frac{k(2k^2 - k_\beta^2)}{F(k)} r_\alpha J_0(kr') \frac{e^{-ik_\alpha R}}{R}, \quad (39)$$

$$r_\alpha^2 = c^2/\alpha^2 - 1,$$

$$R^2 = r^2 + z^2,$$

$$\sin\theta = \alpha/c = r/R,$$

where  $\theta$  is the takeoff angle measured from the downward vertical and  $c$  is horizontal phase velocity. The far-field displacements are then found by differentiating (39) with respect to  $R$  and retaining only terms of order  $R^{-1}$ . The result is the Green's function

$$G_N^b(r|r') = k_\alpha k \frac{(2k^2 - k_\beta^2)}{\mu F(k)} r_\alpha J_0(kr') \frac{e^{-ik_\alpha R}}{R}. \quad (40)$$

#### Case 2: Applied Shear Traction

Now consider (32) and set  $P(r, \omega) = 0$ . Then following the same procedure as was used to derive (38), we find that

$$\phi_S^b = \frac{1}{\mu} \int_0^\infty \frac{2k\nu'}{F(k)} e^{-\nu z} J_0(kr) J_1(kr') dk. \quad (41)$$

The Green's function for far-field body waves is then

$$G_S^b(r|r') = \frac{2k_\alpha k}{\mu F(k)} (k^2 - k_\beta^2) r_\alpha J_1(kr') \frac{e^{-ik_\alpha R}}{R}. \quad (42)$$



The far-field body wave Green's functions (40, 42) are analogous to (27, 29) for surface waves. The relation between the Green's functions and the total solution for the distributed loads (1) is given by (4). Assuming the boundary loading to be applied in the region  $a \leq r \leq b$ , we have the total far-field body wave displacement

$$\begin{aligned}
 U(\omega) = & \int_a^b P_0(r', \omega) k_\alpha \frac{k(2k^2 - k_\beta^2)}{\mu F(k)} r_\alpha J_0(kr') \frac{e^{-ik_\alpha R}}{R} r' dr' \\
 & + \int_a^b Q_0(r', \omega) 2k_\alpha \frac{k(k^2 - k_\beta^2)}{\mu F(k)} r_\alpha J_1(kr') \frac{e^{-ik_\alpha R}}{R} r' dr'.
 \end{aligned}
 \tag{43}$$

This may be reduced to

$$U(\omega) = \frac{k k_\alpha r_\alpha}{\mu F(k)} \frac{e^{-ik_\alpha R}}{R} \left\{ (2k^2 - k_\beta^2) \hat{P}(\omega) + (k^2 - k_\beta^2) \hat{Q}(\omega) \right\} \tag{44}$$

where  $\hat{P}(\omega)$ ,  $\hat{Q}(\omega)$  are the spatial integrals given by (33).